Aus dem Experimental and Clinical Research Center
der Medizinischen Fakultät Charité – Universitätsmedizin Berlin

DISSERTATION

Characterisation of the *Prdm16*$^{csp1/wt}$ mouse as a model for the *PRDM16* associated Cardiomyopathy

Charakterisierung der *Prdm16*$^{csp1/wt}$ Maus als ein Modell für die *PRDM16* assoziierte Kardiomyopathie

zur Erlangung des akademischen Grades
Doctor medicinae (Dr. med.)

vorgelegt der Medizinischen Fakultät
Charité – Universitätsmedizin Berlin

von

Simon Theisen

aus Saarbrücken

Datum der Promotion: 23.03.2024

Table of Contents

List of Figures

List of Tables

Abbreviations

α-Sma	Alpha smooth muscle actin
aa	Amino acids
AcCoA	Acetyl conenzyme A
Acsl1	Long-chain acyl coenzyme synthetase isoform 1
Actn2	Alpha-actinin 2
Actc1	Actin, alpha cardiac muscle 1
Adh1	Alcohol dehydrogenase 1
Aldh3a1	Aldehyde dehydrogenase 3 family member A1
Aldob	Fructose-bisphosphate aldolase B
Ank	Progressive ankylosis protein
ARVC	Arrhythmogenic right ventricular cardiomyopathy
ATP	Adenosine triphosphate
Atp5a	ATP synthase F1 subunit alpha
BAT	Brown adipose tissue
BCA	Bicinchoninic acid
bp	Base pairs
BSA	Bovine serum albumin
ChIP	Chromatin immunoprecipitation
Cox4	Cytochrome c oxidase subunit 4
Ct	Cycle threshold
C/EBPβ	CCAAT/Enhancer-binding-protein-beta
cDNA	Complementary DNA
cKO	Cardiac-specific knockout
CMP	Cardiomyopathy
CO	Cardiac output
Col1	Collagen type I alpha 1
CTBP	C-terminal-binding protein
DAPI	4′,6-diamidino-2-phenylindole
DCM	Dilated cardiomyopathy
DEPC	Diethyl pyrocarbonate
Dhtkd1	Dehydrogenase E1 and transketolase domain containing 1
DNA	Deoxyribonucleic acid
dNTP	Deoxyribonucleotide triphosphate

Dsp	Desmoplakin
ECG	Electrocardiogram
EF	Ejection fraction
EHMT1	Euchromatic histone-lysine-N-methyltransferase 1
ELISA	Enzyme-linked immunosorbent assay
ENU	N-ethyl-N-nitrosourea
ETC	Electron transport chain
$FADH_2$	Flavin adenine dinucleotide
Gapdh	Glyceraldehyde-3-phosphatase dehydrogenase
GC-MS	Gas chromatography–mass spectrometry
gDNA	Genomic DNA
GIT	Gastrointestinal tissue
Glc	Glucose
H&E	Hematoxylin and eosin staining
HCM	Hypertrophic cardiomyopathy
HDAC1/3	Histone deacetylase 1/3
HF	Heart failure
HKMT	Histone lysine methyltransferase
HLX	Homebox-protein HB24
HPLC	High-performance liquid chromatography
HRP	Horseradish peroxidase
HSC	Hematopoietic stem cell
Hsp70	Heat shock protein 70
iPSC-CM	Induced pluripotent stem cell derived cardiomyocytes
IVCT	Isovolumetric contraction time
IVSd/s	Interventricular septum at diastole/systole
Junb	Transcription factor jun-B
JUP	Junction plakoglobin
Lac	Lactate
Lcat	Phosphatidylcholine-sterol acyltransferase
LFC	Log2 fold change
loxP	Locus of crossover P1
LVIDd/s	Left ventricular internal diameter at diastole/systole
LVNC	Left ventricular non-compaction cardiomyopathy

LVPWd/s	Left ventricular posterior wall at diastole/systole
MED1	Mediator of RNA polymerase II transcription subunit 1
MCS	Multiple cloning site
MC4R	Melanocortin receptor 4
mt	Mitochondrial
Mtco1	Mitochondrially encoded cytochrome c oxidase I
MFN2	Mitofusin-2
mRNA	Messenger RNA
Mybpc3	Cardiac myosin-binding protein C
Myh6	Myosin Heavy Chain 6
Myh7	Myosin Heavy Chain 7
Myl3	Myosin light chain 3
MYCN	N-myc proto-oncogene
NADH	Nicotinamide adenine dinucleotide
NCBI	National Center for Biotechnology Information
Ndufb8	NADH dehydrogenase [ubiquinone] 1 beta subcomplex subunit 8
NGS	Next-generation sequencing
Nmrk2	Nicotinamide riboside kinase 2
Nppb	Natriuretic peptide B
Nr1d1	Nuclear receptor subfamily 1 group D member 1
NuRD	Nucleosome remodelling deacetylase
PBS	Phosphate buffered saline
Pbxip1	Pre-B-cell leukemia transcription factor-interacting protein 1
PCR	Polymerase chain reaction
Per1	Period circadian protein homolog 1
PGC-1	Peroxisome proliferator-activated receptor gamma coactivator 1
PRDM16	PR domain containing 16
PPP	Pentose phosphate pathway
PPAR	Peroxisome proliferator-activated receptor
PVDF	Polyvinylidene fluoride
PWD	Pulsed wave Doppler
Pyr	pyruvate
Pyroxd2	Pyridine nucleotide-disulfide oxidoreductase domain-containing protein 2
qPCR	Quantitative polymerase chain reaction

RFLP	Restriction fragment length polymorphism
RNA	Ribonucleic acid
ROI	Region of interest
Rorb	Nuclear receptor ROR-beta
Rorc	Nuclear receptor ROR-gamma
ROS	Reactive oxygen species
Runx3	Runt-related transcription factor 3
Scd4	Stearoyl-CoA desaturase 4
Sdha/b	Succinate dehydrogenase complex, subunit A/B
SKI	Ski oncogene
SV	Stroke volume
TDI	Tissue Doppler imaging
TBS-T	Tris-buffered saline with Tween20
TBX20	T-box transcription factor TBX20
TCA	Tricarboxylic acid cycle
Tcap	Telethonin
TEM	Transmission electron microscopy
TGF-β	Transforming growth factor beta
Tnni3	Cardiac muscle troponin I
Tnnt2	Cardiac muscle troponin T
Tom20	Mitochondrial import receptor subunit TOM20
Tpm1	Tropomyosin alpha-1 chain
TTE	Tris-Taurine-EDTA
Ttn	Titin
Ubiad1	UbiA prenyltransferase domain-containing 1
Uqrc2	Cytochrome b-c1 complex subunit 2
WGA	Wheat germ agglutinin
Wt	Wild-type
ZFP156	Zinc finger Protein 156

Kurzdarstellung

Einführung: Genetische Varianten in *PR domain containing 16* (*PRDM16*) sind mit Kardiomyopathien (KMP) assoziiert. Es ist bekannt, dass PRDM16 in nicht-kardialem Gewebe Einfluss auf Transkription, Differenzierung, Transforming growth factor-β (TGF-β), Stoffwechselprozesse und Mitochondrien hat. Der Pathomechanismus der *PRDM16* KMP ist jedoch unzureichend geklärt. Neue Erkenntnisse deuten auf eine mitochondriale Dysfunktion als Ursache hin. Um die Rolle von *PRDM16* für die Entstehung einer KMP weiter zu untersuchen, analysierten wir Pathophysiologie und molekularer Defekt im *Prdm16*$^{csp1/wt}$ Maus Modell mit systemischer, heterozygoter *Prdm16* Inaktivierung.

Methoden: Die Spleiß-Mutation *csp1* in *Prdm16*$^{csp1/wt}$ Mäusen wurde mit Endpunkt PCR, Klonierung, Hochdurchsatz-Sequenzierung und quantitativer PCR (qPCR) in Herz und Lungen RNA analysiert. Der Phänotyp wurde charakterisiert hinsichtlich Körperzusammensetzung, Echokardiographie, Elektrokardiographie, Blutdruck und respiratorischer Funktion. *Prdm16*$^{csp1/wt}$ Herzschnitte wurden in Picro-Sirius Red, H&E und Weizenkeimagglutinin (WGA) gefärbt. Anschließend wurden diese hinsichtlich Fibrose, Struktur und Kardiomyozytenquerschnitt analysiert. Mit Transmissionselektronenmikroskopie (TEM) wurde die kardiale Ultrastruktur beurteilt. Die Expression von Sarkomer Genen und *Natriuretischem Peptid B (Nppb)* wurden mit qPCR gemessen. Das Herz Transkriptom wurde mit Hochdurchsatz-RNA-Sequenzierung analysiert. Die mitochondriale und metabolische Funktion in *Prdm16*$^{csp1/wt}$ Herzen wurde evaluiert durch Gas Chromatografie-Massenspektrometrie (GC-MS) des zentralen Kohlenstoffmetabolismus und mit Western Blot Analyse der Elektronentransportkette (ETC).

Ergebnisse: Die *csp1* Mutation beeinträchtigte das Spleißen und verursachte reduziertes mutantes *Prdm16* Transkript. *Prdm16*$^{csp1/wt}$ Mäuse zeigten einen milden KMP Phänotyp, der stärker in Weibchen ausgeprägt war: reduziertes Körpergewicht, hypotrophe Herzen, reduzierte Herzfunktion, normaler Blutdruck und respiratorische Funktion. *Nppb* war in *Prdm16*$^{csp1/wt}$ Weibchen hochreguliert. Im *Prdm16*$^{csp1/wt}$ Herz war die Gewebestruktur normal, eine Fibrose war nicht nachweisbar und der Kardiomyozytenquerschnitt war reduziert. TEM zeigte einen normalen mitochondrialen Gehalt und leicht kürzere Sarkomere. Die Genexpression und die Zusammensetzung des Sarkomers waren größtenteils unverändert. Auffallend waren verminderte Metabolite des zentralen Kohlenstoffmetabolismus in *Prdm16*$^{csp1/wt}$ Herzen. Die

Western Blot Analyse zeigte verringerte ETC Komplex IV Proteine in weiblichen *Prdm16*$^{csp1/wt}$ Mäusen.

Schlussfolgerung: *Prdm16*$^{csp1/wt}$ Mäuse zeigen milde KMP Zeichen. Diese Arbeit bestätigt die Bedeutung von *PRDM16* für den kardialen Stoffwechsel und Mitochondrien. Das Geschlecht ist potenzieller Einflussfaktor für die *PRDM16* Funktion. Weitere Untersuchungen des *Prdm16*$^{csp1/wt}$ Stoffwechsels und der mitochondrialen Funktion können hilfreich sein den Pathomechanismus der *PRDM16* KMP aufzudecken.

Abstract

Introduction: Genetic variants of *PR domain containing 16* (*PRDM16*) are associated with cardiomyopathy (CMP). In non-cardiac tissues, the PRDM16 protein regulates transcription, differentiation, transforming growth factor-β (TGF-β), metabolism, and mitochondrial activity. However, the pathogenesis of the *PRDM16* associated CMP is largely unresolved. Recent findings suggest mitochondrial dysfunction as a possible cause. To further explore the role of *PRDM16* in CMP, we used the *Prdm16*$^{csp1/wt}$ mouse model with systemic, heterozygous *Prdm16* deactivation and analysed the pathophysiology and underlying molecular defects.

Methods: The splice site mutation *csp1* in *Prdm16*$^{csp1/wt}$ mice was evaluated with endpoint PCR, molecular cloning, high-throughput sequencing and quantitative PCR (qPCR) in heart and lung RNA. The *Prdm16*$^{csp1/wt}$ phenotype was characterised by body composition analysis, echocardiography, electrocardiography, blood pressure measurements, and respiratory analysis. *Prdm16*$^{csp1/wt}$ heart sections were stained with Picro-Sirius Red, H&E, and wheat germ agglutinin (WGA). Subsequently, sections were analysed for fibrosis, tissue organisation, and cross-sectional cardiomyocyte area. With transmission electron microscopy (TEM), the cardiac ultrastructure was assessed. Expression analysis was performed by qPCR for sarcomere genes and *Natriuretic peptide B (Nppb)*. In addition, the heart transcriptome was analysed with high-throughput RNA sequencing. Mitochondrial and metabolic function in *Prdm16*$^{csp1/wt}$ hearts were evaluated by gas chromatography-mass spectrometry (GC-MS) of the central carbon metabolism and by Western blot analysis of the electron transport chain (ETC).

Results: The *csp1* mutation negatively affected splicing and reduced the *Prdm16* mutant transcript level. *Prdm16*$^{csp1/wt}$ mice presented with a mild CMP phenotype,

interestingly more evident in females: lower body weights, cardiac hypotrophy, diminished cardiac function, as well as normal blood pressure and respiratory function. *Nppb* was elevated in *Prdm16*$^{csp1/wt}$ females. In the *Prdm16*$^{csp1/wt}$ heart tissue, the histological structure was organised normally, fibrosis was absent, and the cross-sectional cardiomyocyte area was reduced. TEM revealed normal mitochondrial content and slightly shorter sarcomeres in *Prdm16*$^{csp1/wt}$ hearts. Global gene expression and sarcomere composition remained largely unaffected by heterozygous *Prdm16* deletion. Strikingly, the central carbon metabolism was decreased in *Prdm16*$^{csp1/wt}$ hearts. Western blot analysis showed diminished ETC complex IV proteins in female *Prdm16*$^{csp1/wt}$ mice.

Conclusion: Heterozygous *Prdm16*$^{csp1/wt}$ mice displayed mild signs of CMP. This study confirms a critical role of *PRDM16* in cardiac metabolism and mitochondria, and identifies sex as a potential modifier of *PRDM16* function. Further exploration of the *Prdm16*$^{csp1/wt}$ metabolism and mitochondrial function can help to resolve the disease mechanism of the *PRDM16* CMP.

1 Introduction

1.1 Cardiomyopathies

The term cardiomyopathy (CMP) describes a heterogeneous group of myocardial diseases. Common classifications distinguish primary CMPs from secondary CMPs. Primary CMPs are defined as mainly myocardial disorders, whereas secondary CMPs are caused by systemic diseases (1, 2). The etiology of primary CMPs can be genetic, acquired, or mixed. Another categorisation of CMP is based on the phenotype, i.e., hypertrophic cardiomyopathy (HCM), dilated cardiomyopathy (DCM), arrhythmogenic right ventricular cardiomyopathy (ARVC), left ventricular non-compaction cardiomyopathy (LVNC), and restrictive cardiomyopathy (RCM) (1-4). Despite distinct causes and phenotypes, the clinical presentation of CMPs is similar to the general signs of heart failure, such as reduced ejection fraction (EF), peripheral oedema, fatigue, dyspnoea, orthopnoea, exhaustion, paroxysmal nocturnal dyspnoea, syncope, presyncope, and cardiac ischemia (5). This dissertation explores the role of the gene *PR domain containing 16* (*PRDM16*) - a known DCM and LVNC disease gene - in cardiac physiology and pathophysiology. Therefore, only DCM and LVNC will be described accurately. Some information about HCM, ARVC, and RCM is shown in Table 1.

Dilated Cardiomyopathy

The yearly incidence of DCM is 2-8/100,000 and the estimated prevalence is 1/250. Between 30 % and 50 % of cases are caused genetically (6, 7). DCM is defined by enlarged left ventricular chamber dimension, normal wall thickness, and normal systolic dysfunction. Severe complications like heart failure, thromboembolism, and sudden cardiac death make DCM the leading cause for heart transplantation (1, 7). Inheritance of DCM is mainly autosomal dominant, but also it being x-chromosomal, autosomal recessive, or mitochondrial is possible (7, 8). The two most common hypotheses for DCM pathogenesis are based on the fact that genetic DCM is mainly caused by variants in genes encoding proteins of the cytoskeleton and sarcomere. The “defective force transmission” hypothesis states that disease-causing mutations lead to impaired connection between the sarcomere and the sarcolemma. The “defective force generation” hypothesis states that disease-causing mutations lead to insufficient

force generation at the sarcomere (3, 8). Further explanations refer to metabolic alterations, especially in oxidative phosphorylation and redox homeostasis (9).

Left ventricular non-compaction

The prevalence of LVNC is estimated to be below 1 %. LVNC presents with a hypertrabeculated left ventricle and intertrabecular recesses that can cause left ventricular dysfunction, heart failure, thromboembolism, and sudden cardiac death. However, it is highly debated if LVNC should be defined as an independent entity or if LVNC is rather a phenomenon which occurs in other CMPs or congenital heart diseases. Furthermore, the clinical presentation of LVNC is extremely heterogeneous, ranging from lifelong symptom free cases to severe heart failure (1, 5, 7, 10). Inheritance of LVNC is mainly autosomal dominant or x-chromosomal recessive, but also autosomal recessive or mitochondrial. Genetic variants associated with LVNC affect the sarcomere, the z-disc, the nuclear envelope, ion channels, and signalling pathways (7, 10). Due to the clinical and genetic heterogeneity of LVNC, it is challenging to develop explanations for its pathomechanism. Current hypotheses are based on murine models and describe LVNC as a consequence of dysregulated signalling in late embryonic development, e.g., Transforming growth factor beta (Tgf-β), Notch or Wnt (11).

Table 1. Overview of cardiomyopathies.

Cardiomyopathy	Description (1, 5)	Prevalence (1, 5-7)	Main cause (1, 4, 5)	Primarily affected structure (3, 7, 8, 10, 12)
HCM	- Left ventricular hypertrophy - Typical: interventricular septum - No dilation	1:500	Genetic	Sarcomere (e.g., *MYH7, MYBPC3*)
DCM	- Enlarged chamber dimensions - Normal wall thickness - Impaired systolic function	1:250	Mixed	Sarcomere (e.g., *Ttn, MYH7*), cytoskeleton (e.g., *DES, DMD*)
RCM	- Stiffening of ventricles - Diastolic dysfunction	rare	Mixed	Sarcomere (e.g., *MYH7,* TNNI3), z-disc (e.g., *MYPN*)
ARVC	- Thinning and dilation - Fibrosis - Typical: right ventricle	1:1000-1:5000	Genetic	Desmosome (e.g., *DSP, JUP*)
LVNC	- Hypertrabeculated left ventricle	1%	Genetic	Heterogenous (e.g., *MYH7, TAZ, LDB3*)

HCM – Hypertrophic cardiomyopathy; DCM – Dilated cardiomyopathy; RCM – Restrictive cardiomyopathy; ARVC – Arrhythmogenic right ventricular cardiomyopathy; LVNC – Left ventricular non-compaction cardiomyopathy; genes are abbreviated according to the Entrez Gene database of the National Center for Biotechnology Information (NCBI).

1.2 Mutations in *PRDM16* cause cardiomyopathy

Arndt et al. (13) identified *PRDM16* as a CMP disease gene by genetic screening of 1p36 deletion syndrome patients. Variable heterozygous terminal deletion of chromosome 1 leads to this heterogeneous disease pattern with differential expression of craniofacial malformation, intellectual deficits, structural brain disorders, hearing loss, delayed growth, structural heart disease, and CMP (14). Interestingly, patients with 1p36 deletion syndrome and CMP lacked a common region of chromosome 1, containing exons 4-17 of *PRDM16* (Figure 1). Remarkably, 16 of these 18 patients were female, raising the question of sex-specific aspects in *PRDM16* associated CMP. Sequencing of LVNC and DCM cohorts identified novel *PRDM16* variants and a higher frequency of non-synonymous *PRDM16* variants in DCM patients compared to the Exome Sequencing Project. Furthermore, transgenic expression of a novel truncating *PRDM16* variant (c.2104A>T [p.Lys702*]) or *PRDM16* knockdown in zebrafish led to reduced cardiac output (CO), bradycardia, impaired cell proliferation, increased apoptosis, and electrical uncoupling in cardiomyocytes. Also, injection of minimal doses of antisense oligonucleotides for *PRDM16* or *Ski oncogene (SKI)* showed no effect if applied separately, but lowered cardiac output if applied simultaneously. This points towards a functional connection between *SKI* and *PRDM16* (13).

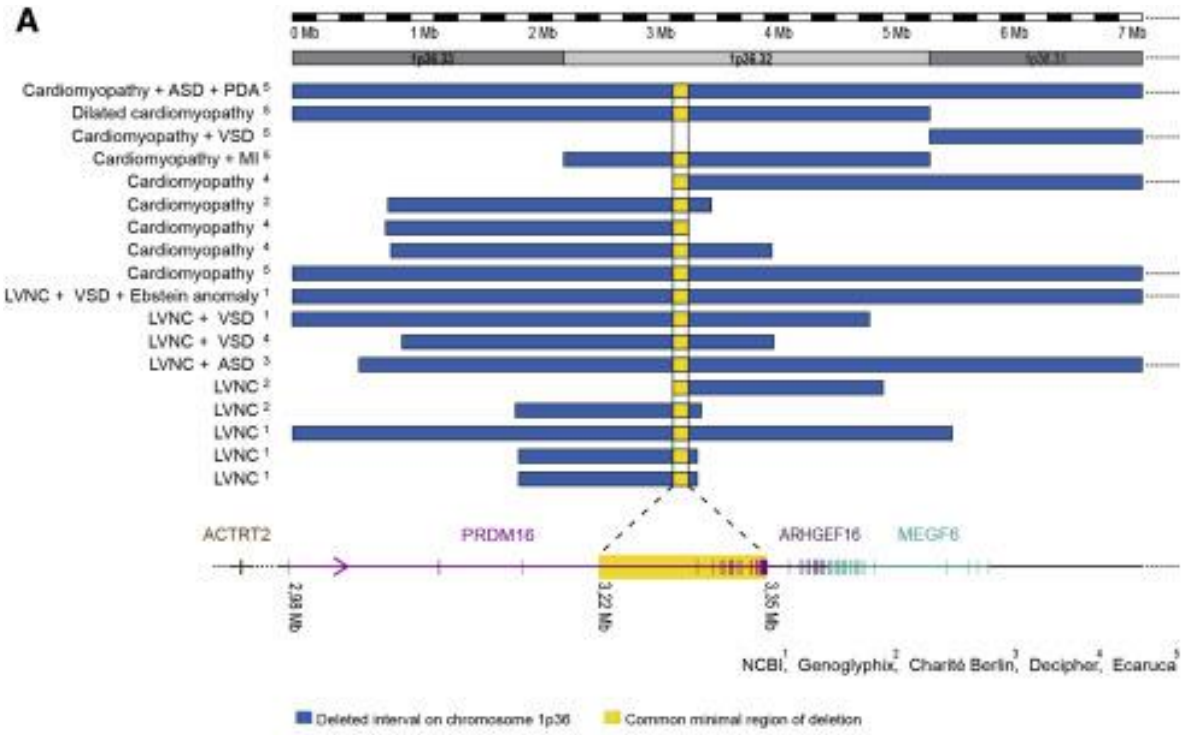

Figure 1. Loss of *PRDM16* in 1p36 deletion syndrome with cardiomyopathy. The figure shows the deleted regions (blue) of chromosome 1 in patients with 1p36 deletion syndrome and cardiomyopathy. The overlapping region of loss (yellow) contains *PRDM16* exons 4-17. Abbreviations: ASD – atrial septal defect; VSD – ventricular septal defect; PDA – patent ductus arteriosus; MI – mitral insufficiency (Arndt et al. (13), DOI: 10.1016/j.ajhg.2013.05.015, agreement of Elsevier Inc.).

1.3 Molecular functions of PRDM16

1.3.1 Gene and protein structure of human *PRDM16* and murine *Prdm16*

Human *PRDM16* locates to chromosome 1: 3,069,168-3,438,621 (forward strand), contains 17 exons, and encodes four different PRDM16 protein isoforms with lengths between 1092 and 1276 amino acids (aa), and molecular weights between 120 and 140 kDa (Figure 2) (15, 16). The 1276 aa isoform (PRDM16fl) and the 1092 aa isoform (PRDM16s) are well characterised. The biological role of the other isoforms remains unclear. PRDM16 consists of an N-terminal PR domain, an N-terminal and a C-terminal C2H2 zinc finger domain, a proline rich domain, a repressor domain, and a C-terminal acidic activation domain (17). The PR domain displays histone lysine methyltransferase (HKMT) activity (18, 19). The zinc fingers show sequence-specific DNA-binding, but their importance seems greater for protein-protein interactions (17, 20-29). The repressor domain contains a 5 aa PLDS motif, relevant for C-terminal-binding protein 1/2 (CTBP1/2) mediated gene repression (23). The functions of the proline rich domain and the acidic activation domain are unclear. The activation domain possibly regulates transforming growth factor beta (TGF-β) signalling through SKI

interaction (Figure 2 B) (24). Immunostaining and Western blotting of subcellular fractions detected human PRDM16 and murine Prdm16 in the nucleus and the cytoplasm (13, 19, 24, 30). During embryonic mouse development, *Prdm16* is expressed ubiquitously. In adult mice, the *Prdm16* expression is enriched in neuronal tissue, lung, heart, craniofacial tissue, kidney, liver, the gastrointestinal tract, and adipose tissue (21, 30, 31).

Murine *Prdm16* locates to chromosome 4: 154,316,125-154,636,873 (reverse strand). Its genomic and protein structure resembles human *PRDM16*. Next to the canonical 1275 aa Prdm16, Uniprot enlists two isoforms of 1178 aa and 1276 aa (15). However, a short isoform corresponding to PRDM16s has not been described in mice so far (15, 16).

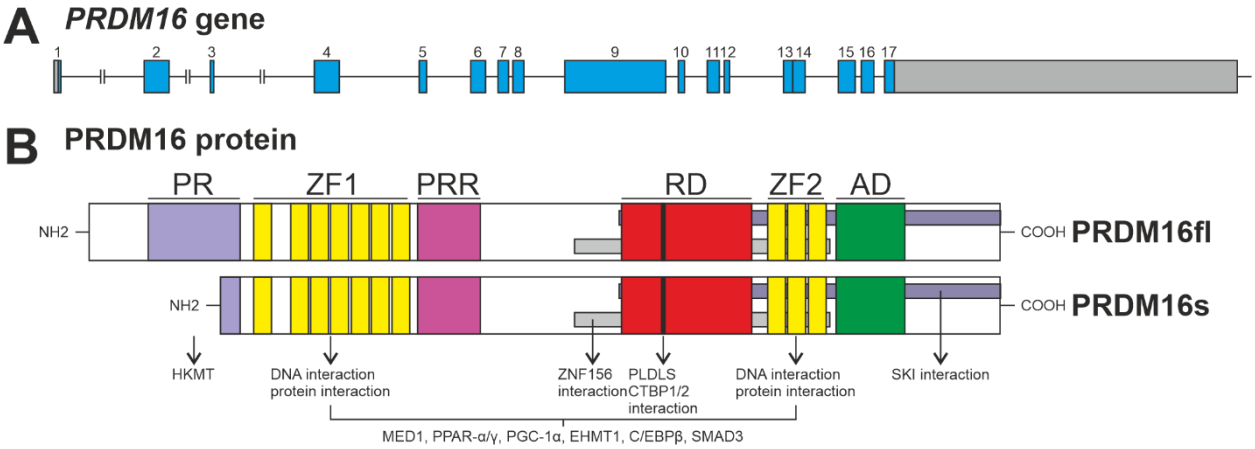

Figure 2. *PRDM16* gene and resulting proteins. A *PRDM16* consists of 17 exons (blue). **B** The two main protein isoforms of PRDM16 and its domains. The arrows indicate regions with known interaction partners. Abbreviations: PR – PR domain; ZF1/2 – zinc finger domain 1/2; RD – repressor domain; AD – acidic activation domain; HKMT – histone lysine methyltransferase; CTBP1/2 – C-terminal-binding protein 1/2; MED1 – mediator of RNA polymerase II transcription subunit 1; PPAR-α/γ – peroxisome proliferator-activated receptor-alpha/gamma; PGC-1α – peroxisome proliferator-activated receptor gamma coactivator 1-alpha; EHMT1 – euchromatic histone-lysine-N-methyltransferase 1; C/EBPβ – CCAAT/enhancer-binding-protein-beta.

1.3.2 PRDM16 is a critical regulator of transcription, differentiation and the cell cycle

PRDM16 function in transcriptional regulation and differentiation has been studied intensively, especially in adipose tissue. *PRDM16* is critical for the differentiation, maintenance, and function of beige and brown adipose tissue (BAT) (20-22, 32, 33). *PRDM16* induces BAT-specific gene expression, represses muscle and white adipocyte-specific genes, induces adaptive thermogenesis, and increases energy

expenditure (20-23, 25, 29, 32-35). On a functional level, PRDM16 physically interacts with several transcriptional regulators in adipose tissue. Induction of BAT genes is mediated through interaction with peroxisome proliferator-activated receptor-alpha/gamma (PPAR-α/γ) and their co-activators peroxisome proliferator-activated receptor gamma coactivator 1-alpha/beta (PGC-1α/β), CCAAT/Enhancer-binding protein-beta (C/EBPβ), zinc finger Protein 156 (ZFP156), or homebox-protein HB24 (HLX) (20-22, 36, 37) (Figure 3 A). Gene repression is mediated by recruiting CTBP-1 and CTBP-2 to their promotors (Figure 3 A). Thereby, PGC-1α competes for interaction with PRDM16 (23). Furthermore, PRDM16 is critical for the function of histone-modifying enzymes like euchromatic histone-lysine-N-methyltransferase 1 (EHMT1) or histone deacetylase 3 (HDAC3) (25, 38) (Figure 3 A).

Furthermore, PRDM16 influences the epigenetics and organisation of higher chromatin structure. Next to its DNA-binding capacity, PRDM16 possesses intrinsic histone lysine methyltransferase (HKMT) activity (17-20). Also, PRDM16 interacts with several components of the nucleosome remodelling deacetylase (NuRD) complex, a multiprotein complex which regulates chromatin structure (39, 40). By binding and recruiting mediator of RNA polymerase II transcription subunit 1 (MED1), PRDM16 connects nuclear transcription factors with the general transcription machinery (28, 29).

In addition to adipose tissue formation, PRDM16 is essential for stem- and progenitor cells of other tissues (27, 30, 41-45) (Figure 3 B). Deletion of *Prdm16* in mice led to malformations in craniofacial tissue, retina, choroid plexus, salivary glands, and lungs. Also, *Prdm16*-deficient mice demonstrated smaller heart ventricles and a cleft at the apex (30). Studies in hematopoietic stem cells (HSCs) and enterocytes of *Prdm16*-deficient mice revealed that Prdm16 influences apoptosis, the cell cycle, and proliferation (41, 42, 45). Prdm16 is critical for differentiation, maintenance, and function of embryonic and adult neuronal stem cells, mainly by regulating oxidative stress (27, 42-44). Either *Prdm16* depletion or overexpression lead to higher concentrations of mitochondrial reactive oxygen species (mtROS) and total ROS. Pgc-1α was identified as a possible downstream target of *Prdm16* in a complex regulatory network of neuronal differentiation (27).

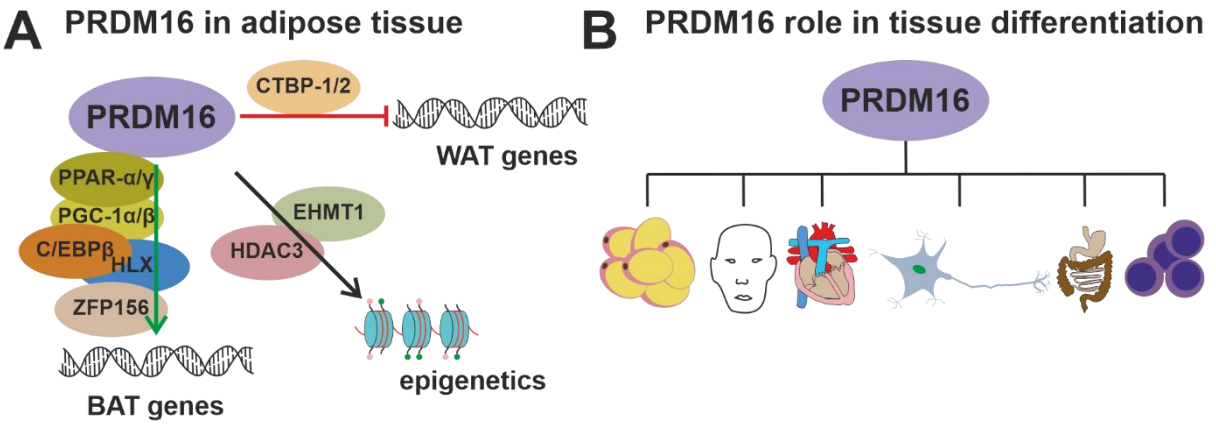

Figure 3. PRDM16 function in adipose tissue and differentiation of multiple tissues. A In adipose tissue PRDM16 controls a brown/beige adipocyte phenotype and upregulates BAT-specific genes through interaction with PPAR-α/γ, PGC-1α/β, C/EBPβ, ZFP156, or HLX. Also, PRDM16 downregulates WAT and muscle-specific genes through interaction with CTBP-1/2. PRDM16 is linked to epigenetics via HDAC3 and EHMT1. **B** PRDM16 was found to drive the differentiation of adipose tissue, craniofacial tissue, the cardiovascular system, neuronal tissue, the gastrointestinal tract, and hematopoietic stem cells. Abbreviations: BAT – brown adipose tissue; WAT – white adipose tissue.

1.3.3 PRDM16 influences Transforming growth factor-β signalling

Transforming growth factor-β (TGF-β) activates a signalling pathway through ligand binding at the TGF-β receptor type I or II. The consequence is phosphorylation of Smad2 and Smad3 followed by creation of a complex with Smad4. This complex translocates to the nucleus to regulate transcription. Numerous signalling molecules modulate TGF-β transduction, e.g., inhibitory Smads6/7 or SKI (24, 46). TGF-β controls biological processes, such as cellular proliferation, apoptosis, migration, adhesion, extracellular matrix production, and the organisation of the cytoskeleton. Via these functions, TGF-β plays a key role in the embryonic development of the cardiovascular system. Perturbations are linked to diseases, e.g., congenital heart disease or cardiac fibrosis (46).

Multiple studies have shown the interaction of PRDM16 with Smad2, Smad3, HDAC1 and SKI - all components of the TGF-β pathway (24, 47). Furthermore, PRDM16 was associated with inhibition of TGF-β in gastric cancer cells, adipocytes, and cardiac and orofacial tissue (24, 26, 47, 48). Conversly, TGF-β enhancement was observed in neurons (49). In T-cell leukemia, the effects were different depending on the *PRDM16* isoform (50). A possible mode of action for PRDM16 in the TGF-β pathway is the suppression of Smad3-dependent gene expression by stabilising the Smad3-HDAC1 complex in synergy with SKI (24).

Several studies revealed a connection between PRDM16 and TGF-β in cardiac tissue (13, 48, 51). As mentioned before (compare 1.2), it is likely for PRDM16 to function in synergy with the SKI ortholog in the zebrafish heart (13). Moreover, conditional cardiac-specific ablation of *Prdm16* in mice led to Tgf-β activation. Mutant mice showed elevated expression of *Tgfb1-3* and pro-fibrotic Tgf-β controlled genes, and increased p-Smad2/Smad2 ratio (48). Moreover, induced pluripotent stem cell derived cardiomyocytes (iPSC-CMs) of LVNC and DCM patients due to T-box transcription factor TBX20 (TBX20) mutations presented with decreased *PRDM16* expression, diminished proliferative capacity, stronger phosphorylation of Smad2/3, and elevated expression of TGF-β target genes. Genome editing of *PRDM16* in iPSC-CMs resulted in diminished proliferation and increased TGF-β target gene expression (51).

1.3.4 PRDM16 controls mitochondrial and metabolic function

Apparently, *PRDM16* is enriched in tissues with a highly active metabolism and regulates a large variety of genes involved in energy metabolism and mitochondrial function (20, 21, 32, 33, 42, 44, 45). Several studies associated *PRDM16* with proper mitochondrial content and structure (21, 27, 32). Furthermore, PRDM16 interacts with PPAR-α, PPAR-γ, PGC-1α, and PGC-1β, known key regulators of mitochondrial biogenesis, especially in cardiac tissue (20, 21, 23, 35, 52). Additionally, *PRDM16* is connected with mitochondrial dynamics. This process describes the constant fusion and fission of mitochondria to maintain their distribution, size, form, and function (52, 53). In HSCs, *Prdm16* induced *Mitofusin-2* (*Mfn2)* expression – a mediator of mitochondrial fusion – and was required for proper mitochondrial shape (52, 53). In adipocytes, PRDM16 increased cellular respiration and induced thermogenesis (20, 23, 32-35). As already mentioned (see 1.3.2), *PRDM16* regulates ROS production and expression of genes associated with redox homeostasis (27, 42, 44). Also, *Prdm16* was identified to control free fatty acid utilization and β-oxidation (25, 33, 45, 54).

Findings in astrocytoma cells were exemplary for *PRDM16's* impact on mitochondrial function. *PRDM16* ablation interrupted mitochondrial function entirely, as evidenced by depleted degenerated mitochondria, lower mitochondrial membrane potential, elevated ROS concentration, diminished ATP production, and strong activation of mitochondrial apoptosis (55). Figure 4 is a schematic summary of PRDM16's influence on mitochondria and metabolism.

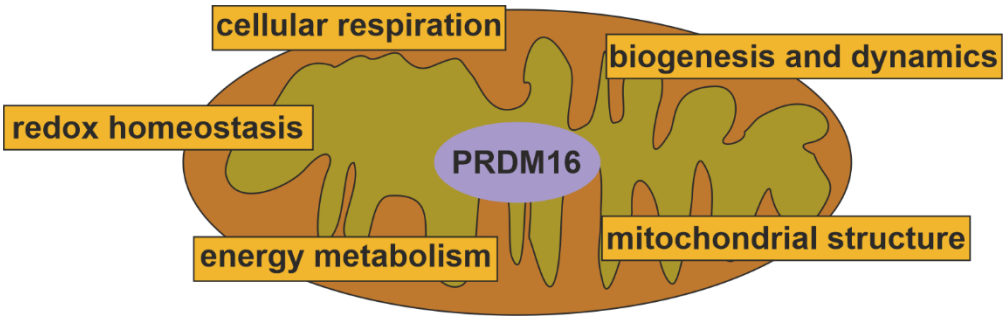

Figure 4. Role of PRDM16 in mitochondria and energy metabolism. PRDM16 is important for proper mitochondrial structure and function. It is deeply involved in the regulation of cellular respiration, energy metabolism, and redox homeostasis. Also, PRDM16 is involved in mitochondrial biogenesis and dynamics.

1.4 Cardiac phenotype of *PRDM16* inactivation

To date, only a few studies have examined PRDM16 function in the heart. As described above (see 1.2), depletion of *PRDM16* in zebrafish led to impaired cardiac function and cardiomyocyte proliferation (13). Also, in iPSC-CMs PRDM16 – as a downstream target of TBX20 – regulated cell proliferation by modulating TGF-β signalling (51).

This dissertation evaluated heterozygous *Prdm16*$^{csp1/wt}$ mice of the FVB.C-Prdm16^{csp1}/J strain, which was originally established as a model for craniofacial development by N-ethyl-N-nitrosourea (ENU) induced mutagenesis (30). Mutant mice carry the intronic *csp1* mutation (c.888-3C>A) in the splice acceptor site of *Prdm16* exon 7. Bjork et al. found that the *csp1* allele is hypomorphic, which means that it causes aberrant splicing with variable efficiency. In the mutant *csp1* splice isoform, whole skipping of exon 7 leads to a frameshift and premature termination of translation. Interestingly, all *Prdm16*$^{csp1/csp1}$ mice died shortly after birth with signs of cardiopulmonary failure. *Prdm16*$^{csp1/csp1}$ mice demonstrated malformations in craniofacial tissue, retina, choroid plexus, and salivary glands. Their lungs were hypoplastic and appeared abnormal in histological stains. The cardiac phenotype of *Prdm16-deficient* mice was characterised by smaller, deformed ventricles with a clefted apex (Figure 5). Histological analysis did not detect perturbations in septa, valves, or large vessels. Moreover, the Prdm16^{csp1} lost the ability to inhibit TGF-β in HepG2 and Mv1Lu cells.

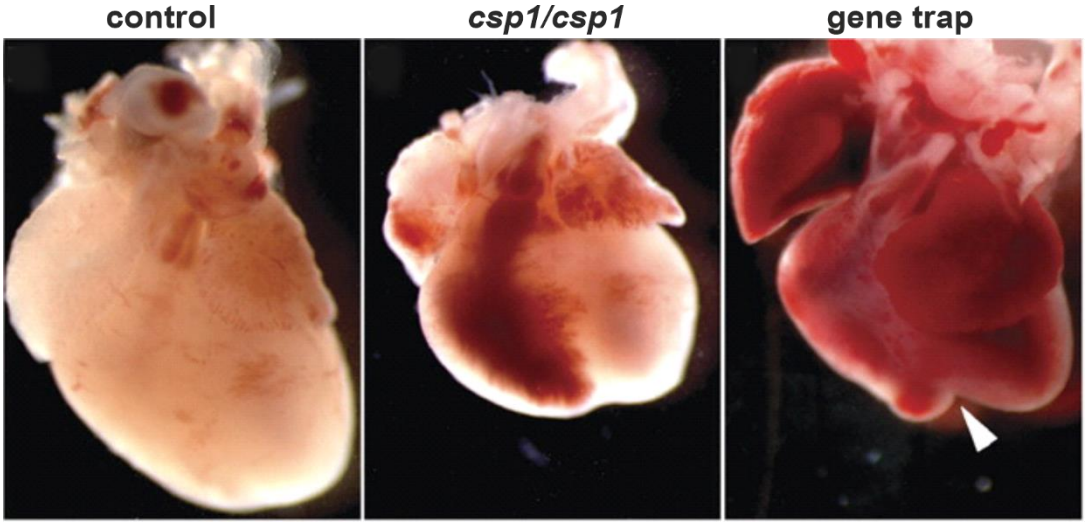

Figure 5. Cardiac phenotype of systemic homozygous *Prdm16* inactivation. *Prdm16*$^{csp1/csp1}$ hearts were hypopthropic and irregularly shaped. In gene-trap animals, the cleft in the apex was more prominent (modified from Bjork et al. (30), DOI: 10.1093/hmg/ddp543, agreement of Oxford University Press).

Recently, several cardiac-specific conditional *Prdm16* knockout (cKO) mouse strains were established (48, 56, 57). In one model, all animals survived postnatally. At different ages (1 month, 2 months, 5 months), *Prdm16* cKO mice presented with prolonged QRS and QTc durations, cardiomyocyte hypertrophy, and cardiac fibrosis (Figure 6 A). Remarkably, global heart hypertrophy appeared only in 5-month-old females. Expression analysis by qPCR and RNAseq revealed elevated transcripts of genes associated with cardiac fibrosis and hypertrophy, as well as dysregulated cardiac ion homeostasis. Also, Tgf-β activity was enhanced. However, its inhibition could not reverse the phenotype.

In another model, Cibi et al. (56) showed that *Prdm16* cardiac-specific conditional KO in mice leads to metabolic and mitochondrial dysfunction, finally ending in age-dependent cardiac malfunction, fibrosis, and hypertrophy (Figure 6 A - B). *Prdm16* cKO mice demonstrated changes in metabolic gene expression, metabolite levels, and mitochondrial ultrastructure. Also, electron transport chain (ETC) complexes were diminished (Figure 6 C). In young mice, these changes preceded impaired cardiac function and predisposed for metabolic stress-induced cardiac malfunction. Interestingly, structural heart defects were absent in neonates and late embryonic states. Moreover, ChIP analysis showed that binding of Prdm16 and Ehmt1 was necessary for the repression of hypertrophic genes.

In the most recent mouse model, homozygous *Prdm16* cKO led to a LVNC phenotype starting in late embryonic stages (57). Additionally, *Prdm16* cKO hearts exhibited a cleft at the apex, as seen in *Prdm16*$^{csp1/csp1}$ mice. Cardiac dysfunction caused the death of *Prdm16* cKO mice within seven days after birth. RNA-seq and ChIP-seq showed that *Prdm16* directly induced genes of the compact myocardium and repressed genes of the trabecular myocardium. Thereby, Prdm16 co-functioned with left-ventricular specific transcription factors. Interestingly, mitochondrial genes were repressed in *Prdm16* cKO hearts. Moreover, Wu et al. (57) stated that Prdm16 is negligible in the adult heart, because Prdm16 expression decreased during aging and inducible cKO did not result in obvious defects until 36 weeks after induction.

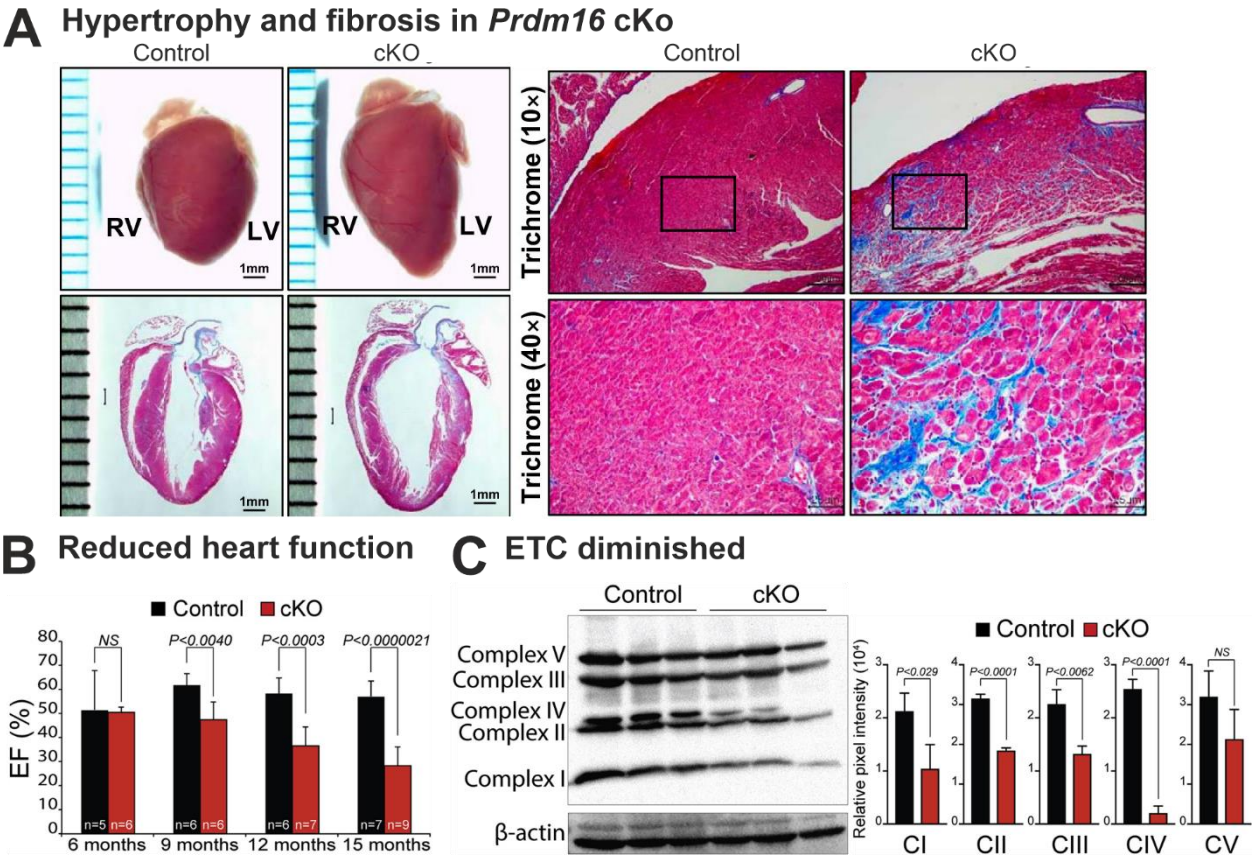

Figure 6. Homozygous cardiac-specific deletion of *Prdm16*. **A** On the left: whole hearts and trichrome stained sagittal sections showed heart hypertrophy of *Prdm16* cardiac-specific knockouts (cKO). On the right: severe fibrosis in *Prdm16* cKO hearts as evidenced by trichrome staining. Scale bar for 10x magnification is 100 µm and for 40x magnification, 25 µm. **B** Reduced EF in *Prdm16* cKO mice progressed with ageing of mice. **C** Western blots of ETC in *Prdm16* cKO mice and controls. Diminished levels of complex I - IV indicated mitochondrial dysfunction in *Prdm16* cKO mice. Values are shown as mean, error bars indicate standard deviation. Abbreviations: cKO – cardiac-specific knockout; RV – right ventricle; LV – left ventricle; EF – ejection fraction; ETC – electron transport chain (modified from Nam et al. (48), DOI: 10.1152/ajpheart.00647.2019, agreement of The American Physiological Society; and Cibi et al. (56), DOI: 10.1016/j.celrep.2020.108288, CC BY-NC-ND).

1.5 Metabolic and mitochondrial alterations in cardiomyopathy and heart failure

The mitochondrion is the main bioenergetic organelle and controls other cellular processes that play a role in CMP and heart failure (HF), e.g., ROS generation, antioxidative metabolism, cell survival, and calcium homeostasis. Mitochondrial and metabolic dysfunction are hallmarks of CMP and heart failure (9, 58-62). As the main source of energy production and ROS generation, the mitochondrial electron transport chain (ETC) is of special interest for the pathogenesis of CMP and HF. ETC malfunctions lead to impaired energy production, increased oxidative stress and damage, which further worsens the situation in a vicious cycle. ROS damage can lead to perturbations in almost any cellular function like contractility, ion homeostasis, or cell survival. Because it is difficult to measure ROS directly, ROS damage and dysregulated antioxidant genes deliver the most compelling evidence for ROS involvement in CMP and HF (58, 59).

The heart can use any kind of substrate for energy production to meet its high energy demand (carbohydrates, fatty acids, ketone bodies, lactate, and amino acids). However, there is a preference in substance use that also changes in age and disease. Perinatally, the heart switches from predominant use of carbohydrates towards fatty acid oxidation accompanied by increased mitochondrial biogenesis. Oxidative phosphorylation becomes the main source of energy production. (61, 62). In CMP and HF, metabolic alterations usually appear early in disease progression before cardiac dysfunction. The most common are a switch back towards carbohydrate utilisation and an increase in ketone body metabolism. However, other - and partially contrary - effects have been observed. Also, it remains unclear if metabolic remodelling is adaptive, maladaptive, or causative in CMP and HF. However, the consensus is that mitochondrial oxidative capacity is impaired during HF and CMP. It seems that the loss of metabolic flexibility can perturb cardiac stress response (9, 58, 60-62).

1.6 Aims

CMP is a severe, life-threatening disease which can lead to HF. Genetic variants in *PRDM16* are a known cause of CMP (13, 48). Improved understanding of PRDM16

molecular functions and their implications for cardiac physiology as well as the pathogenesis of CMP is a prerequisite for the development of novel diagnostic, preventive, and therapeutic strategies targeting the *PRDM16* associated CMP. However, very little research about the cardiac roles of PRDM16 exists. In order to establish a murine model for the *PRDM16* CMP, we analysed *Prdm16*$^{csp1/wt}$ mice with systemic heterozygous *Prdm16* inactivation.

1. *Evaluation of the csp1 mutation for Prdm16 pre-mRNA splicing in cardiac tissue*. We studied how heterozygous presence of the *csp1* mutation (c.888-3C>A) affects splicing of the *Prdm16* transcript, and quantified splice isoforms.
2. *Physiological analysis of Prdm16*$^{csp1/wt}$ *mice*. Phenotyping of *Prdm16*$^{csp1/wt}$ mice focused on cardiac function. Furthermore, the study included basic examination of body composition and respiratory function.
3. *Morphological analysis of Prdm16*$^{csp1/wt}$ *hearts.* Different histological stains helped us to investigate the cardiac tissue structure of *Prdm16*$^{csp1/wt}$ mice. Also, the ultrastructure was studied.
4. *Molecular analysis of Prdm16*$^{csp1/wt}$ *hearts.* In order to identify possible causes of the *PRDM16* CMP, we investigated molecular alterations after heterozygous *Prdm16* inactivation. We specifically targeted mitochondrial function with expression analysis and measurement of metabolites.

2 Materials and Methods

2.1 Materials

2.1.1 Consumables

Table 2. Consumables.

Consumable (Ref)	Company, Country
SafeSeal reaction tube 1.5ml (72706)	SARSTEDT, Germany
Eppendorf Safe-Lock tubes 2.0 ml (30120094)	Eppendorf, Germany
RNase-free microfuge tubes 1.5 ml (AM12400)	Thermo Fisher Scientific, Germany
PCR tubes, strips of 8 (AB-0264)	Thermo Fisher Scientific, Germany
Greiner tubes 50 ml, PP (227261)	Sigma-Aldrich/Merck, Germany
Greiner tubes 15 ml, PP (188271)	Sigma-Aldrich/Merck, Germany
Qubit assay tubes (Q32856)	Thermo Fisher Scientific, Germany
MicroAmp optical 96 well reaction plate (4306737)	Thermo Fisher Scientific, Germany
96 well plate PCR (AB-0600)	Thermo Fisher Scientific, Germany
96 well plate Sanger sequencing (AB-1100)	Thermo Fisher Scientific, Germany
96 well plates, polystyrene (M2186-100EA)	Sigma-Aldrich/Merck, Germany
Pipet tips 1-10 µl (701114)	SARSTEDT, Germany
Pipet tips 200 µl (70760002)	SARSTEDT, Germany
Pipet tips 1000µl (70762100)	SARSTEDT, Germany
SafeSeal SurPhob filter tips 10 µl (VT0200)	Biozym Scientific, Germany
SafeSeal SurPhob filter tips 200 µl (VT0240)	Biozym Scientific, Germany
SafeSeal SurPhob filter tips 1250 µl (VT0270)	Biozym Scientific, Germany
Filter tips, 12.5 µl (4415)	INTEGRA Biosciences, Germany
Filter tips, 125 µl (4425)	INTEGRA Biosciences, Germany
Filter tips, 300 µl (4435)	INTEGRA Biosciences, Germany

Serological pipette 5 ml (861253001)	SARSTEDT, Germany
Serological pipette 10 ml (861254001)	SARSTEDT, Germany
Serological pipette 25 ml (861685001)	SARSTEDT, Germany
Cutfix stainless scalpel #1 (5518075)	Braun, Germany
Epoxy coated forceps (11210-10)	Fine Science Tools, Germany
Mayo scissors (14010-17)	Fine Science Tools, Germany
Fine scissors (14106-09)	Fine Science Tools, Germany
Petri dishes (82.1473)	SARSTEDT, Germany
Simport Scientific Histosette I tissue processing/embedding cassette (10181341)	Thermo Fisher Scientific, Germany
SuperFrost microscope slides (AAAA000081##32)	Thermo Fisher Scientific, Germany
Cover glass (LH25.1)	Carl Roth, Germany
Mikrotome blade Feather S35 (207500000)	Pfm Medical, Germany

2.1.2 Kits and Reagents

Table 3. Buffers and solutions.

Reagent (Ref)	**Company, Country**
HPLC dH_2O (A511.1)	Carl Roth, Germany
Sodium hydroxide (6771.3)	Carl Roth, Germany
Ethylenediaminetetraacetic acid EDTA (E9884)	Sigma-Aldrich/Merck, Germany
Tris (5429.2)	Carl Roth, Germany
Hydrochloric acid (4625.2)	Carl Roth, Germany
Ethanol >99.8 % (K928.4)	Carl Roth, Germany
Methanol (0082.3)	Carl Roth, Germany
Acetic Acid (6755.2)	Carl Roth, Germany
Taurin (4721.2)	Carl Roth, Germany

Table 4. PCR reagents.

Reagent (Ref)	Company, Country
FIREPol DNA Polymerase (01-02-01000)	Solis BioDyne, Estonia
10 x Reaction buffer B 0.8 M Tris-HCl, 0.2 M (NH4)2SO4, 0.2% w/v Tween-20 (01-02-01000)	Solis BioDyne, Estonia
25 mM $MgCl_2$ (01-02-01000)	Solis BioDyne, Estonia
dNTP set (GEN-009-250)	Rapidozym, Germany
Dimethyl sulfoxide (D4540)	Sigma-Aldrich/Merck, Germany
Phusion High-Fidelity DNA Polymerase (M0530L)	New England Biolabs, Germany
CutSmart buffer (B7204S)	New England Biolabs, Germany
HindIII (R0104S)	New England Biolabs, Germany

Table 5. Gel electrophoresis.

Reagent (Ref)	Company, Country
LE agarose (840004)	Biozym Scientific, Germany
Ethidium bromide 1 % (46067-50ML-F)	Sigma-Aldrich/Merck, Germany
GeneRuler 100 bp DNA ladder (SM024)	Thermo Fisher Scientific, Germany
GeneRuler 1 kb DNA ladder (SM0313)	Thermo Fisher Scientific, Germany
Orange G (0318.1)	Carl Roth, Germany
Xylene cyanole (CN90.1)	Carl Roth, Germany
Ficoll (A513.2)	Carl Roth, Germany
6 x gel loading dye, purple (B7024S)	New England Biolabs, Germany

Table 6. Sequencing.

Reagent (Ref)	Company, Country
Exonuclease I (M0293L)	New England Biolabs, Germany
rAPid Alkaline phosphatase (04898141001)	Roche, Germany
Exonuclease I reaction buffer (B0293S)	New England Biolabs, Germany

BigDye Terminator v1.1 & v3.1 5X sequencing buffer (4336697)	Thermo Fisher Scientific, Germany
BigDye Terminator v3.1 Cycle Seq kit (4337455)	Thermo Fisher Scientific, Germany
TERMIPol DNA Polymerase (01-03-00500)	Solis BioDyne, Estonia
Sephadex G-50 (GE17-0043-02)	Sigma-Aldrich/Merck, Germany

Table 7. RNA isolation, cDNA synthesis, expression analysis.

Reagent (Ref)	Company, Country
RNAse ZAP (R2020)	Sigma-Aldrich/Merck, Germany
TRIzol reagent (5596026)	Thermo Fisher Scientific, Germany
Chloroform (7331.2)	Carl Roth, Germany
DEPC (K028.1)	Carl Roth, Germany
Isopropanol (6752.1)	Carl Roth, Germany
Qubit RNA HS assay kit (Q32855)	Thermo Fisher Scientific, Germany
Qubit ds DNA HS assay kit (Q32854)	Thermo Fisher Scientific, Germany
Agilent RNA 6000 nano Kit (5067-1511)	Agilent Technologies, Germany
Agilent DNA 1000 kit (5067-1504)	Agilent Technologies, Germany
PrimeScript RT reagent kit (RR037A)	Takara Bio Europe, France
SYBR premix Ex Taq II (RR820B)	Takara Bio Europe, France

Table 8. Molecular cloning.

Reagent (Ref)	Company, Country
CutSmart buffer (B7204S)	New England Biolabs, Germany
HindIII (R0104S)	New England Biolabs, Germany
XhoI (M0293L)	New England Biolabs, Germany
EcoRI-HF (R0146S)	New England Biolabs, Germany
T4 DNA Ligase reaction buffer (B0202S)	New England Biolabs, Germany
T4 DNA Ligase (M0202S)	New England Biolabs, Germany
rAPid Alkaline Phosphatase (04898141001)	Roche, Germany
pEGFP-C2 vector (6083-1)	Addgene, USA

MSB Spin PCRapace (1020220200)	STRATEC, Germany
Invisorb Spin DNA Extraction Kit (1020110300)	STRATEC, Germany
XL1-Blue competent cells (200249)	Agilent Technologies, Germany
SOB medium (AE27.1)	Carl Roth, Germany
LB-medium (Luria/Miller) (X968.2)	Carl Roth, Germany
Kanamycine sulfate (60615-5G)	Sigma-Aldrich/Merck, Germany
Ampicillin sodium salt (A0166-25G)	Sigma-Aldrich/Merck, Germany
NucleoSpin plasmid, mini kit (740588.250)	MACHEREY-NAGEL, Germany

Table 9. Protein analysis.

Reagent (Ref)	Company, Country
MILLIPLEX MAP lysis buffer (43-040)	Merck, Germany
Pierce protease inhibitor tablets (A32965)	Thermo Fisher Scientific, Germany
Pierce BCA Protein-Assay (23225)	Thermo Fisher Scientific, Germany
Precision Plus protein dual color standard (1610394SP)	Bio-Rad Laboratories, Germany
Bolt 4-12% Bis-Tris plus gels, 15-well (NW04125BOX)	Thermo Fisher Scientific, Germany
20X Bolt MES SDS running buffer (B0002)	Thermo Fisher Scientific, Germany
iBlot 2 transfer stacks, PVDF (IB24001)	Thermo Fisher Scientific, Germany
NP-40 (74385)	Sigma-Aldrich/Merck, Germany
Milk powder (T145.2)	Carl Roth, Germany
Brilliant blue R (27816-25G)	Sigma-Aldrich/Merck, Germany
Tween 20 (9127.1)	Carl Roth, Germany
Western Bright ECL chemiluminescence substrate (SA62550-01)	Biozym Scientific, Germany

Table 10. Histological procedures.

Reagent (Ref)	Company, Country

Formaldehyde, ROTI Histofix 4 % (P087.6)	Carl Roth, Germany
Ethanol 70 % (T913.2)	Carl Roth, Germany
Ethanol >99.8 % (K928.4)	Carl Roth, Germany
Isopropanol (6752.1)	Carl Roth, Germany
Xylene (9713.5)	Carl Roth, Germany
Surgipath Paraplast paraffin (39601006)	Leica, Germany
H&E fast staining kit (9194.1)	Carl Roth, Germany
Hydrochloric acid 37 % fuming (4625.2)	Carl Roth, Germany
Eukitt quick-hardening mounting medium (03989)	Sigma-Aldrich/Merck, Germany
Direct red 80 25 % (365548)	Sigma-Aldrich/Merck, Germany
Picric acid solution 1.3% in H_2O (P6744)	Sigma-Aldrich/Merck, Germany
Acetic acid (6755.2)	Carl Roth, Germany
Hematoxylin solution A acc. to Weigert (X.906.1)	Carl Roth, Germany
Hematoxylin solution B acc. to Weigert (X.907.1)	Carl Roth, Germany
Saponin (47036-50G-F)	Sigma-Aldrich/Merck, Germany
NP-40 (74385)	Sigma-Aldrich/Merck, Germany
Albumin Fraction V, BSA (T844.4)	Carl Roth, Germany
Fluoromount-G mounting medium (E17984-25)	Science Services, Germany

Table 11. Antibodies and stains for histology.

Antibody/stain (Ref)	Company, Country	Host	Dilution
α-Sma (A2547)	Sigma-Aldrich/Merck, Germany	mouse	1:200
Col1 (ab21286)	Abcam, United Kingdom	rabbit	1:200
anti-mouse Alexa568 (A-11031)	Thermo Fisher Scientific, Germany	goat	1:500
anti-rabbit Alexa647 (A-21245)	Thermo Fisher Scientific, Germany	goat	1:500
DAPI (D1306)	Thermo Fisher Scientific, Germany		1:300
WGA (W11261)	Thermo Fisher Scientific, Germany		1:100

Table 12. Antibodies for Western blots.

Antibody (Ref)	Company, Country	Host	Molecular weight [kDa]	Dilution
Hsp70 (ADI-SPA-820)	Enzo Life Sciences, Switzerland	mouse	72-73	1:1000
Cox4-I1 (AF5814)	R&D Systems, USA	goat	18	1:200
OxPhos rodent WB Ab cocktail (#45-8099)	Thermo Fisher Scientific, Germany	mouse	20, 30, 48, 35-40, 55	1:1000
Sdha (#11998)	Cell Signaling, Germany	rabbit	70	1:1000
Tom20 (#42406)	Cell Signaling, Germany	rabbit	16	1:1000
anti-mouse HRP (7076S)	Cell Signaling, Germany	horse		1:1000
anti-rabbit HRP (#7074)	Cell Signaling, Germany	goat		1:1000
anti-goat HRP (A16005)	Thermo Fisher Scientific, Germany	donkey		1:1000

Table 13. Primers

Gene (transcript)	Primer	Sequence (5' -> 3')	Length [bp]	Melting temperature[°C]
Primers for genotyping				
Prdm16				
(ENSMUST00000105638.8)	Exon 7 forward	TGCACGCATTCCAATCTC	18	53.70
	Exon 7 reverse	ATTTCACAGCAGGGTGGAG	19	56.70
Primers for characterisation of splice variants				
Prdm16				
(ENSMUST00000105638.8)	Exon 3 forward	CCCAGGAGAGCTGCATCAAA	20	60.03
	Exon 9 reverse	ACTGCGTGTAGGACTTGTGG	20	59.40
	Exon 6 forward	AGCTCTACGAGGGCCTAGG	19	59.85
	Exon 8 reverse	GGATGTGACGCTGGAGGTT	19	59.70
Primers for cloning				
Prdm16	Exon 5 forward	ctcagatCTCGAGCTTGCATGTGAAAGAAGGTG		
(ENSMUST00000105638.8)	XhoI	CC	35	59.04
	Exon 8 reverse			
	EcoRI	actgGAATTCGCTGTTTGAGGCCAGAGGAT	30	59.70
Primers for Sanger sequencing				

Prdm16 (ENSMUST00000105638.8)	Exon 5 forward	TGCATGTGAAAGAAGGTGCC	20	59.04
	Exon 8 reverse	GGATGTGACGCTGGAGGTT	19	59.70
	EGFP_C_3_f	CATGGTCCTGCTGGAGTTCGTG	22	68.10
Primers for qPCR				
Prdm16 (ENSMUST00000105638.8)	Exon 3 forward	CCCAGGAGAGCTGCATCAAA	20	60.03
	Exon 4 reverse	ACGGATGTACTTGAGCCAGC	20	60.11
	Exon 6 forward	AGGATTGCGAGCGGATGTTC	20	62.00
	Exon 7 reverse	CCAGTTGAAGGCCTTGGGAC	20	64,00
	Exon 7 forward	GAAGTCCAACCTCATCCGCC	20	64.00
	Exon 8 reverse	ATGTGACGCTGGAGGTTGC	19	60.00
	Exon 14 forward	GAACCAGGCATCCACTCGAA	20	60.04
	Exon 15 reverse	CTACGTCCTCTGGCTTTGCA	20	60.04
Nppb (ENSMUST00000103231.4)	Exon 1 forward	TCCTTTATCTGTCACCGCTGG	21	59.80
	Exon 2 reverse	GTCTCTGGGCCATTTCCTCC	20	61.40
Actn2 (ENSMUST00000064204.13)	Exon 11 forward	GCCTCCACGCACGAGACATG	20	59.75
	Exon 12 reverse	TGCTTCCGAAGTAGGGCTCGA	21	59.68

Actc1 (ENSMUST00000090269.6)	Exon 2 forward	CTGGTGAAGGCCGGCTTTGC	20	60.75
	Exon 3 reverse	TCCTTCTGTCCCATACCCACCA	22	59.31
Dsp (ENSMUST00000124830.2)	Exon 11 forward	CGGAACCCAGACTACAGGAGCA	22	60.16
	Exon 12 reverse	GCGCTCGTTGTTGTCCTTCAGA	22	59.74
Myh6 (ENSMUST00000081857.13)	Exon 3 forward	GTTAAGGCCAAGGTCGTGTCCC	22	59.72
	Exon 4 reverse	ACTTGGGTGGGTTCTGCTGC	20	59.37
Myh7 (ENSMUST00000168485.7)	Exon 25 forward	CCAAGGCCAAGGTCAAGCTGG	21	60.20
	Exon 26 reverse	GCTTCCGCTTGGCTCGCTC	19	60.17
Myl3 (ENSMUST00000079784.11)	Exon 1 forward	GGAAGCCGAGTTTGATGCCTCC	22	60.07
	Exon 3 reverse	TCCCCACACTGCCCGTATGT	20	59.93
Tcap (ENSMUST00000008021.2)	Exon 1 forward	AACGCAGGGAAGCCTTCTGG	20	59.09
	Exon 2 reverse	GCCGGTGGTAGGTCTCATGC	20	59.11
Tnnt2 (ENSMUST00000112087.8)	Exon 3 forward	ACTGGAGTGAAGAAGAGGAGGACG	24	59.93
	Exon 4 reverse	GCCTCCTCTGTCTCAGCCTCA	21	59.77
Tpm1 (ENSMUST00000113707.8)	Exon 2 forward	GAAACTGGAGCTGGCGGAGAAA	22	59.44
	Exon 3 reverse	TCCTGAGCACGATCCAACTCCT	22	59.69
Ttn (ENSMUST00000111846.8)	Exon 5 forward	CACCAACCCCATCTCCAGTCAG	22	59.04

	Exon 6 reverse	GTGGTGGTCTGAGTCTTGCGAAT	23	59.34
*Ank (*ENSMUST00000022875.6)	Exon 4 forward	CTGGTGGGATGTGCCTCAA	19	58.80
	Exon 5 reverse	AGCAAAATGGCTACGAAAACAAC	23	57.10
Gapdh (ENSMUST00000118875.7)	Exon 3 forward	GGGAAGCCCATCACCATCTT	20	59.30
	Exon 3 reverse	CGGCCTCACCCCATTTG	17	57.60

2.1.3 Devices

Table 14. Devices.

Device	Company, Country
LF90II Body composition analyzer	Bruker, Germany
CODA tail-cuff system	Kent Scientific, USA
ecgTUNNEL system	EMKA Technologies, France
Double-chamber plethysmograph	EMKA Technologies, France
Vevo 2100 imaging system	FUJIFILM VisualSonics, Canada
Vortex Genie 2	Bender & Hobein, Switzerland
Centrifuge Heraeus Pico21	Eppendorf, Germany
Centrifuge 5804R	Eppendorf, Germany
Minicentrifuge FV-2400 Mikro-Spin	Biosan, Latvia
Centrifuge 3K30	Sigma, Germany
Thermomixer 5436	Eppendorf, Germany
Thermomixer comfort	Eppendorf, Germany
Microwave	SEVERIN, Germany
pH-meter 766	Knick, Germany
NanoDrop Spectrophometer ND-1000	PEQLAB, Germany
DNA Engine Tetrad 2 Peltier thermal cycler	Bio-Rad Laboratories, Germany
Applied Biosystems 7500 Real Time PCR system	Thermo Fisher Scientific, Germany
Applied Biosystems 3730xl DNA analyzer	Thermo Fisher Scientific, Germany
Explorer GT2100 scale	OHAUS, Switzerland
AB 104 fine scale	Mettler-Toledo, Germany
Qubit 3 fluorometer	Thermo Fisher Scientific, Germany
Spark 10Ms multiplate reader	Tecan, Switzerland
Hoefer HE 99X Max Submarine electrophoresis unit	Thermo Fisher Scientific, Germany
Biometra Power Pack P25	Analytik Jena, Germany

PowerPac Basic Power Supply	Bio-Rad Laboratories, Germany
Biometra UV transilluminator BioDocAnalyze	Analytik Jena, Germany
Polymax 1040 shaker	Heidolph Instruments, Germany
Analogue tube roller SRT9	Cole-Parmer, United Kingdom
iBlot 2 Dry blotting system	Thermo Fisher Scientific, Germany
LEO transmission electron microscope 906	Carl Zeiss, Germany
Laser scanning microscope 700	Carl Zeiss, Germany
STP 120 spin tissue processor	Thermo Fisher Scientific, Germany
EG 1160 embedding station	Leica, Germany
Thermo Scientific™ HM 340E electronic rotary microtome	Thermo Fisher Scientific, Germany
Pannoramic MIDI II slides canner	Sysmex, Germany
Chemiluminescence imaging system CHEMI only	VWR International, Germany
Water bath TWB5	JULABO, Germany
Incubator BD53	BINDER, Germany
2100 Bioanalyzer	Agilent Technologies, Germany
T 10 basic ULTRA-TURRAX disperser	IKA, Germany

2.1.4 Software

Table 15. Software.

Software	Company, Country
CorelDRAW Graphics Suite 2019	Corel Corporation, Canada
Microsoft Office 2016	Microsoft Corporation, USA
CaseViewer 2.3	3DHISTECH Ltd, Hungary
Pannoramic Control Software	Sysmex Deutschland GmbH, Germany
ZEN 3.0	Carl Zeiss, Germany
Axio Vision Rel. 4.8.2	Carl Zeiss, Germany
Agilent 2100 Expert Software B.02.08	Agilent Technologies, Germany
ABI Sequencing Analysis 5.1.1	Thermo Fisher Scientific, Germany

LaserGene SeqMan Pro 14	DNASTAR, USA
Applied Biosystems 7500 Real-Time PCR Software	Thermo Fisher Scientific, Germany
Capture software for VWR CHEMI only	VWR International, Germany
GelQuant.Net V 1.7.8	BiochemLabSolutions, USA

2.2 Methods

2.2.1 Animal handling

Viable controls (*Prdm16*$^{wt/wt}$) and heterozygous (*Prdm16*$^{csp1/wt}$) mice of the FVB.C-Prdm16^{csp1}/J mouse strain were purchased from Jackson Laboratories, USA (JAX stock #013100) at the age of 2 months. Mice were maintained with a twelve-hour day and night cycle and unlimited access to food under specific pathogen-free conditions for another 6 months in the animal facility of the Max-Delbrück-Center, Berlin (Stefanie Schelenz, Martin Taube, Dr. Arnd Heuser). The strain was originally created by N-ethyl-N-nitrosourea (ENU) induced mutagenesis and carries the *csp1* mutation, an intronic splice acceptor site mutation (c.888-3C>A) in the *Prdm16* gene (30). Dr. Kuehnisch received approval for the handling, physiological characterisation, and sacrifice of the mice by the Landesamt für Gesundheit und Soziales Berlin (LAGeSo), Germany (G0070/17; date accepted: 10.07.2017). All experiments were conducted or supervised by him. After physiological evaluation, animals were sacrificed with isoflurane and by decapitation. Tissue was collected and either snap-frozen in liquid nitrogen or fixed in a 4 % PFA solution.

2.2.2 Genotyping

Genotyping of mice occurred according to an established protocol (30). Briefly, the *csp1* mutation introduces a new cleavage site for the restriction enzyme *HindIII,* causing a restriction fragment length polymorphism (RFLP) in *Prdm16*$^{csp1/wt}$ mice. DNA was extracted from tail tip biopsies (95°C, 50 min in 25 mM NaOH, 0.2 mM EDTA followed by neutralisation with 40 mMol Tris-HCl, pH 5) and used as a template for endpoint PCR (Table 16 - Table 17). The 344 bp PCR product was subsequently digested by *HindIII* (2.8 U/µl, 37 °C, > 2 h). Digested PCR products were separated in a 1.5 % agarose gel in TTE (Tris 0.09 M, taurin 0.03 M, EDTA 1 mM), containing 0.5 mg/ml ethidium bromide and visualised with an UV transilluminator. Control mice only showed the 344 bp product, whereas heterozygous *Prdm16*$^{csp1/wt}$ mutants showed

additional bands at 211 bp and 133 bp. The primer sequence can be found in Table 13.

Table 16. Genotyping PCR.

Compound	Volume 1 x assay [µl] (final concentration)
HPLC water	12.2
10 x buffer B	2.0
$MgCl_2$ (25 mM)	1.2 (1.5 mM)
dNTPs (10 mM)	0.4 (0.2 mM)
FIREPol DNA Polymerase	0.2 (0.05 U/µl)
Prdm16 Exon 7 forward primer (10 µM)	1.0 (0.5 µM)
Prdm16 Exon 7 reverse primer (10 µM)	1.0 (0.5 µM)
DNA template	2.0

Table 17. Touchdown PCR cycling program for Genotyping.

Step	Temperature [°C]	Duration	Cycles
Activation	94	2 min	1
Denaturation	94	20 sec	2 x at 65 °C - 61°C
Annealing	65 > 64 > 63 > 62 > 61 > 60	15 sec	30 x at 60 °C
Elongation	72	1 min	
Final elongation	72	10 min	1
Hold	4	forever	-

2.2.3 Pathophysiological measurements

The phenotype of *Prdm16*$^{csp1/wt}$ mice and viable controls was evaluated with echocardiography, electrocardiography, blood pressure measurement, body composition analysis, and respiratory analysis at the animal phenotyping platform of the Max-Delbrück-Center, Berlin (Dr. Arnd Heuser). Except for echocardiography, all procedures lasted for only a few minutes and the animals were moved back into the animal facility at once.

The cardiac function of mice was evaluated in *echocardiography*. For anaesthesia, a 2.5 % isoflurane oxygen mixture was used in a tempered chamber. Mice inhaled the mixture during the entire procedure (5-10 min). After the removal of chest hair, mice were fixed on a heated plate. Electrocardiograms and respiratory rates were recorded. The body temperature was measured rectally and kept stable using a heating lamp. Stroke volume (SV) and cardiac output (CO) were measured in parasternal long axis view. Wall dimensions, ejection fraction (EF), and fractional shortening (FS) were quantified in M-mode and B-mode images. Mitral flow profiles were measured in the apical 4-chamber view by Pulsed wave Doppler (PWD). Tissue Doppler imaging (TDI) was used to analyse diastolic annular velocities at the mitral annulus.

Body composition analysis. Distribution of body fat, free water and muscle tissue was measured with an NMR-spectroscopic method.

The non-invasive CODA tail-cuff system was used for *blood pressure measurements* in a shaded, tubular, and tempered analysis chamber.

Electrocardiography. Electrocardiograms were recorded with 4 electrodes via the mouse paws in the ecgTUNNEL system.

Respiratory analysis. A double-chamber plethysmograph enabled the evaluation of respiratory function in mice. During the measurement, changes of respiratory volume and the analysis chamber were comparatively calculated. The thoracal and nasal flow data were dynamically calculated.

2.2.4 Histomorphological analysis

Tissue processing and fixation. Freshly collected organs of 8-month-old animals were fixed in a 4 % formaldehyde solution (4 °C, 1 - 5 d) and washed twice in PBS (NaCl 0.14 M, KCl 2.7 mM, Na_2HPO_4-$2H_2O$ 0.01 M, KH_2PO_4 1.8 mM, pH7.4). Fixed organs were dehydrated via the ascending alcohol series (70 % - 80 % - 96 % - Isopropanol), cleared in xylene and embedded in paraffin. Then, embedded tissue was sectioned with a rotary microtome to a slice thickness of 4 µM, transferred to slides and allowed to dry at room temperature overnight. Prior to all staining procedures, slides were

dewaxed in xylene and rehydrated with a descending alcohol series (100 % - 90 % - 70 % - dH_2O).

Picro-Sirius Red staining was used for the detection of collagen deposition. After labelling of the nuclei by immersion in Weigert's hematoxylin (1:1 mixture of hematoxylin solution A/B acc. to Weigert) for 8 minutes and blueing in running tap water for 10 minutes, sections were stained with Picro-Sirius red solution (1 g Direct red 80 in 1 L 1.3 % picric acid solution) for 1 hour. Finally, sections were washed in 2 changes of 0.5 % acetic acid, dehydrated in 3 changes of 100 % ethanol, cleared in xylene and mounted.

H&E staining was used to screen for structural defects in murine hearts. The procedure was performed using the H&E fast staining kit according to the manufacturer's instructions. Briefly, sections were incubated in hematoxylin, differentiated with HCl (0.1 %), blued in running tap water, stained with Eosin Y, rinsed in tap water, dehydrated, and finally mounted.

After *image acquisition* with the Pannoramic MIDI II slide scanner, qualitative analysis was carried out for fibrotic depositions and structural alterations.

Immunofluorescence and fluorescence staining. The expression and localisation of different proteins and the size of cardiomyocytes was assessed by immunostaining. Therefore, dewaxed and rehydrated sections were washed 3 times in PBS, permeabilised (0.3 % Saponin, 0.1 % NP-40 in PBS) for 30 minutes, washed again 3 times in PBS, and blocked in 3 % bovine serum albumin (BSA) diluted in PBS for 1 hour. After another washing step, primary antibody incubation took place for 1 hour. Then, sections were washed in PBS 4 more times and incubated with secondary antibodies for 20 minutes. The stained sections were washed 4 times again and mounted. All antibodies were diluted in 3 % BSA in PBS. Wheat germ agglutinin (WGA) was used to label cell membranes in the primary antibody incubation step. The nuclei were labelled with 4′,6-diamidino-2-phenylindole (DAPI) during the second last washing step. Dilution factors of all antibodies and stains can be found in Table 11. Images were acquired with the Leica LSM700 confocal microscope.

Cross-sectional areas of cardiomyocytes were quantified with ZEN 3.0. The contours, of at least 200 independent cardiomyocytes for each animal were manually drawn with the spline tool.

2.2.5 Ultrastructural analysis

Tissue preparation. Small pieces of left ventricular tissue collected from *Prdm16*$^{csp1/wt}$ mice and controls were fixed in 2.5 % glutaric aldehyde in 0.1 M cacodylate buffer (pH 7.3). Postfixation, epoxy embedding, staining, semithin sectioning, and ultrathin sectioning was performed according to standard protocols by the Core Facility for Electron Microscopy of the Charité University Hospital, Berlin (Dr. Sara Timm, Petra Schrade).

Image acquisition and analysis. Transmission electron micrographs were acquired with the LEO Transmission electron microscope and analysed with Axio Vison and ZEN3.0. The length of fully contracted sarcomeres was measured between the middle of two z-discs with the line tool in ZEN 3.0. At least 200 independent sarcomeres per animal were evaluated. The mean and standard deviation were calculated for each genotype. Axio Vison was used to quantify sarcomere and mitochondrial areas in TEM images. First, the region of interest (ROI) was defined, and artefacts were excluded. Then, the total sarcomere area was determined with the contour tool and each mitochondrion was measured. Total mitochondrial area, mitochondrial count, and sarcomere area were normalised to the ROI area.

2.2.6 Molecular Analysis

Expression analysis

RNA isolation. RNA was isolated from interventricular septum and lung tissue. Samples were mechanically powdered in liquid nitrogen immersed in 1000 µl TRIzol reagent and homogenised. For phase separation, 200 µl chloroform was added, and the mixture was shaken vigorously and left at room temperature for 15 minutes. After centrifugation (10000 x G, 4 °C, 15 min), the upper RNA containing phase was transferred into RNAse free tubes. Precipitation of RNA was realised by addition of 500 µl isopropanol, incubation at room temperature for 10 minutes and centrifugation (10000 x G, 4 °C, 10 min). For washing purposes, RNA pellets were immersed in 75

% Ethanol (diluted in DEPC water) and spun down (10000 x G, 4 °C, 5 min) twice. In the final step, RNA was dried at 80°C briefly and dissolved in DEPC water.

RNA quality control. To assure the integrity of isolated RNA, the Agilent RNA 6000 nano was used according to the manufacturer's instructions. Samples were run on the 2100 Bioanalyzer and analysed with the Agilent 2100 expert software.

cDNA synthesis. Before the synthesis of cDNA, the RNA concentrations in isolates were measured to ensure proper sample dilution. Therefore, samples were measured with the NanoDrop spectrophotometer preliminarily. Accurate quantification was realised with the Qubit RNA HS assay kit using the Qubit 3 fluorometer. Finally, RNA was reverse transcribed into cDNA with the Takara PrimeScript RT reagent kit according to the manufacturer`s instructions.

qPCR. Expression analysis of sarcomere genes and *Prdm16*^{csp1} splice isoforms was performed with qPCR. The Takara SYBR premix Ex Taq II was used on the Applied Biosystems 7500 Real-Time PCR system as instructed in the manual. Samples were measured in duplicates and normalised to the endogenous controls Glyceraldehyde-3-phosphatase dehydrogenase (*Gapdh*) and Progressive ankylosis protein (*Ank*) with the ΔΔCt method (63). Sequences of exon spanning qPCR primers can be found in Table 13.

RNAseq. RNA was prepared and tested for sufficient quality as described above. Further handling of samples and data analysis occurred at the Berlin Institute of Health, Core Unit Genomics (Dr. Tatiana Borodina, Dr. Sascha Sauer) and Bioinformatics (Dr. Benedikt Obermayer, Dr. Dieter Beule). Briefly, library preparation was realized with the TruSeq stranded mRNA kit (Illumina, USA). Reads were aligned with STAR (v2 6.1a) against the GRCm38 reference. Quantification occurred in R (v3.4.1) using featureCounts (v1.6.3) with the Gencode vM12 annotation. Differential expression was assessed with DESeq2 (Bioconductor, USA) and defined for genes with a $\log_2$ fold change (LFC) (*Prdm16*$^{wt/wt}$ vs. *Prdm16*$^{csp/wt1}$) < -0.5 or > 0.5; normalised counts ≥ 50, and $p \leq 0.01$ in two-tailed t-test.

Analysis of aberrant splicing

PCR analysis of aberrant splicing. The first attempt to study the influence of the *csp1* mutation on splicing was conducted by endpoint PCR with cDNA templates generated from total RNA isolates of heart and lung tissue (see above). Primers were designed to cover as much sequence of the *Prdm16* transcript as possible with standard PCR protocols (Table 18, 19). The primer sequence can be found in Table 13. PCR products were separated in an agarose gel (1 % in TTE, 0.5 mg/ml ethidium bromide), and visualised under an UV lamp. Bands of amplified splice products were cut out and eluted in HPLC dH_2O (50 °C, 40 min), and used as template for nested PCR (Table 18 ,Table 19). Separation and visualisation of the nested PCR was realised using the 2100 Bioanalyzer and the DNA 1000 kit according to the manufacturer's instructions.

Table 18. PCR for analysis of aberrant splicing and molecular cloning.

Compound	Volume 1 x assay [µl] (final concentration)
HPLC water	22.35
10 x Buffer B	4.0
$MgCl_2$ (25 mM)	2.4 (1.5 mM)
dNTPs (10 mM)	0.8 (0.2 mM)
FIREPol DNA Polymerase	0.4 (0.05 U/µl)
Phusion High-Fidelity DNA Polymerase	0.05 (0.0025 U/µl)
Forward primer (10 µM)	2.0 (0.5 µM)
Reverse primer (10 µM)	2.0 (0.5 µM)
DNA template	4.0

Table 19. Cycling conditions of PCR for analysis of aberrant splicing and molecular cloning.

Step	Temperature [°C]	Duration	Cycles
Activation	95	5 min	1
Denaturation	95	30 sec	2 x with 60 °C - 56 °C 35 x with 60 °C
Annealing	60 > 58 > 56 > 54	45 sec	
Elongation	72	1 min	
Final elongation	72	10 min	1
Hold	4	forever	-

Molecular cloning was used in a second attempt to isolate *Prdm16* splice isoforms. Gel-isolated PCR products of the splice isoforms (see above) were further amplified in cloning PCR with specific restriction sites for XhoI and EcoRI (Table 18, Table 19) to generate DNA inserts. A small amount of the reaction was used to monitor the success of the cloning PCR in an agarose gel (1.25 % in TTE, 0.5 mg/ml ethidium bromide). The remains of the reaction were digested with XhoI and EcoRI-HF (37 °C, 2.5 h). DNA inserts were purified with MSB Spin PCRapace spin columns. 4.43 µg of the target p-EGFP-C2 vector were digested (37°C, 16 h) and its open DNA ends were dephosphorylated with SAP (37°C, 15 min) to prevent self-ligation. The digested vector was purified by electrophoresis in an agarose gel (1 % in TTE, 0.5 mg/ml ethidium bromide) and eluted with the Invisorb Spin DNA Extraction Kit. Ligation was performed with T4 DNA Ligase (16 °C, 4 h, followed by room temperature, 10 min). For the transformation, freshly thawed XL1-Blue Competent Cells were mixed with ligated vectors and β-mercaptoethanol, and underwent a heat shock in a water bath (42 °C, 45 sec). Afterwards cells were cooled down on ice for 2 minutes, incubated in SOB medium (37°C, 30 min), plated on LB Agar with the corresponding antibiotic kanamycine for selection and left at 37 °C overnight. The pUC18 plasmid was used as positive control for transformation. After successful growth, clones were picked to inoculate a master plate. Colony PCR identified clones containing an insert. Primer Sequence and PCR conditions can be found in Tables 13 and 19. Then, positive clones were incubated in liquid LB medium (37°C, overnight) and their plasmids were isolated with the NucleoSpin Plasmid Mini kit. Plasmid concentrations were measured with the NanoDrop spectrophotometer. Eluted plasmids were visualised with an UV transilluminator in an agarose gel (1 % in TTE, 0.5 mg/ml ethidium bromide).

Sanger Sequencing. For the sequencing reaction, 100 - 200 ng of plasmid was used as a template. For verification of the *csp1* mutation, murine gDNA was PCR amplified as described in 2.2.2, and purified prior to sequencing (rAPid Alkaline Phosphatase and Exonuclease I; 37°C, 30 min; 72°C, 15 min; 4°C, forever). The protocol of the BigDye Terminator v3.1 cycle sequencing kit was optimised to 0.5 x amount of BigDye Terminator solution and an additional 0.05 U/µl TERMIPol DNA Polymerase for longer stable sequencing strands. Sequencing primers are listed in Table 13. Before running the reaction on the 3730 DNA Analyzer, sequencing reactions were purified with Sephadex G-50 agarose gel and diluted in 10 µl H_2O. Base calling and sequence

analysis were realised with ABI sequencing analysis and LaserGene Seqman Pro 14 software, respectively. The obtained sequences were aligned to exon 6 - 8 of the wild-type *Prdm16* sequence (ENSMUST00000030902.12).

For t*argeted high-throughput sequencing,* nested PCR products, generated as described above, were sent to GENEWIZ (Leipzig, Germany). Data analysis was done at the Berlin Institute of Health, Core Unit Bioinformatics (Dr. Benedikt Obermayer, Dr. Dieter Beule). Briefly, the fragment length was calculated from raw sequencing reads by pairwise alignment using the globalms method in the pairwise2 python package. Reads were aligned to the Prdm16 reference sequence (ENSMUSG00000039410) with STAR (v2.7.3a). Aligned fragments between 235 and 255 nt were inspected for gaps of over 50 nt.

Protein analysis

For *protein isolation,* murine heart tips were mechanically powdered in liquid nitrogen immersed in MILLIPLEX MAP Lysis buffer (plus Pierce Protease Inhibitor Tablets) and homogenised with an IKA Ultra-turrax disperser.

Concentration measurements. The protein concentrations of lysates were measured using the Pierce BCA Protein Assay according to the manufacturer's instructions. Briefly, the assay is based on the reduction of Cu^{2+} to Cu^{1+} by proteins in alkaline medium and the chelation of Cu^{1+} by bicinchoninic acid (BCA), which creates a complex with strong light absorbance at 562 nm. Diluted samples (1:15) and BSA standards were incubated as duplicates with working reagent on a microplate (37°C, 30 minutes). Absorption was measured with the Spark 10M multiplate reader (562 nm). Microsoft Excel was used for the creation of a linear standard curve and the calculation of concentrations.

Western blot Analysis. 30 µg of protein were separated by electrophoresis in Bolt 4-12 % Bis-Tris Plus Gels and transferred to an iBlot 2 Transfer Stacks PVDF membrane. Gels were stained with coomassie (0.025 % Brilliant Blue R250, 40 % methanol, 7 % acetic acid in dH_2O) to assure that the same amount of protein was loaded. After blocking in 5 % milk powder and 0.2 % NP-40 in TBS-T (Tris 0.2 M; NaCl 1.4 M; Tween20 9 mM) (room temperature, 1 h), membranes were incubated with primary

antibodies (4 °C, overnight), followed by 4 washing procedures in TBS-T and incubation with secondary antibody horseradish peroxidase (HRP)-conjugates (room temperature, 1 h). All antibodies were diluted in the blocking buffer. Dilution factors are listed in Table 12. Before the detection of marked proteins, membranes were washed 4 more times in TBS-T. Then, membranes were incubated with Western Bright ECL chemiluminescence substrate (1:1 mix of luminol/ECL enhancer and peroxide) for 1 minute. The emitted light was measured with a chemiluminescence imaging system with exposure times ranging from 1 sec to 10 min. The obtained signals were quantified with GelQuant.Net.

2.2.7 Metabolic analysis

The central carbon metabolism in interventricular septum tissue of *Prdm16*$^{csp1/wt}$ mice and viable controls was analysed with *Gas chromatography–mass spectrometry* (GC-MS) at the Berlin Institute of Health, Core Unit Metabolomics (Dr. Raphaela Fritsche-Guenther, Alina Eisenberger, Dr. Jennifer Kirwan) according to standard protocols. The chromatograms were processed with the ChromaTOF software (LECO Corporation, USA). Data was analysed in Microsoft Excel and R Studio. Peak area values of detected metabolites were normalised to cinnamic acid. Differential levels of single metabolites were detected with the $\log_2$ from the ratio of normalised peak area between *Prdm16*$^{wt/wt}$ and *Prdm16*$^{csp1/wt}$ (> 0.2 or < 0.2 and $p \leq 0.05$ in two-tailed t-test). For univariate scaled analysis of metabolite groups, individual values were transformed (value-mean/standard deviation) and categorised as increased if > 0 or decreased if < 0. Here, Pearson's chi-squared test was used to calculate statistical significance between groups.

2.2.8 Statistical analysis

Data capture and statistical analysis was performed with Microsoft Excel. For each individual group, mean and standard deviation were calculated. Normal distribution of measurements was evaluated in histograms. Differences between two groups were assessed by unpaired student's t-test. Statistical significance was set at $p \leq 0.05$. Data analysis of RNAseq and GC-MS occurred at the Berlin Institute of Health, Core Unit Bioinformatics, and Core Unit Metabolomics, respectively, and is described in the corresponding sections above.

3 Results

3.1 Aberrant splicing in *Prdm16*$^{csp1/wt}$ mice

3.1.1 Sequence and genomic location of the *csp1* mutation

Sanger sequencing of DNA, obtained from murine tail tips, showed the presence of the described *csp1* mutation (ENSMUSG00000039410: g.30020C>A; ENSMUST00000030902.12: c.888-3C>A) in heterozygous *Prdm16*$^{csp1/wt}$ mice (Figure 7 A). The mutation locates to the splice acceptor site in intron 6-7 of the *Prdm16* gene, comprising 17 exons in total (Figure 7 B).

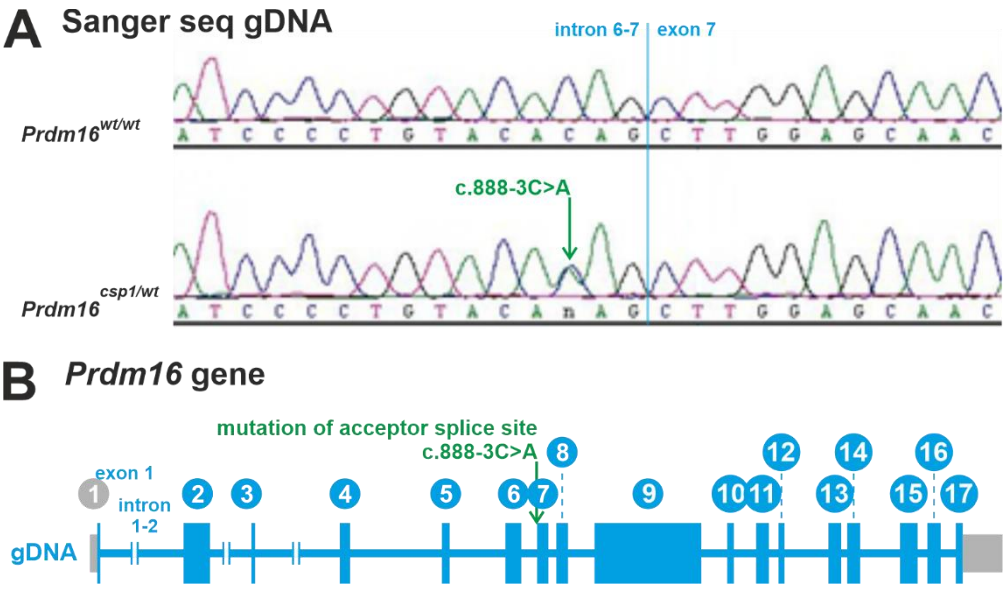

Figure 7. Sanger sequencing of the *csp1* mutation. A Sequence of *Prdm16* gDNA in the region of intron 6-7 and exon 7. The green arrow indicates the C>A base exchange in the mutant *csp1* allele. The blue line marks the beginning of exon 7. **B** The *Prdm16* gene comprises 17 exons and 16 introns. The *csp1* mutation affects the splice acceptor site in intron 6-7.

3.1.2 Genotyping of *Prdm16*$^{csp1/wt}$ mice

The *csp1* mutation introduces a new cleavage site for the restriction enzyme *HindIII* (30). End point PCR amplified a 344 bp piece of *Prdm16* gDNA containing the mutation. After *HindIII* digestion, heterozygous *Prdm16*$^{csp1/wt}$ mice showed two additional bands of 211 bp and 133 bp length corresponding to the cleaved mutant allele (Figure 8).

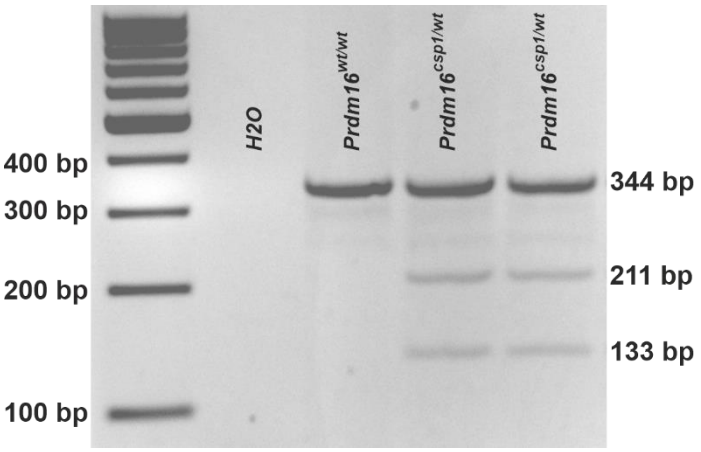

Figure 8. Genotyping of *Prdm16$^{csp1/wt}$* animals. The figure shows a representative image of HindIII digested PCR products, separated in an agarose gel. The 344 bp product corresponds to wild-type *Prdm16*. The two additional bands appeared only in *Prdm16$^{csp1/wt}$* mice as a result of the cleaved mutant *csp1* allele.

3.1.3 Identification of *Prdm16^{csp1}* splice isoforms

To study the impact of the *csp1* mutation on *Prdm16* pre-mRNA splicing, total RNA from heart and lung was transcribed into cDNA. Unexpectedly, PCR amplification and subsequent agarose gel analysis of *Prdm16* revealed the presence of three splice products in *Prdm16$^{csp1/wt}$* mutants. Next to the expected bands at 806 bp (*wt*) and 658 bp (*exon 7 skipping*), electrophoresis detected another product at ~ 780 bp (Figure 9 A). Nested PCR of the gel-isolated product at ~ 780 bp was visualised with a high-resolution Bioanalyzer and yielded three products at 297 bp (*wt*), 149 bp (*exon 7 skipping*), and ~ 270 bp (*unknown*) (Figure 9 B). As PCR amplification of the ~ 780 bp band did not produce a single band with ~ 270 bp, direct Sanger sequencing could not be applied for further characterisation of the unknown product.

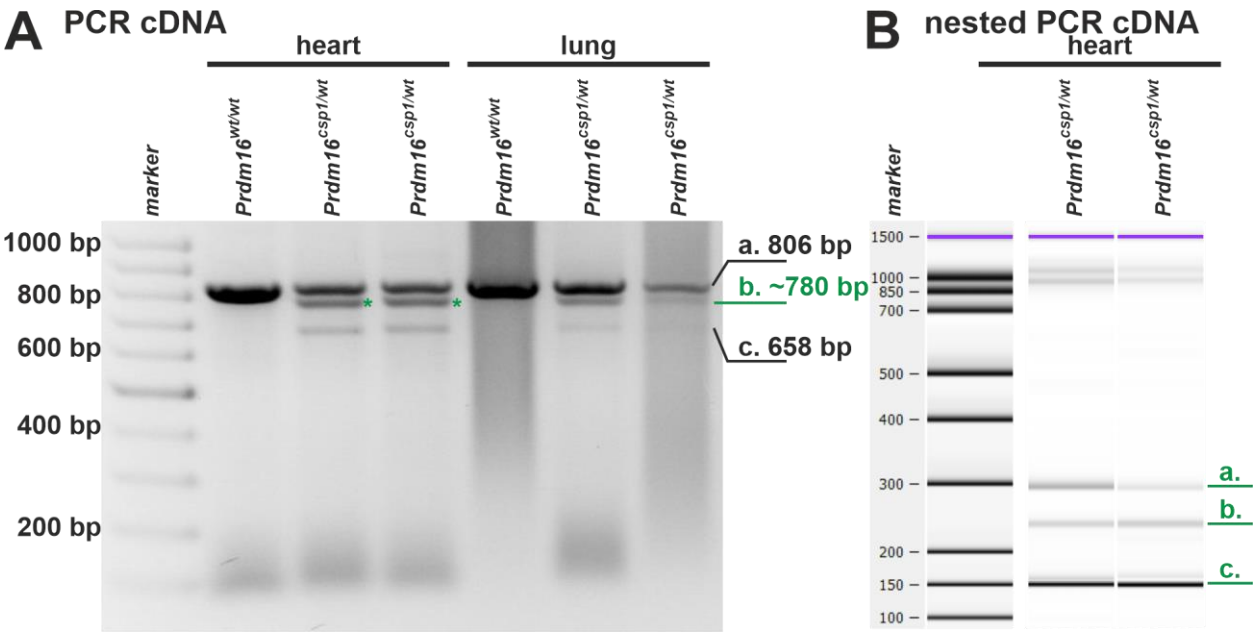

Figure 9. Affected splicing due to the *csp1* mutation. A Amplification of cDNA and agarose gel analysis showed the presence of three alternative splice products in *Prdm16*$^{csp1/wt}$ animals: a. – *wild-type* splice isoform; b. – *unknown* transcript; c – mutant isoform resulting from *exon 7 skipping*. The green stars indicate the templates for further amplification in nested PCR. **B** Nested PCR of the isolated unknown band (b.) produced three different bands as visualised by Bioanalyzer gel electrophoresis.

As gel purification failed to isolate splice products for direct Sanger sequencing, we approached characterisation of the *csp1* splice isoforms by molecular cloning. Cloning PCR of gel isolates of 806 bp (*wt*) and ~ 780 bp (*unknown*) bands (compare Figure 9 A) with recognition sites for restriction enzymes produced bands at 531 bp (*wt*), ~ 505 bp (*unknown*) and 383 bp (*exon 7 skipping*) (Figure 10 A). These products were inserted into the multiple cloning site (MCS) of a pEGFP-C2 vector via sticky end ligation and transformed in chemocompetent cells. Successfully transformed clones were selected on agar plates by antibiotic resistance (kanamycine). Gel electrophoresis of colony PCR showed bands with the expected lengths for insertion of the *wt*-, *exon 7 skipping*-, or the *unknown* isoform at ~ 750, 724, and 602 bp. However, the small difference in length between the *wt*- and the *unknown* isoform made it impossible to discriminate the isoforms in an agarose gel (Figure 10 B). Further analysis by Sanger sequencing revealed that the *unknown* splice product was not inserted in any plasmid construct. We only obtained the sequence for the *wt*- and *exon 7 skipping* inserts, the empty vector backbone, or nonsense sequence (Figure 10 B - C). Therefore, molecular cloning failed to characterise *Prdm16*^{csp1} splice isoforms.

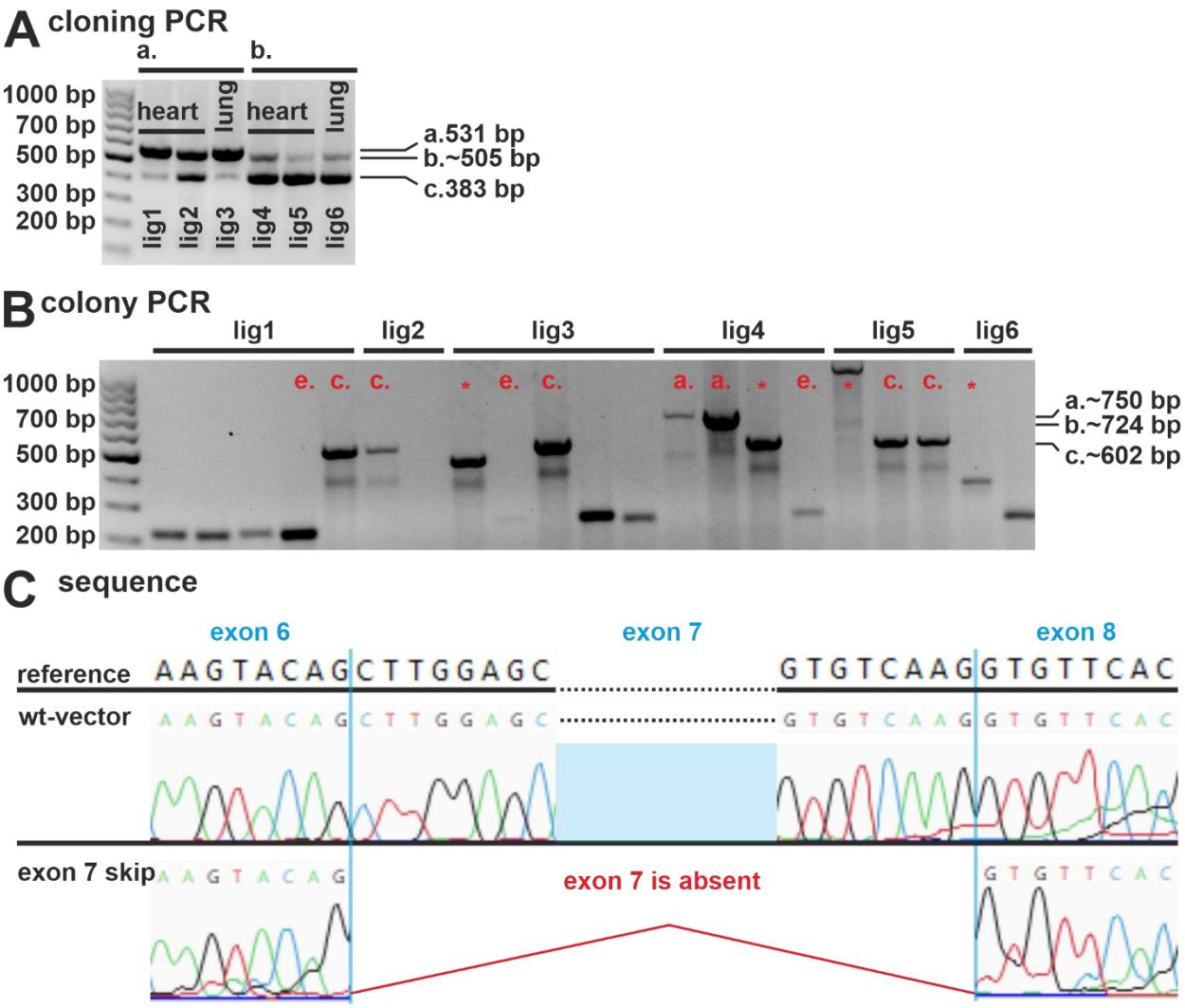

Figure 10. Failed attempt to isolate *Prdm16*^{csp1} splice isoforms by molecular cloning. A Cloning PCR of gel-isolated PCR products (compare Figure 9 A) for the *wild-type*- (a.) and *unknown* isoform (b.) generated bands at 531 bp (*wild-type*, a.), ~ 505 bp (*unknown* transcript, b), and 383 bp (*exon 7 skipping*, c.). lig - ligation. **B** Colony PCR of successfully transformed clones (ligation 1-6) produced bands with the expected lengths for the insertion of *wt* splice isoform (~ 750 bp, a.), *unknown* transcript (~ 724 bp, b.), *exon 7 skipping* isoform (~ 602 bp, c). Red letters indicate clones selected for Sanger sequencing and the result of the analysis: a. – *wild-type* splice isoform, c. – *exon 7 skipping* splice isoform, e – empty vector, * – nonsense sequence. **C** Example sequence for vectors expressing the *Prdm16 wt*- and the *exon 7 skip*-isoform in which exon 6 is followed by exon 8 instead of exon 7.

To finally detect differential splicing in *Prdm16*$^{csp1/wt}$ mice, a high-throughput sequencing approach was applied. For that, the nested PCR of the ~ 780 bp gel-isolated product (compare Figure 9 B) including the *wt*-, the *unknown*-, and the *exon 7 skip* band, was analysed with targeted next-generation sequencing (NGS). Reads accumulated at ~ 297 bp (*wt*), ~ 149 bp (*exon 7 skipping*), and ~ 270 bp (*unknown*). In-depth analysis of all reads showed the presence of the *Prdm16 wt* splice isoform and four differential *Prdm16*^{csp1} splice isoforms in *Prdm16*$^{csp1/wt}$ mice. Normal splicing of the

wt allele leads to correct alignment of all 17 exons of *Prdm16* (Figure 11 A). The resulting protein (1275 aa) contains the PR domain, the zinc finger domains, the proline rich domain, the repressor domain, and the C-terminal acidic activation domain (Figure 11 B). Two *Prdm16*^{csp1} splice isoforms derive from whole exon 7 skipping. Both isoforms use the splice acceptor site of exon 8. The *exon 7 skip 1* isoform uses the normal intronic splice donor site, and the *exon 7 skip 2* isoform uses a cryptic splice donor site in exon 6. In both *exon 7 skip* isoforms, deficient splicing leads to a frameshift and premature termination of Prdm16 (Figure 11 A - B). In another variant (*in-frame 1*), exon 6 and 7 are partially excluded (Figure 11 A). As this deletion is in-frame, there are 19 amino acids missing in the protein (Figure 11 B). The last variant (*in-frame 2*) results from use of a cryptic splice donor- and acceptor site in exon 6, is in-frame, and leads to a 19 aa shorter Prdm16 protein too (Figure 11 A - B). Interestingly, the cryptic splice donor sites in exon 6 are all located at different genomic positions (Table 20). However, it is not clear how the deletion of 19 aa affects Prdm16 three-dimensional structure and function, especially because the deletions locate to the first or second zinc finger in the C-terminal zinc finger domain, respectively.

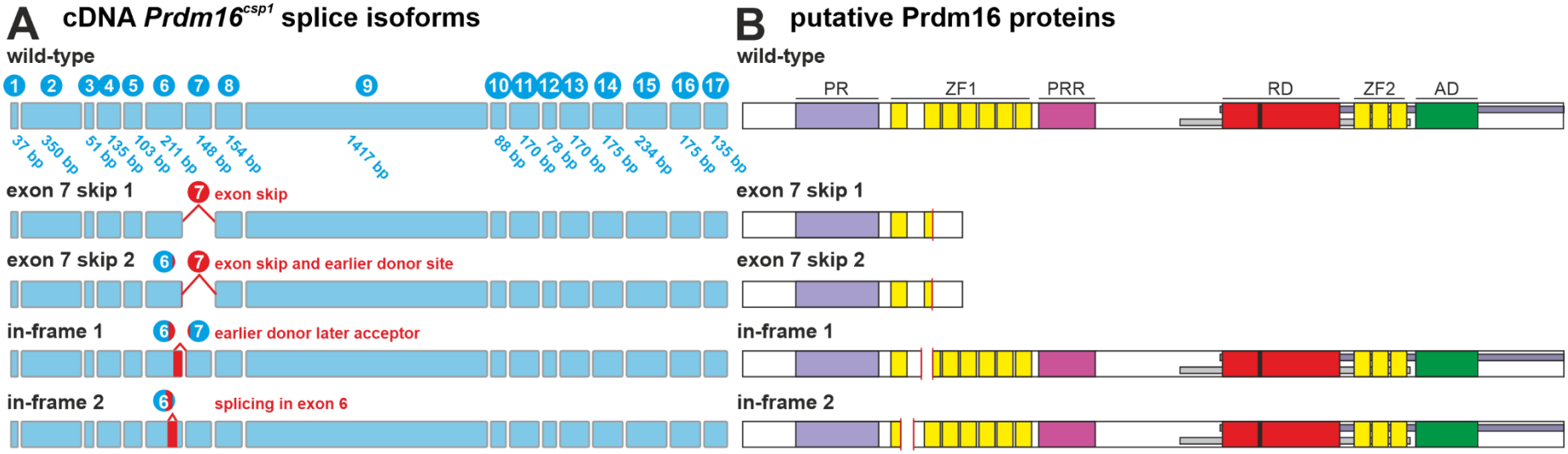

Figure 11. *Prdm16*^{csp1} splice isoforms. A The *wt Prdm16* comprises 17 exons. The *csp1* mutation leads to exclusion of exon 7 (*exon 7 skip 1*). In the *exon 7 skip 2* isoform, exon 7 is also absent, in addition to activation of a cryptic splice donor site in exon 6. In the *in-frame 1* isoform, the splice donor site is in exon 6 and the splice acceptor site is in exon 7. In the *in-frame 2* isoform, splicing occurs within exon 6. Exons are depicted in blue; the length is indicated below. Aberrant splicing is highlighted in red. **B** Putative Prdm16 proteins resulting from aberrant splicing. The wild-type Prdm16 has a length of 1275 aa. Both *exon 7 skip* isoforms lead to premature termination of Prdm16. In the in-frame variants, variable stretches of 19 aa are missing. The red line marks the start of the new aa sequence, or the deleted parts. Abbreviations: PR – PR domain; ZF1/2 – zinc finger domain 1/2; RD – repressor domain; AD – acidic activation domain.

Table 20. Description of Prdm16 proteins resulting from defective *csp1* splicing.

Splice isoform	Genomic positions of exon-exon junctions (Chromosome 4, reverse strand)	Transcript length [bp]	Description of putative protein
Wild-type	- Exon 6: 154,348,134 - 154,347,924 - Exon 7: 154,346,142 - 154,345,995 - Exon 8: 154,345,475 - 154,345,322	8598	- Wild-type Prdm16 - Domains: PR, ZF1/2, RD, AD - 1275 aa length
Exon 7 skip 1	- Exon 6: 154,348,134 - 154,347,924 - Exon 7: - - Exon 8: 154,345,475 - 154,345,322	8450	- Frameshift variant - Premature termination in second zinc finger (ZF1) - 342 aa length
Exon 7 skip 2	- Exon 6: 154,348,134 - 154,347,930 - Exon 7: - - Exon 8: 154,345,475 - 154,345,322	8444	- Frameshift variant - Premature termination in second zinc finger (ZF1) - 340 aa length
In-frame 1	- Exon 6: 154,348,134 - 154,347,976 - Exon 7: 154,346,137 - 154,345,995 - Exon 8: 154,345,475 - 154,345,322	8541	- In-frame deletion - 19 aa of second zinc finger (ZF1) missing - 1266 aa length
In-frame 2	- Exon 6: 154,348,134 - 154,348,011 - Exon 6: 154,347,953 - 154,347,924 - Exon 7: 154,346,142 - 154,345,995 - Exon 8: 154,345,475 - 154,345,322	8541	- In-frame deletion - 19 aa of first zinc finger (ZF1) missing - 1266 aa length

3.1.4 Altered *Prdm16* levels due to aberrant splicing in *Prdm16$^{csp1/wt}$* mice

In order to quantify *Prdm16* depletion caused by the *csp1* allele in heterozygous *Prdm16$^{csp1/wt}$* hearts, the expression of the different *Prdm16^{csp1}* splice isoforms was measured by qPCR. Glyceraldehyde-3-phosphatase dehydrogenase (*Gapdh*) and Progressive ankylosis protein (*Ank*) were used for normalisation with the ΔΔCt method. Primers were designed to amplify regions unaffected by defective splicing (exon 3-4; 14-15) as well as regions including splice affected exon 6 and 7 (exon 6-7; 7-8). Exon 6-7 primers amplified only the *wild-type* and the *in-frame 2* isoforms. Exon 7-8 primers amplified the *wild-type* and both *in-frame* isoforms. qPCR showed a significant reduction (~50 %) of excised regions (exon 6-7; 7-8) in *Prdm16$^{csp1/wt}$* mice (Figure 12 A + C). Interestingly, the expression of regions unaffected by defective *csp1* splicing (exon 3-4; 14-15) was increased in *Prdm16$^{csp1/wt}$* mice, suggesting an auto-regulatory feedback loop of *Prdm16.* However, we did not test if this occurs allele specifically. (Figure 12 B + D). Normalisation to both controls (*Gapdh* and *Ank*) produced similar results apart from significant changes of exon 14-15 and exon 7-8 in *Prdm16$^{csp1/wt}$* males if normalised to *Ank* (Figure 12 C + D), but not if normalised to *Gapdh*, which was likely due to technical reasons (Figure 12 A + B). Unfortunately, it was not possible to quantify the loss of Prdm16 protein in Western blot analysis. None of the commercially available antibodies specifically detected Prdm16 (data not shown). In addition, no suitable antibodies targeting different peptide sequences of the putative Prdm16^{csp1} mutant proteins existed. However, qPCR indicated that aberrant splicing caused by the *csp1* allele in heterozygous *Prdm16$^{csp1/wt}$* mice led to a significant reduction of *Prdm16* (~ 50 %) but no complete loss. Final proof and quantification of Prdm16 knockout in heterozygous *Prdm16$^{csp1/wt}$* animals requires an appropriate technique, e.g., quantitative mass spectroscopy.

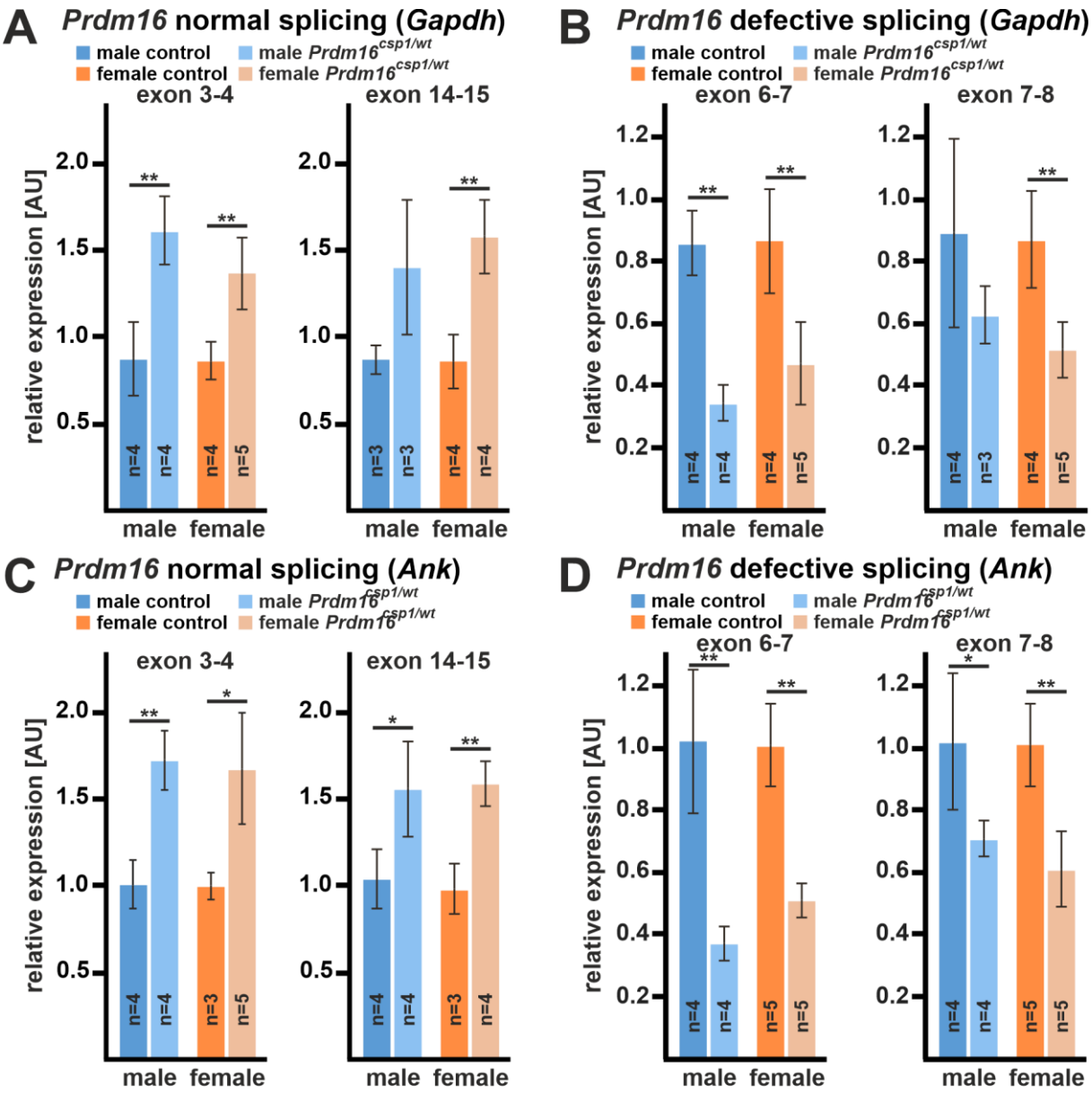

Figure 12. Quantification of defective splicing in *Prdm16*$^{csp1/wt}$ mice by qPCR. A In *Prdm16*$^{csp1/wt}$ hearts, regions of the *Prdm16* transcript unaffected by the csp1 mutation were upregulated. *Gapdh* was used as control gene. **B** *Prdm16* was reduced but not completely deleted due to defective splicing in *Prdm16*$^{csp1/wt}$ hearts. *Gapdh* was used for normalisation. **C** Similar observations after normalisation with *Ank* (compare A). **D** Similar observations after normalisation with Ank (compare B). Differences between genotypes were assessed by unpaired t-test. [*p≤0.05; **p≤0.01]. Values are illustrated as mean, error bars indicate standard deviation. Abbreviations: n – animal count; Gapdh – Glyceraldehyde-3-phosphatase dehydrogenase; Ank – Progressive ankylosis protein; AU – arbitrary units.

3.2 Physiological analysis of the *Prdm16*^{csp1} mouse strain

3.2.1 Reduced body and heart weights in *Prdm16*$^{csp1/wt}$ mice and altered body composition in females

The phenotype of heterozygous *Prdm16*$^{csp1/wt}$ and *Prdm16*$^{wt/wt}$ controls was evaluated at 8 months of age. All *Prdm16*$^{csp1/wt}$ animals were vital until sacrificed. *Prdm16*$^{csp1/wt}$

mice weighed significantly less than controls and their relative heart weight was reduced if normalised to the tibia length (Figure 13 A). Also, nuclear magnetic resonance (NMR) spectroscopy revealed altered body composition in female *Prdm16*$^{csp1/wt}$ mice. The body fat percentage was reduced, whereas muscle mass was increased. Interestingly, the body composition of male *Prdm16*$^{csp1/wt}$ mice was unchanged (Figure 13 B).

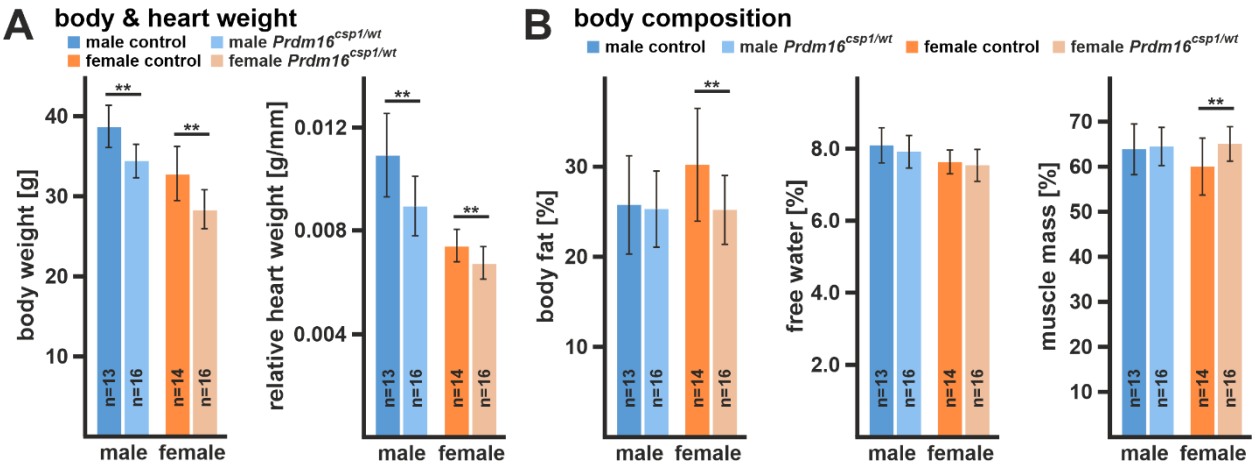

Figure 13. Body parameters of *Prdm16*$^{csp1/wt}$ animals. A *Prdm16*$^{csp1/wt}$ mice were lighter, also the heart weight-to-tibia ratio was reduced. **B** Female *Prdm16*$^{csp1/wt}$ mice had reduced body fat percentage and increased muscle mass. Differences between genotypes were assessed by unpaired t-test. [*p ≤ 0.05; **p ≤ 0.01]. Values are illustrated as mean, error bars indicate standard deviation. Abbreviations: n – animal count.

3.2.2 Sex pronounced reduction in cardiac function of *Prdm16*$^{csp1/wt}$ animals

Echocardiography realised a detailed analysis of cardiac structure and function of *Prdm16*$^{csp1/wt}$ mice and cotrols. Systolic function was evaluated by stroke volume (SV), ejection fraction (EF), and cardiac output (CO). Mitral flow profiles and diastolic annular velocities were used to measure the E/A and E/E' ratio for the assessment of diastolic function. *Prdm16*$^{csp1/wt}$ animals showed mild signs of impaired systolic heart function. SV and CO were diminished in both sexes, whereas EF was reduced only in females (Figure 14 A). Unaltered E/A and E/E' ratios indicated normal diastolic function (Figure 14 B).

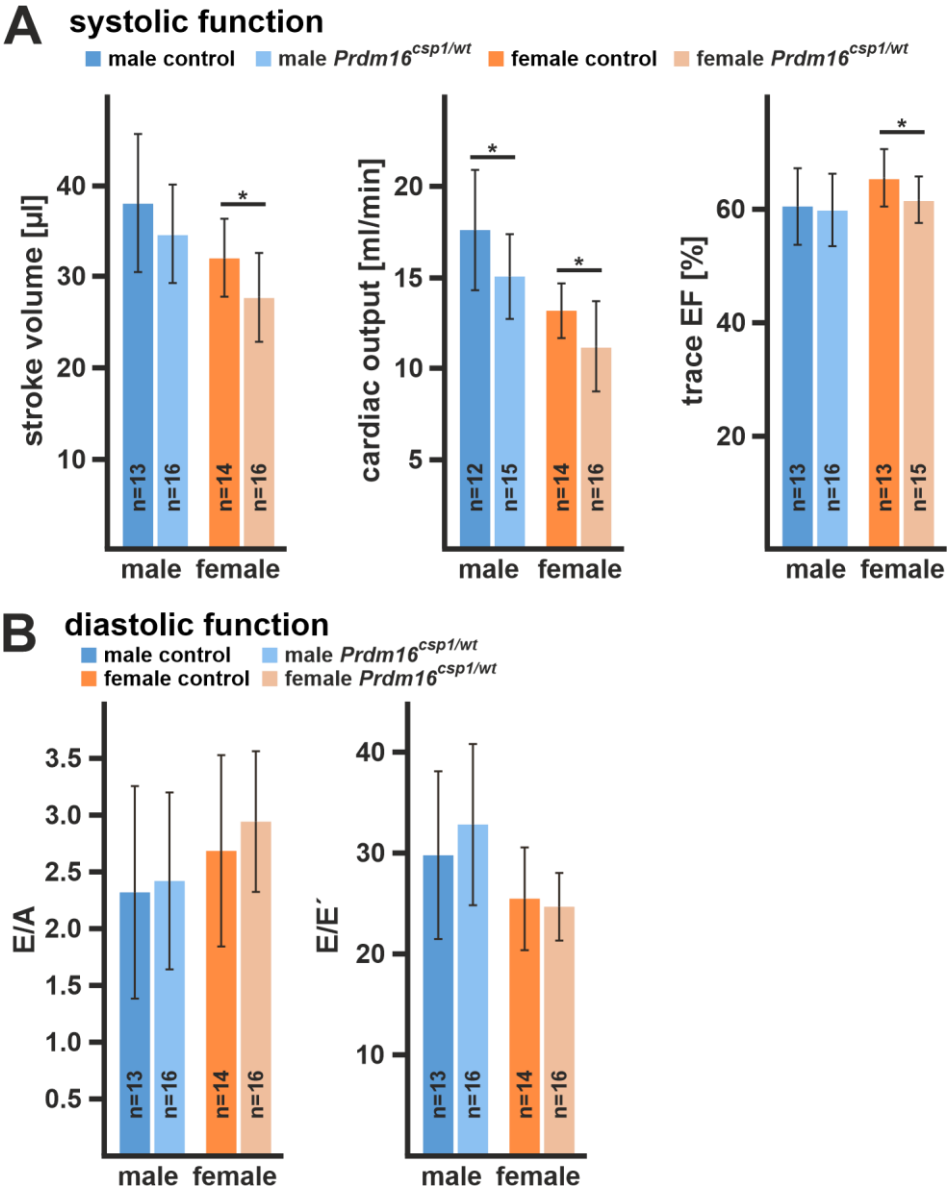

Figure 14. Cardiac function of *Prdm16*$^{csp1/wt}$ mice. A Systolic function was significantly reduced in *Prdm16*$^{csp1/wt}$ mice, with stronger expressiveness in females. **B** Unchanged E/A and E/E´ ratios indicated normal diastolic function of *Prdm16*$^{csp1/wt}$ hearts. Differences between genotypes were assessed by unpaired t-test. [*p ≤ 0.05; **p ≤ 0.01]. Values are illustrated as mean, error bars indicate standard deviation. Abbreviations: n – animal count; trace EF – left ventricle ejection fraction.

In echocardiography, chamber dimensions were measured as the left ventricular internal diameter at diastole and systole (LVIDd/s), and wall dimensions were measured as the thickness of the interventricular septum at diastole and systole (IVSd/s) and the left ventricular posterior wall (LVPWd/s). Chamber and wall dimensions remained largely unchanged, except for a minimal reduction of LVPWd and LVPWs in *Prdm16*$^{csp1/wt}$ females and a minimal increase of IVSs in *Prdm16*$^{csp1/wt}$ males (Figure 15).

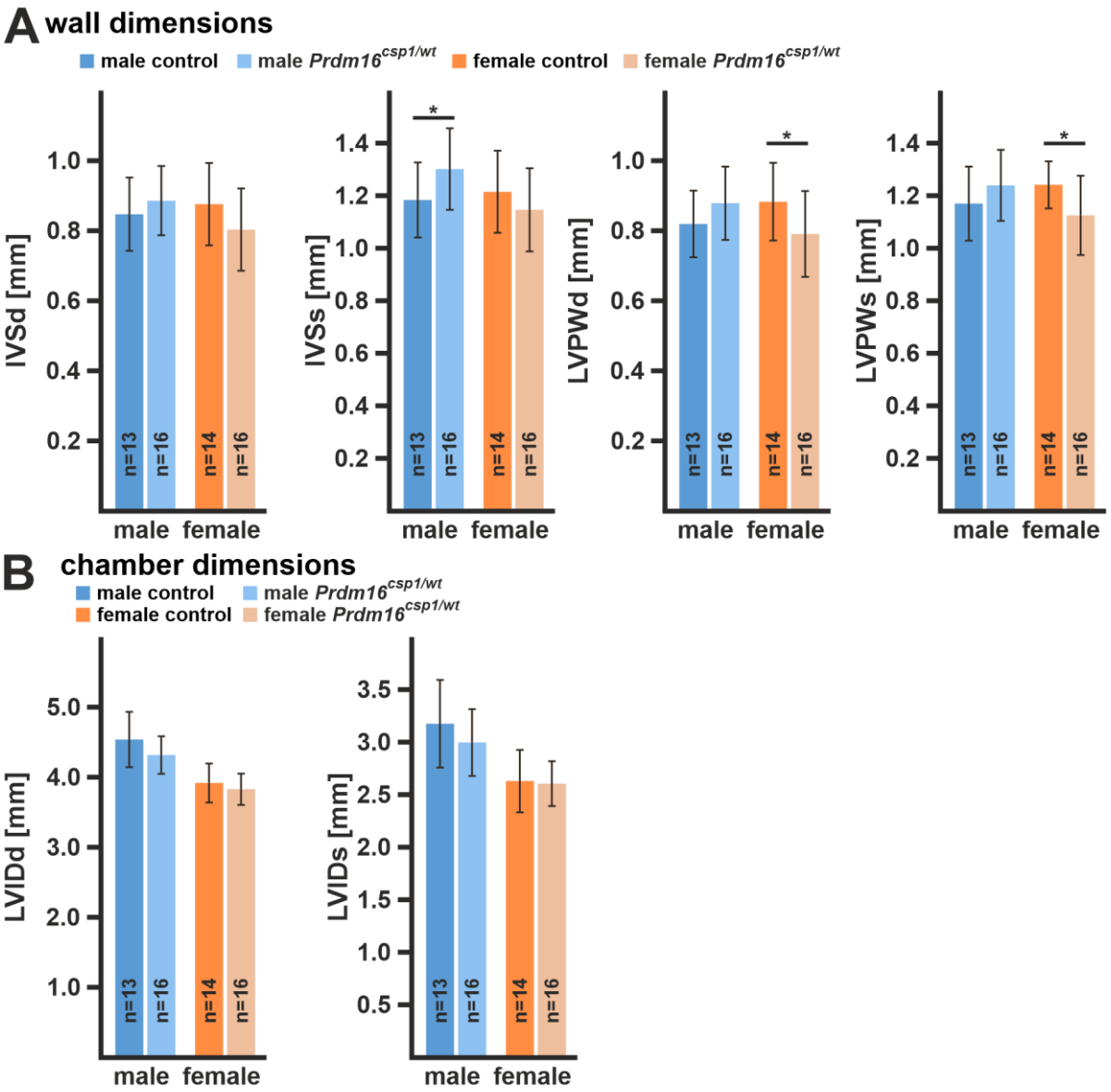

Figure 15. Cardiac dimensions of *Prdm16*$^{csp1/wt}$ mice. A Only minor changes in wall dimensions appeared in the hearts of *Prdm16*$^{csp1/wt}$ mice. **B** Chamber dimensions remained unaffected by heterozygous *Prdm16* deletion. Differences between genotypes were assessed by unpaired t-test. [*p ≤ 0.05; **p ≤ 0.01]. Values are illustrated as mean, error bars indicate standard deviation. Abbreviations: n – animal count; IVSd – interventricular septum at diastole; IVSs – interventricular septum at systole; LVPWd – left ventricular posterior wall at diastole; LVPWs – left ventricular posterior wall at systole; LVIDd – left ventricular internal diameter at diastole; LVIDs – left ventricular internal diameter at systole.

Additionally, electrocardiograms (ECGs) of *Prdm16*$^{csp1/wt}$ mice and controls were recorded. Also, non-invasive blood pressure measurement occurred. ECGs showed altered electrical activity in *Prdm16*$^{csp1/wt}$ hearts. Prolonged QRS- and shorter P intervals appeared in females only. QTc duration was increased in both sexes. The heart rate stayed unaffected by heterozygous *Prdm16* deletion (Figure 16).

Prdm16$^{csp1/wt}$_animals presented normotensive values for systolic-, diastolic-, and mean arterial blood pressure (Table 21).

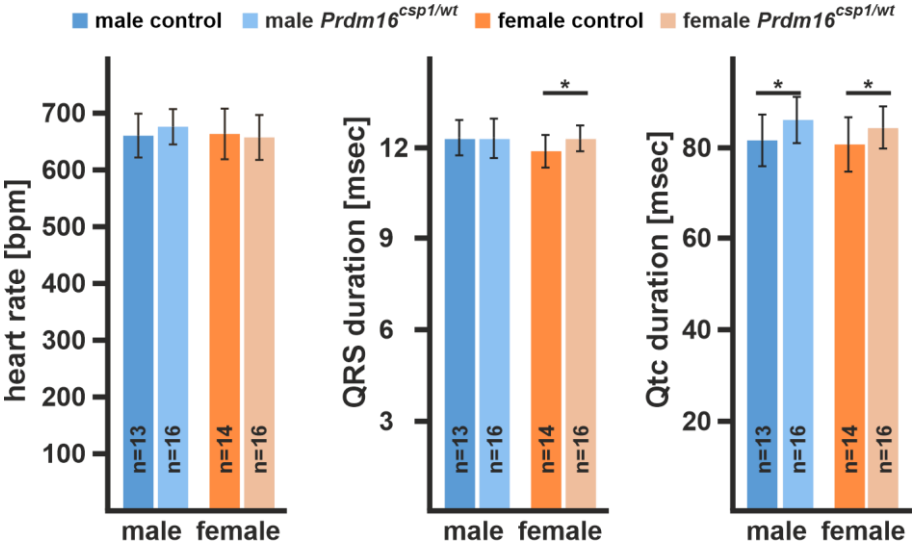

Figure 16. Electrocardiography in *Prdm16*$^{csp1/wt}$ mice. The heart rate of Prdm16$^{csp1/wt}$ mice was normal, whereas QRS and Qtc intervals were prolonged in *Prdm16*$^{csp1/wt}$ females and Qtc intervals were also prolonged in males. Differences between genotypes were assessed by unpaired t-test. [*p ≤ 0.05; **p ≤ 0.01]. Values are illustrated as mean, error bars indicate standard deviation. Abbreviations: n – animal count.

Table 21. Blood pressure.

		male - 8 months			female - 8 months		
value	**unit**	**controls**	***Prdm16*$^{csp1/wt}$**	**t-test**	**controls**	***Prdm16*$^{csp1/wt}$**	**t-test**
n		13	16		14	16	
HR	bpm	622.53 ± 36.30	613.89 ± 45.69	n.s.	613.19 ± 43.92	599.07 ± 33.41	n.s.
sBP	mmHg	131.94 ± 11.49	128.85 ± 13.53	n.s.	112.80 ± 11.93	116.59 ± 13.96	n.s.
dBP	mmHg	103.97 ± 10.07	99.73 ± 11.37	n.s.	88.03 ± 8.96	89.13 ± 14.46	n.s.
MAP	mmHg	112.96 ± 10.20	109.15 ± 11.78	n.s.	96.01 ± 9.84	97.98 ± 13.93	n.s.

All values are given as mean ± standard deviation. Differences between genotypes were considered statistically significant if $p \leq 0.05$ was calculated by unpaired t-test. Abbreviations: n – animal count; HR – heart rate; sBP – systolic blood pressure; dBP – diastolic blood pressure; MAP – mean arterial pressure; n.s. – not significant.

3.2.3 Normal respiratory function in *Prdm16$^{csp1/wt}$* mice

Respiratory function in *Prdm16$^{csp1/wt}$* mice and controls was evaluated with double chamber plethysmography by measurement of inspiratory time, expiratory time, relaxation time, peak inspiratory flow, expiratory flow, tidal volume, expired volume, minute volume, breathing frequency, end-inspiratory pause, end-expiratory pause, specific airway resistance, specific airway conductance, and mid-expiratory flow. Interestingly, the lung function of *Prdm16$^{csp1/wt}$* mice appeared normal in respiratory analysis. Apart from reduced tidal volume and expired volume in *Prdm16$^{csp1/wt}$* females, there were no differences between controls and *Prdm16$^{csp1/wt}$* mice (Table 22).

Table 22. Respiratory analysis.

		male - 8 months			female - 8 months		
value	**unit**	**controls**	***Prdm16*$^{csp1/wt}$**	**t-test**	**controls**	***Prdm16*$^{csp1/wt}$**	**t-test**
n		13	16		14	16	
Ti	msec	108.98 ± 15.30	104.96 ± 14.74	n.s.	118.12 ± 13.29	115.95 ± 13.05	n.s.
Te	msec	125.36 ± 12.06	124.22 ± 14.67	n.s.	126.9 ± 12.09	134.69 ± 22.60	n.s.
RT	msec	73.02 ± 7.47	75.02 ± 13.38	n.s.	77.76 ± 8.22	83.10 ± 16.68	n.s.
PIF	ml/sec	2.62 ± 0.50	2.73 ± 0.58	n.s.	2.54 ± 0.43	2.39 ± 0.49	n.s.
PEF	mg	2.69 ± 0.45	2.70 ± 0.61	n.s.	2.63 ± 0.50	2.30 ± 0.57	n.s.
TV	ml	0.20 ± 0.03	0.20 ± 0.04	n.s.	0.21 ± 0.03	0.19 ± 0.03	$p \leq 0.05$
EV	ml	0.20 ± 0.03	0.20 ± 0.04	n.s.	0.21 ± 0.03	0.19 ± 0.03	$p \leq 0.05$
MV	ml	54.47 ± 8.21	55.93 ± 10.21	n.s.	55.60 ± 9.14	49.03 ± 10.77	n.s
f	bpm	267.63 ± 28.55	276.35 ± 24.20	n.s.	260.72 ± 29.79	261.00 ± 33.76	n.s
EIP	msec	1.40 ± 0.43	1.60 ± 0.45	n.s.	1.80 ± 0.21	1.81 ± 0.34	n.s.
EEP	msec	16.23 ± 2.17	15.27 ± 2.14	n.s.	15.71 ± 1.59	16.71 ± 2.99	n.s.
dT	msec	2.74 ± 0.76	2.88 ± 0.94	n.s.	2.56 ± 0.50	2.41 ± 1.08	n.s.
sRaw	cmH2O*sec	2.66 ± 0.75	2.80 ± 0.92	n.s.	2.49 ± 0.48	2.76 ± 1.74	n.s.
sGaw	1/cmH2O*sec	0.43 ± 0.15	0.42 ± 0.17	n.s.	0.44 ± 0.09	0.57 ± 0.28	n.s.
EF50	ml/sec	2.24 ± 0.46	2.35 ± 0.56	n.s.	2.37 ± 0.44	2.07 ± 0.57	n.s.

All values are given as mean ± standard deviation. Differences between genotypes were considered statistically significant if $p \leq 0.05$ was calculated by unpaired t-test. Abbreviations: n – animal count; Ti – inspiratory time; Te – expiratory time; RT – relaxation time; PIF – peak inspiratory flow; PEF – peak expiratory flow; TV – tidal volume; EV – expired volume; MV – minute volume; f – breathing frequency; EIP – end-

inspiratory pause; EEP – end-expiratory pause; dT – time delay; sRaw – specific airway resistance; sGaw – specific airway conductance; EF50 – mid-expiratory flow; n.s. – not significant.

3.2.4 Elevated *Nppb* expression in *Prdm16*$^{csp1/wt}$ females

For further evaluation of the cardiac phenotype in *Prdm16*$^{csp1/wt}$ mice, we measured the expression of *Natriuretic peptide B* (*Nppb)* as a common biomarker for pathological cardiac stress in the heart tissue of *Prdm16*$^{csp1/wt}$ heterozygotes and controls by qPCR. Interestingly, *Nppb* expression was elevated in *Prdm16*$^{csp1/wt}$ females but not in *Prdm16*$^{csp1/wt}$ males. This confirmed that heterozygous *Prdm16* deletion results in mild cardiac stress, with a stronger impact in the female sex (Figure 17).

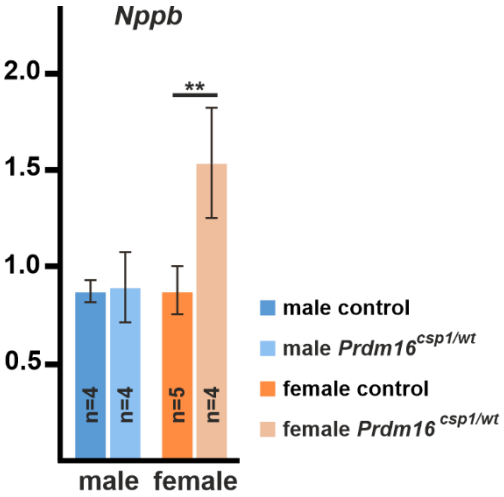

Figure 17. *Nppb* upregulation in female *Prdm16*$^{csp1/wt}$. A In *Prdm16*$^{csp1/wt}$ heart tissue, *Nppb* expression was increased in female mutants. Differences between genotypes were assessed by unpaired t-test. [*p ≤ 0.05; **p ≤ 0.01]. Values are illustrated as mean, error bars indicate standard deviation. Abbreviations: n – animal count; AU – arbitrary units, Nppb – Natriuretic peptide B.

3.3 Cardiac morphology of *Prdm16*$^{csp1/wt}$ mice

3.3.1 Normal cardiac tissue structure after heterozygous *Prdm16* deletion

Different histological procedures analysed the cardiac morphology in female *Prdm16*$^{csp1/wt}$ animals. H&E and Picro-Sirius red staining were used to screen for tissue organisation and extracellular collagen depositions, respectively. H&E staining revealed normal tissue structure (Figure 18 A). Picro-Sirius red staining showed the absence of fibrotic depositions in the hearts of mutant mice (Figure 18 B).

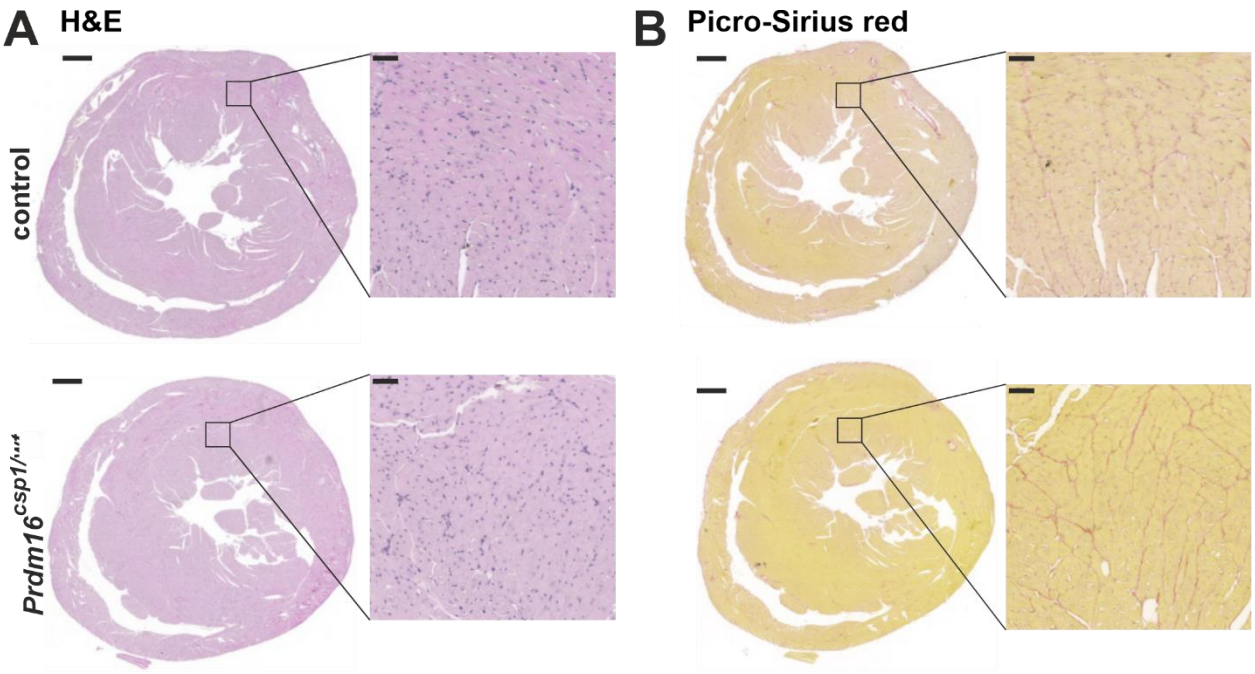

Figure 18. Normal tissue structure in histology of *Prdm16*$^{csp1/wt}$ hearts. A H&E staining of heart sections did not detect structural alterations in *Prdm16*$^{csp1/wt}$ mice. **B** Picro-Sirius red staining revealed the absence of fibrosis in *Prdm16*$^{csp1/wt}$ mice. Scale bars are 500 µm and 50 µm.

For a more sensitive detection of cardiac fibrosis sections, we performed immunostaining with antibodies targeting Collagen type I alpha 1 (Col1) and alpha smooth muscle actin (α-Sma), common markers for fibrosis or the presence of myofibroblasts, respectively. Confocal microscopy revealed negative staining for both markers and confirmed the absence of cardiac fibrosis in *Prdm16*$^{csp1/wt}$ mice (Figure 19).

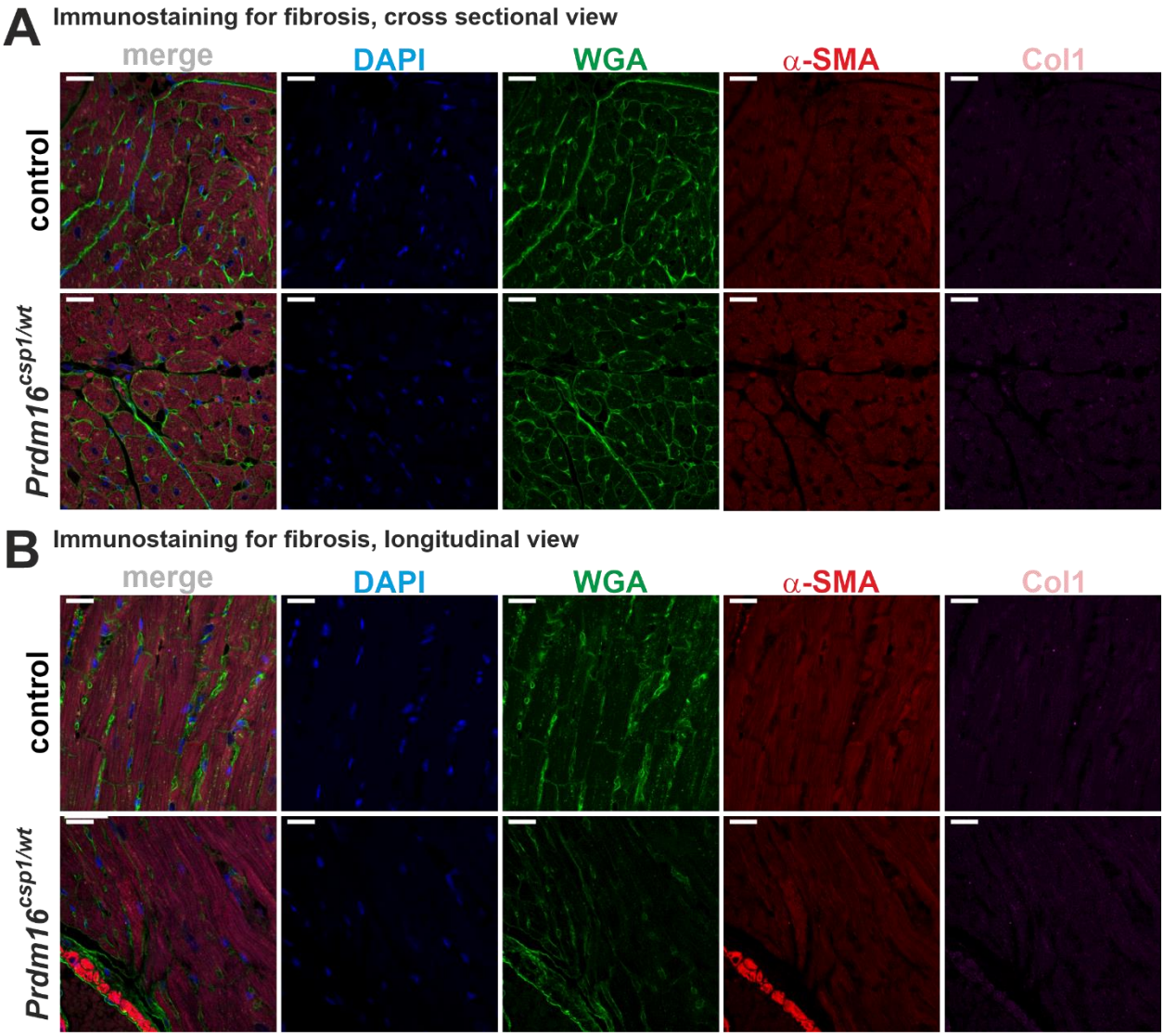

Figure 19. Absent cardiac fibrosis in immunostaining of *Prdm16*$^{csp1/wt}$ hearts. A Cross-sectional view of negative staining for fibrotic markers. **B** Longitudinal view of immunostained heart sections. Scale bar indicates 20 µm. Abbreviations: DAPI – 4′,6-diamidino-2-phenylindole; WGA – wheat germ agglutinin; α-Sma – alpha smooth muscle actin; Col1 – collagen type I alpha 1.

Several mutations in *PRDM16* are linked to LVNC (13). Hence, two heterozygous *Prdm16*$^{csp1/wt}$ mice were screened for left ventricular non-compaction and compared with two controls in H&E staining of serial heart sections. Normal compaction was displayed from a midventricular region to the apex in the left ventricles of *Prdm16*$^{csp1/wt}$ mice displayed normal (Figure 20).

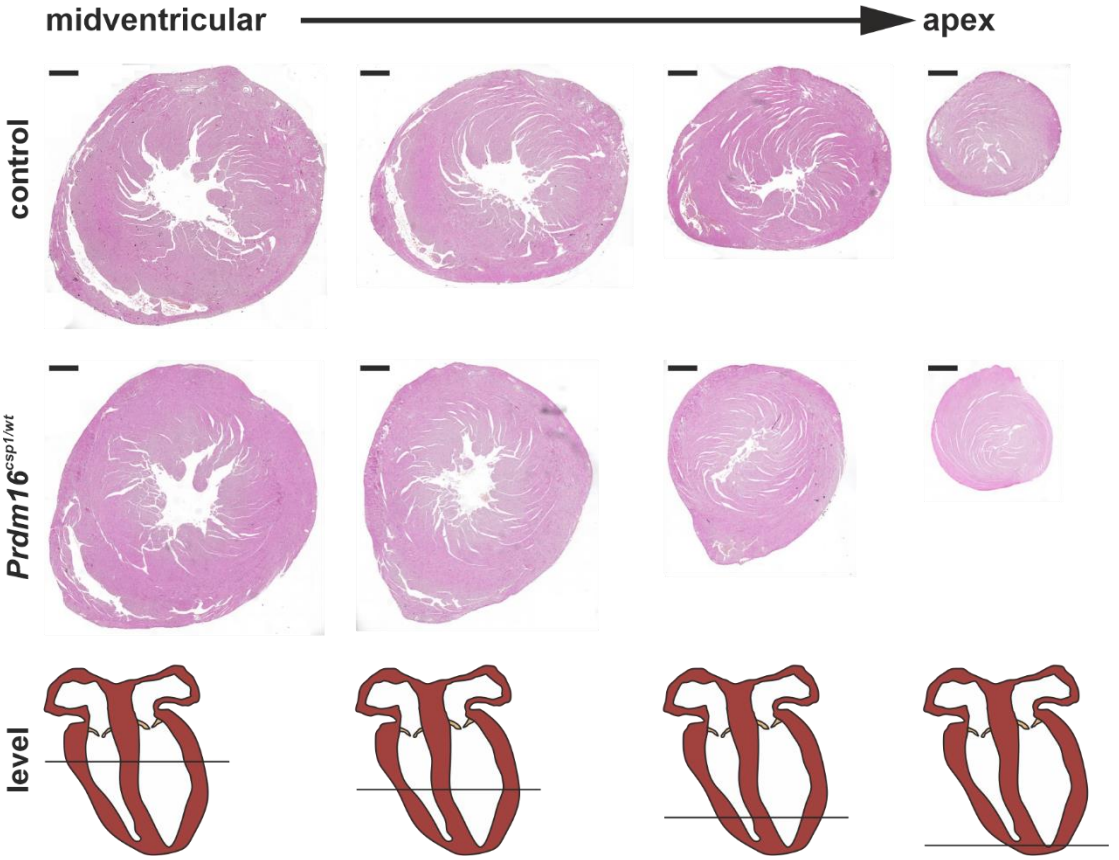

Figure 20. Compacted myocardium in serial sections of murine heart sections. H&E staining of serial heart sections revealed normal compaction of the left ventricle in *Prdm16*$^{csp1/wt}$ mice. The sectioning level is indicated in the last row. Scale bars are 500 µm.

3.3.2 Cardiomyocyte hypotrophy in *Prdm16*$^{csp1/wt}$ mice

Next, we questioned if the cardiac hypotrophy in *Prdm16*$^{csp1/wt}$ mice (compare 3.2.1) also occurs on the cellular level. Therefore, cell membranes of left ventricular cardiomyocytes were labelled with wheat germ agglutinin (WGA) to measure the cross-sectional areas in female mice. Concordant with the lower heart weights of *Prdm16*$^{csp1/wt}$ mice, the cardiomyocytes were reduced in size. This provided further evidence that heterozygous *Prdm16* deactivation leads to hypotrophy in the murine heart (Figure 21).

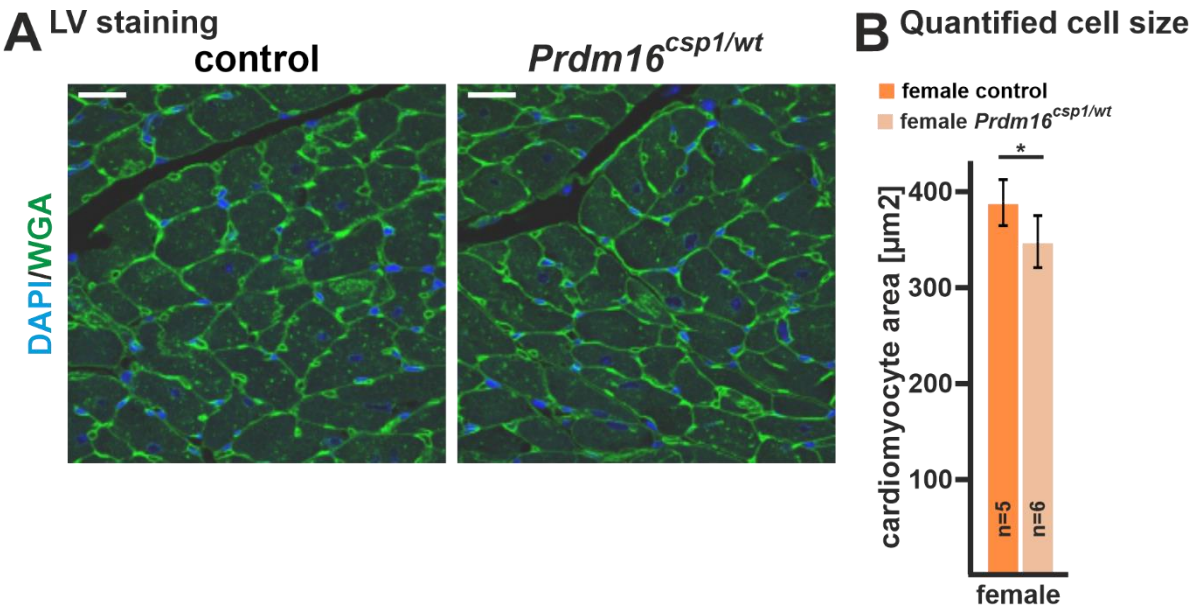

Figure 21. Hypotrophy of *Prdm16*$^{csp1/wt}$ cardiomyocytes. A Representative images of control and *Prdm16*$^{csp1/wt}$ left ventricles in cross-sectional view. DAPI stains the nuclei, WGA labels cell membranes. Scale bar shows 20 µm. **B** Quantification of cross-sectional areas identified hypotrophy of cardiomyocytes in *Prdm16*$^{csp1/wt}$ mice. Differences between genotypes were assessed by unpaired t-test [*p ≤ 0.05]. Values are illustrated as mean, error bars indicate standard deviation. Abbreviations: DAPI – 4′,6-diamidino-2-phenylindole; WGA – wheat germ agglutinin.

3.3.3 Normal myocardial ultrastructure in *Prdm16*$^{csp1/wt}$ mice

Myocardial ultrastructure of *Prdm16*$^{csp1/wt}$ females and controls was assessed by transmission electron microscopy (TEM) with the focus on mitochondrial size and number. Longitudinally orientated sections were used to count mitochondria, and to measure their independent area as well as the total mitochondrial area. Also, the sarcomere length and total sarcomere area were quantified. It needs to be noted that sarcomeres were fully contracted due to immersion fixation (Figure 22 A + B). The analysis revealed a minimal but significant reduction in sarcomere length of *Prdm16*$^{csp1/wt}$ hearts, in accordance with cardiac hypotrophy (Figure 22 B). Mitochondrial size and number, total mitochondrial area, and the ratio between sarcomere and mitochondrial area were unchanged (Figure 22 B). Unfortunately, the poor quality of sections prevented deeper analysis of mitochondrial ultrastructure. Generally, myocardial ultrastructure remained largely unaffected by heterozygous *Prdm16* inactivation.

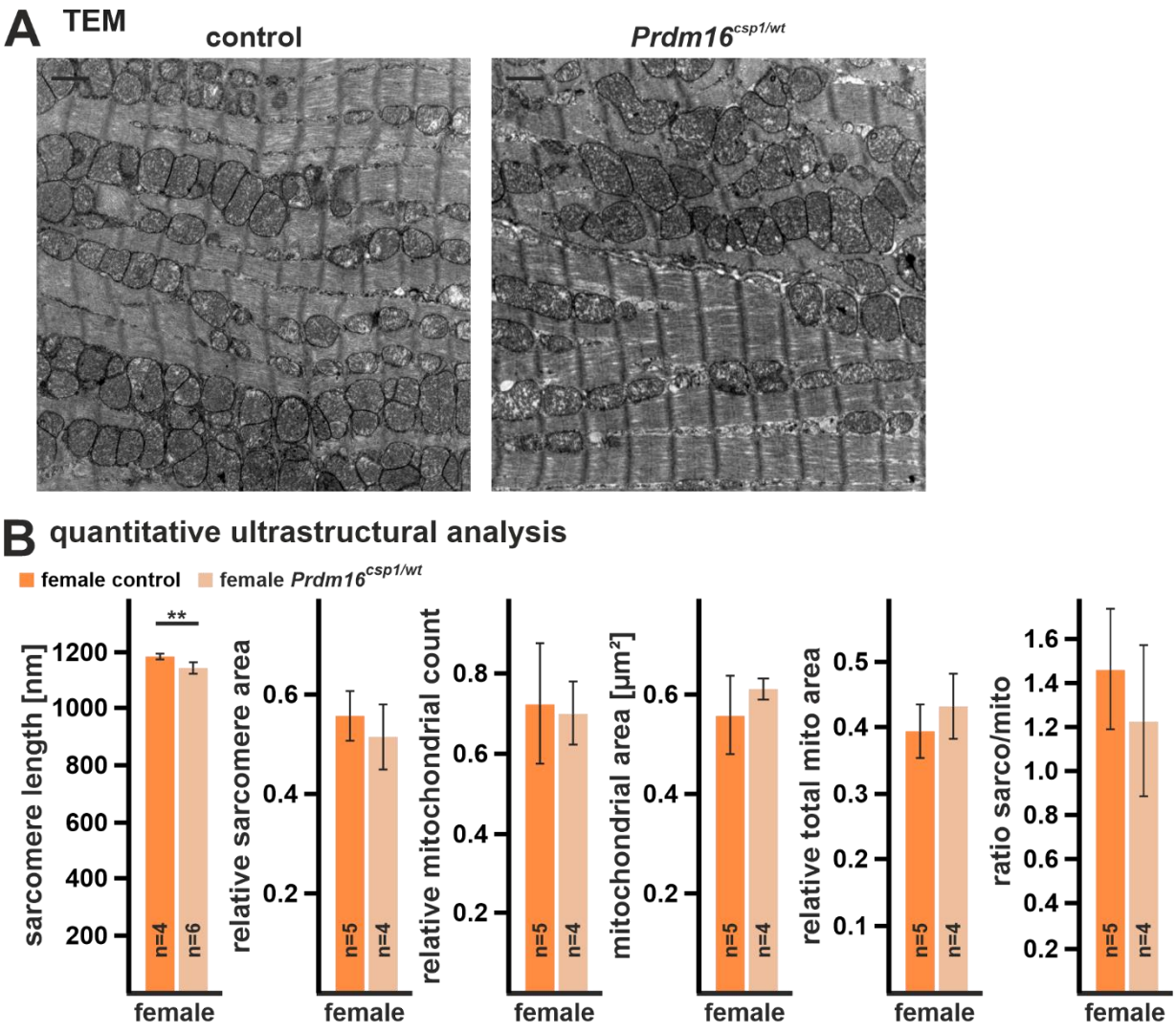

Figure 22. Ultrastructural evaluation of *Prdm16*$^{csp1/wt}$ left ventricles. **A** Representative transmission electron micrographs of controls and *Prdm16*$^{csp1/wt}$ mice. Scale bar shows 1000 nm. **B** Except for slightly shorter sarcomeres myocardial ultrastructure was normal in *Prdm16*$^{csp1/wt}$ mice. Sarcomere area, mitochondrial count, and total mitochondrial area were normalised to the defined ROI. Differences between genotypes were assessed by unpaired t-test. [*p ≤ 0.05; **p ≤ 0.01]. Values are illustrated as mean, error bars indicate standard deviation.

3.4 The molecular *Prdm16*$^{csp1/wt}$ phenotype

3.4.1 Consistent expression of sarcomere genes in *Prdm16*$^{csp1/wt}$ mice and controls

Mutation of the sarcomere can cause CMP and HF. Moreover, altered sarcomere function, structure, and gene expression appear frequently in CMP. Thus, we quantified mRNA expression of selected sarcomere genes in cardiac tissue of *Prdm16*$^{csp1/wt}$ mice and controls by qPCR. The analysis covered all relevant sarcomere regions. Thin filament: *alpha cardiac muscle actin 1* (*Actc1*), *cardiac muscle troponin*

T (*Tnnt2*); thick filament: *myosin heavy chain 6* (*Myh6*), *myosin heavy chain 7* (*Myh7*), *myosin light chain 3* (*Myl3*); z-disc: *alpha-actinin 2* (*Actn2*), *telethonin* (*Tcap*); *titin (Ttn); tropomyosin alpha-1 chain* (*Tpm1*); desmosomes: *desmoplakin* (*Dsp*). In general, qPCR demonstrated similar expression patterns between *Prdm16*$^{csp1/wt}$ animals and controls, with a few minor changes. In male *Prdm16*$^{csp1/wt}$ animals, *Actc1* and *Dsp* expression were slightly increased, and *Myl3* and *Tpm1* expression were slightly decreased. Only *Tcap* expression was notably elevated in both sexes (Figure 23). With the function of a stretch sensor, Tcap is involved in sarcomere assembly, t-tubule organisation, calcium homeostasis, apoptosis, and the pathogenesis of CMP (64-66). In summary, qPCR suggested normal composition of the sarcomere in *Prdm16*$^{csp1/wt}$ mice.

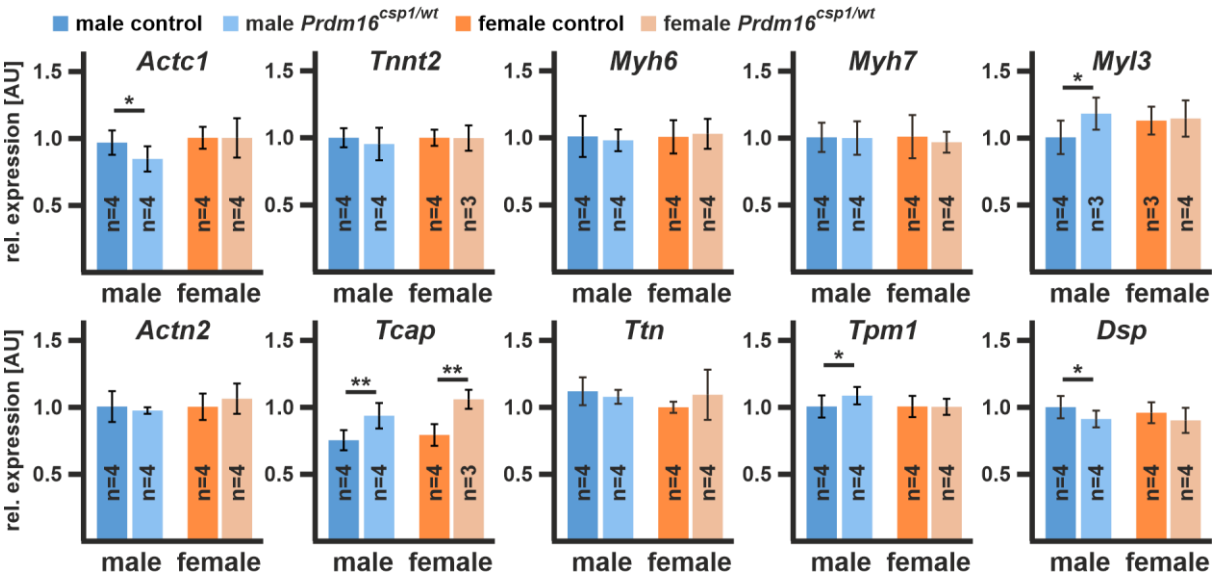

Figure 23. Regular expression of sarcomere genes in *Prdm16*$^{csp1/wt}$ hearts. qPCR showed that heterozygous *Prdm16* inactivation had no major impact on sarcomere gene expression. Expression of targets was normalised to *Gapdh*. Differences between genotypes were assessed by unpaired t-test. [*p ≤ 0.05; **p ≤ 0.01]. Values are illustrated as mean, error bars indicate standard deviation. Abbreviations: n – animal count; AU – arbitrary units; genes are abbreviated according to the Entrez Gene database of the National Center for Biotechnology Information (NCBI).

3.4.2 Unaffected global gene expression in the heart after heterozygous *Prdm16* deletion

Next, we questioned how heterozygous *Prdm16* inactivation affects global gene expression in *Prdm16*$^{csp1/wt}$ mice. Therefore, RNA isolated from interventricular septum

of 8-month-old *Prdm16*$^{csp1/wt}$ mice and controls was analysed in RNA sequencing. Interestingly, only a few genes were differentially expressed in *Prdm16*$^{csp1/wt}$ animals (LFC < -0.5 or > 0.5; normalised counts ≥ 50, p ≤ 0.01 in two-tailed t-test). In *Prdm16*$^{csp1/wt}$ males, 12 genes were upregulated and 16 genes were downregulated (Figure 24 A). In *Prdm16*$^{csp1/wt}$ females, 55 genes were upregulated and 35 genes were downregulated (Figure 24 C). Curiously, regulated genes showed little overlap between male and female *Prdm16*$^{csp1/wt}$ mice. Moreover, the analysis did not reveal the altered expression of known *Prdm16* target genes, genes encoding Prdm16 interaction partners, or the main CMP disease genes. As observed in qPCR (see 3.1.4), *Prdm16* was strongly upregulated in male and female *Prdm16*$^{csp1/wt}$ mice. It should be mentioned that - according to Uniprot (15) - some top-regulated genes are associated with transcriptional regulation (*Prdm16, Per1, Pbxip1, Rorb, Mycn, Nr1d1, Runx3, Junb, Rorc*) or metabolism (*Ubiad1, Adh1, Pyroxd2, Aldh3a1, Nr1d1, Scd4, Nmrk2, Lcat, Dhtkd1, Rorc, Aldob*) (Figure 24 B + D). However, RNA sequencing did not unveil outstanding targets for the explanation of the *PRDM16* CMP. Seemingly, neither altered gene expression nor the well-studied mechanisms of Prdm16 function are the main cause for the *Prdm16*$^{csp1/wt}$ cardiac phenotype.

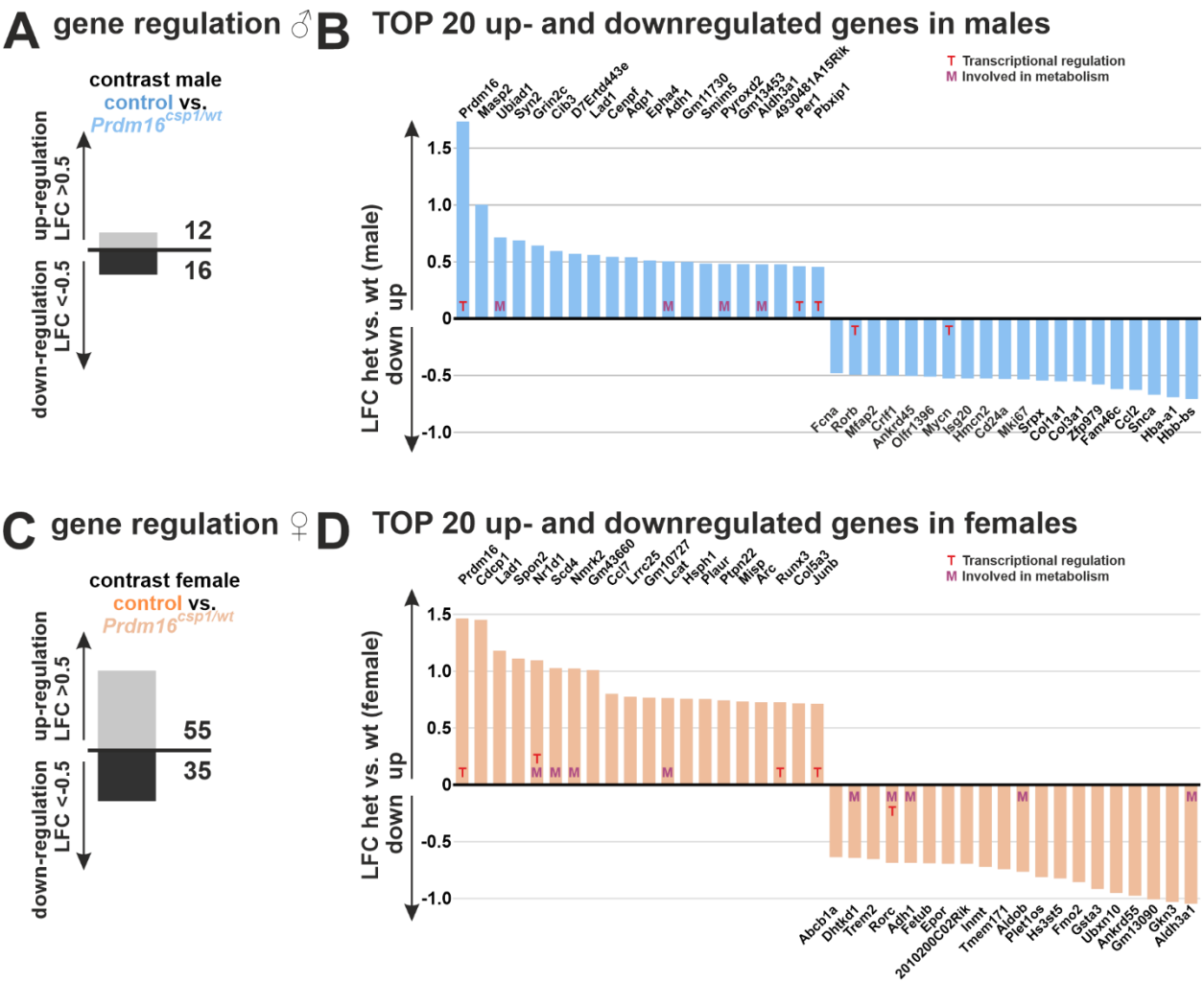

Figure 24. RNA sequencing of *Prdm16*$^{csp1/wt}$ cardiac tissue. A Only a small number of genes were differentially expressed in *Prdm16*$^{csp1/wt}$ males. **B** Regulated genes in *Prdm16*$^{csp1/wt}$ males are not known as targets of *Prdm16*, nor as main CMP disease genes. Some of the regulated genes are linked to transcriptional regulation and metabolism. **C** In female *Prdm16*$^{csp1/wt}$ mice a few more genes showed altered expression. **D** In the main, other genes were affected in female *Prdm16*$^{csp1/wt}$ mice. However, some are also linked to transcription or metabolism, but are not known *Prdm16* targets, or key players of CMP pathogenesis. Differential expression was defined for genes with at least 50 normalised counts, LFC < -0.5 or > 0.5, and $p \leq 0.01$ in two-tailed t-test. Abbreviations: LFC – log2 fold change; T – gene is associated with transcriptional regulation, M – gene with metabolic function.

3.4.3 Systematic reduction of central carbon metabolites in the *Prdm16*$^{csp1/wt}$ heart

Prdm16 is linked to mitochondrial and metabolic function, especially cell respiration (see 1.3.4). To study the metabolic pattern of heterozygous *Prdm16* inactivation, heart tissue of 8-month-old *Prdm16*$^{csp1/wt}$ mice and controls was analysed by Gas chromatography-mass spectrometry (GC-MS). The analysis covered the central carbon metabolism including glycolysis, the tricarboxylic acid cycle (TCA), the pentose

phosphate pathway (PPP), amino acids, glycerol, nucleobases, and miscellaneous metabolites. Strikingly, the central carbon metabolism was generally reduced in the *Prdm16*$^{csp1/wt}$ myocardium. Significant depletion of phosphoenol-pyruvic-acid, pyruvic acid, and glutaric acid appeared sex-independently in *Prdm16*$^{csp1/wt}$ mutants. Additionally, many of the other metabolites showed a tendency towards downregulation without reaching statistical significance (leucine, lysine, methionine, phenylalanine, threonine, glycerol-3-phosphate, ribose-5-phosphate, glyceric-acid-3-phosphate, lactic acid, citric acid, succinic acid, uracil, and glyceric acid). Interestingly, separate analysis of each sex condition confirmed the sex-bias of the *Prdm16*$^{csp1/wt}$ phenotype. In *Prdm16*$^{csp1/wt}$ males, only succinic acid was significantly reduced, whereas in *Prdm16*$^{csp1/wt}$ females, glycerol-3-phosphate, ribose-5-phosphate, phosphoenol-pyruvic acid, succinic acid, butanoic acid, and glutaric acid were significantly reduced. Also, almost every measured metabolite showed a tendency towards downregulation in female *Prdm16*$^{csp1/wt}$ mice (Figure 25). In univariate scaled analysis, metabolites of glycolysis, TCA, glycerol, and amino acids were assessed in groups. The values for each metabolite were transformed (see 2.2.7) and defined as upregulated if < 0 or downregulated if > 0. We compared the number of up- and downregulated metabolites between genotypes for each pathway and sex condition. Sex-independent analysis showed more downregulated metabolites in every group for *Prdm16*$^{csp1/wt}$ heterozygotes in comparison with controls. In male *Prdm16*$^{csp1/wt}$ mice, this applied only for amino acids and in female *Prdm16*$^{csp1/wt}$ mice only for TCA metabolites. Taken together, heterozygous deletion of *Prdm16* resulted in the systematic reduction of central carbon metabolites (Figure 25). These observations are compatible with either lower metabolic activity producing lower metabolite levels or higher metabolite turnover with increased uptake.

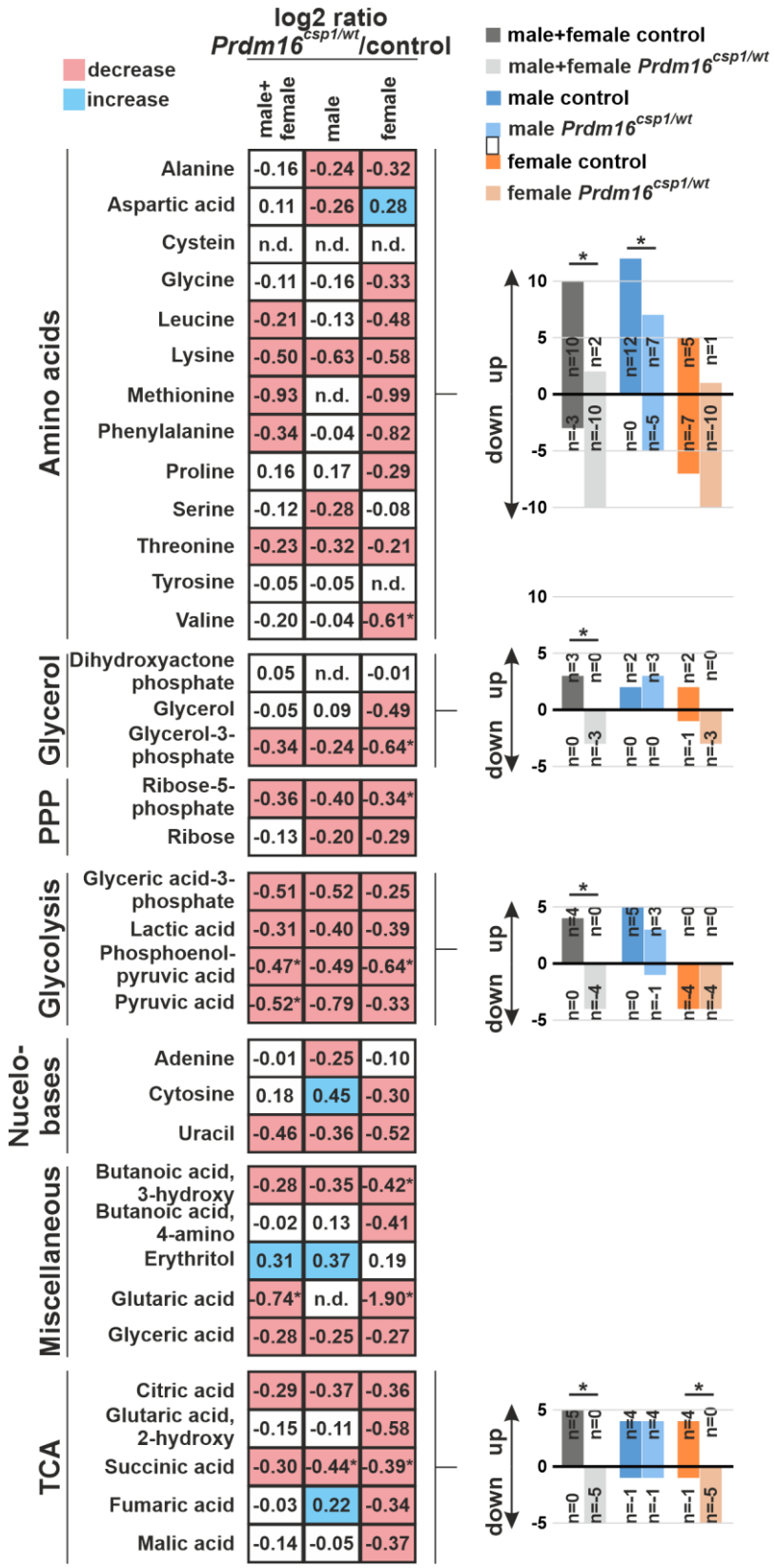

Figure 25. Altered cardiac metabolism in *Prdm16*$^{csp1/wt}$ mutants. On the left: GC-MS evaluation of central carbon metabolites showed a systemic decrease in *Prdm16*$^{csp1/wt}$ hearts that was more pronounced in females. Values are shown as $\log_2$ ratios between genotypes for different sex conditions and marked red for reduction ($\log_2$ ratio < 0.2) or blue for increase ($\log_2$ ratio > 0.2). On the right: Univariate scaled analysis indicated a reduction in amino acid, glycerol, glycolysis, and TCA metabolism of the *Prdm16*$^{csp1/wt}$ heart. If sexes were evaluated

separately, the amino acids were downregulated in male *Prdm16*$^{csp1/wt}$ mice only and TCA was downregulated in *Prdm16*$^{csp1/wt}$ females only. For single metabolites, differences between genotypes were assessed by unpaired t-test, and for univariate scaled analysis the Pearson`s chi-squared test was used [*p≤0.05]. Abbreviations: n.d. – not detected; PPP – pentose phosphate pathway; TCA – tricarboxylic acid cycle.

3.4.4 Impaired electron transport chain in the female *Prdm16*$^{csp1/wt}$ heart

The systematic reduction of the central carbon metabolism in *Prdm16*$^{csp1/wt}$ mice led to the hypothesis that PRDM16 is critical for cardiac energy metabolism. Therefore, we measured the protein expression of mitochondrial electron transport chain (ETC) complexes in heart lysates of *Prdm16*$^{csp1/wt}$ mice and controls in Western blot analysis. Antibodies targeted NADH dehydrogenase [ubiquinone] 1 beta subcomplex subunit 8 (Ndufb8) for complex I; succinate dehydrogenase complex, subunit A and B (Sdha/Sdhb) for complex II; cytochrome b-c1 complex subunit 2 (Uqrc2) for complex III; mitochondrially encoded cytochrome c oxidase I (Mtco1) and cytochrome c oxidase subunit 4 (Cox4) for complex IV; and ATP synthase F1 subunit alpha (Atp5a) for complex V. Furthermore, the analysis included mitochondrial import receptor subunit TOM20 (Tom20) and Heat shock protein 70 (Hsp70) (Figure 26 A). Remarkably, changes appeared specific to sex. On the one hand, male *Prdm16*$^{csp1/wt}$ mice showed unaltered expression of targeted proteins. On the other hand, female *Prdm16*$^{csp1/wt}$ mice showed lower normalised signal intensities for both complex IV markers, i.e., Mtco1 and Cox4. Moreover, a tendency towards downregulation of complex I and complex III appeared in female *Prdm16*$^{csp1/wt}$ mice, but did not reach statistical significance (Figure 26 B). Apparently, heterozygous *Prdm16* inactivation severely affected cellular respiration. The sex-bias of the *Prdm16*$^{csp1/wt}$ cardiac phenotype was clearly visible.

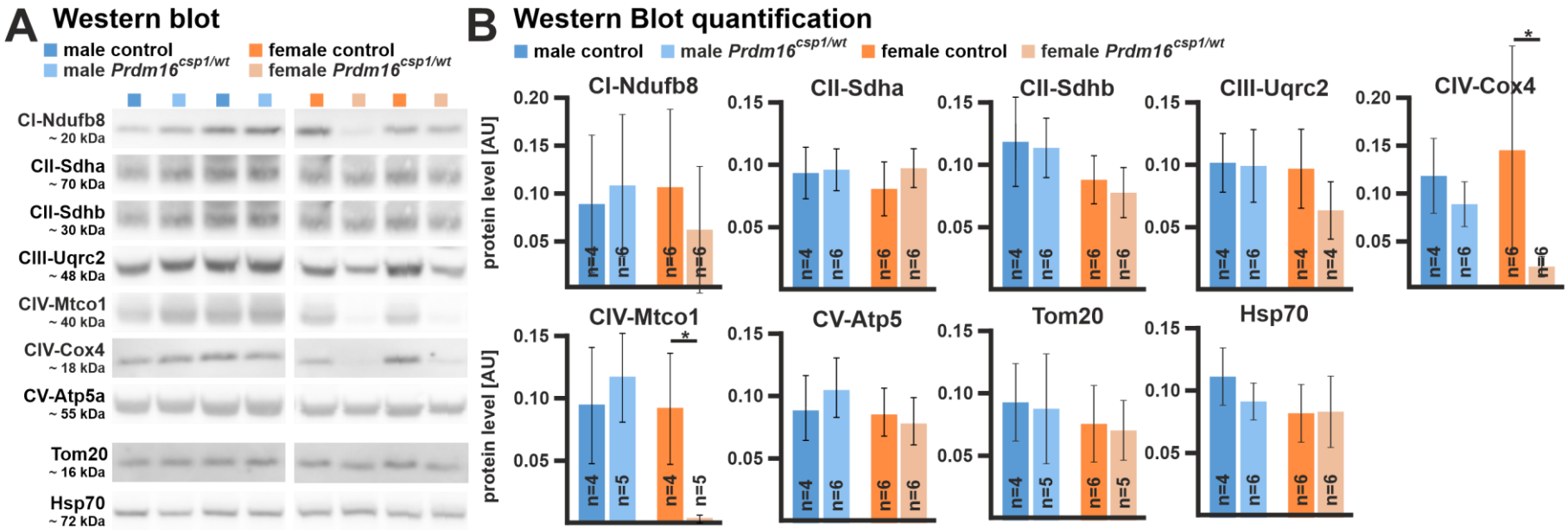

Figure 26. Alteration of the ETC in *Prdm16*$^{csp1/wt}$ hearts. A Western blot for the evaluation of protein expression of ETC components, Tom20 and Hsp70 in *Prdm16*$^{csp1/wt}$ heart tissue. **B** Quantification of signal intensities did not reveal significant changes in the hearts of male *Prdm16*$^{csp1/wt}$ mice. In female *Prdm16*$^{csp1/wt}$ hearts, complex IV was diminished. Complex I and III showed a tendency towards reduction without reaching statistical significance. Differences between genotypes were assessed by unpaired t-test. [*p ≤ 0.05]. Values are illustrated as mean, error bars indicate standard deviation. Abbreviations: n – animal count; AU – arbitrary units; Ndufb8 – NADH dehydrogenase [ubiquinone] 1 beta subcomplex subunit 8; Sdha – succinate dehydrogenase complex, subunit A; Sdhb – succinate dehydrogenase complex, subunit B; Uqrc2 – cytochrome b-c1 complex subunit 2; Mtco1 – mitochondrially encoded cytochrome c oxidase I; Cox4 – cytochrome c oxidase subunit 4; Atp5a – ATP synthase F1 subunit alpha; Tom20 – mitochondrial import receptor subunit TOM20; Hsp70 – Heat shock protein 70.

4 Discussion

4.1 Summary

This work investigated the role of *PRDM16* in the pathophysiology of CMP. It used the established *Prdm16*$^{csp1/wt}$ mouse model and was the first analysis of the mammalian cardiac phenotype after systemic heterozygous *Prdm16* deletion.

Targeted NGS and qPCR analysis revealed that the *csp1* mutation (c.888-3C>A) caused aberrant splicing and reduced expression of *Prdm16* in *Prdm16*$^{csp1/wt}$ hearts (Figure 27).

Prdm16$^{csp1/wt}$ mice expressed a mild CMP phenotype with a stronger impact in females. The *Prdm16*$^{csp1/wt}$ heart presented hypotrophy with impaired cardiac function as indicated by reduced CO, EF, and SV. Histological and ultrastructural analysis showed normal cardiac tissue structure and the absence of fibrosis in *Prdm16*$^{csp1/wt}$ mice. The body weight of *Prdm16*$^{csp1/wt}$ heterozygotes was decreased and *Prdm16*$^{csp1/wt}$ females were leaner compared to controls (Figure 27).

Regarding the molecular *Prdm16*$^{csp1/wt}$ phenotype, qPCR and RNA sequencing indicated that sarcomere and global gene expression were unaffected by heterozygous *Prdm16* deletion (Figure 27). Impressively, GC-MS analysis of *Prdm16*$^{csp1/wt}$ hearts uncovered a systematic decrease in central carbon metabolites as a surrogate for either deficiency or increased flux in myocardial metabolism. Again, the female sex was affected more severely. In addition, complex IV of the ETC was diminished in *Prdm16*$^{csp1/wt}$ females, but not in males, in Western blot analysis of cardiac tissue (Figure 27).

Altogether, this work introduced the existing *Prdm16*$^{csp1/wt}$ mouse strain as a model for the *PRDM16* associated CMP. Metabolic dysfunction is likely to be involved in the development of the disease. Furthermore, female sex is likely a determinant of the *PRDM16* CMP.

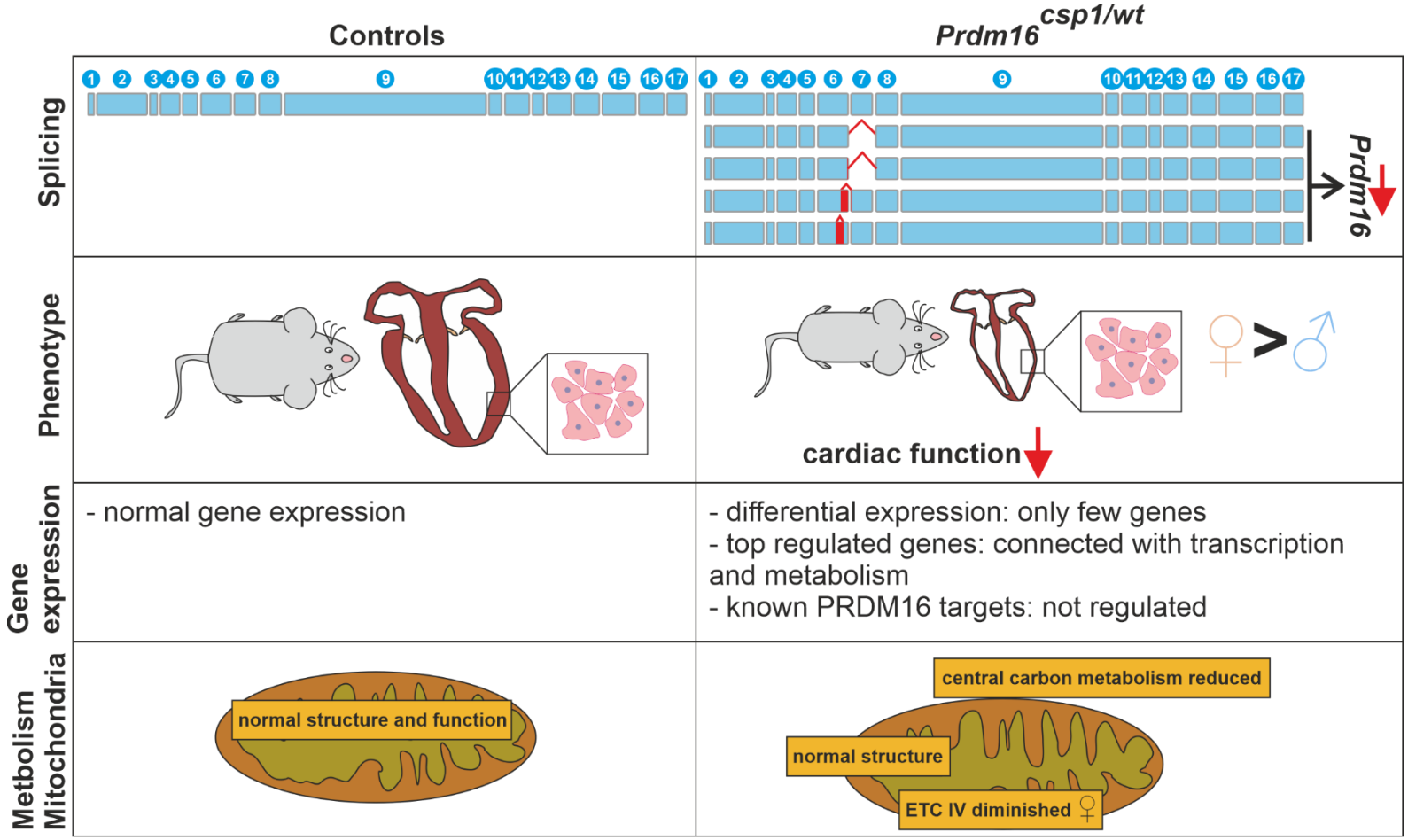

Figure 27. Main findings. In *Prdm16*$^{csp1/wt}$ heterozygotes, aberrant splicing led to four alternative splice isoforms and the reduction of functional *Prdm16*. In comparison to controls, *Prdm16*$^{csp1/wt}$ mice showed lower body weights and cardiac hypotrophy. The histological structure was preserved in *Prdm16*$^{csp/wt1}$ hearts, and cardiac function was mildly reduced. The phenotype was more prominent in females. Only a few genes were differentially expressed in *Prdm16*$^{csp/wt1}$ hearts. Interestingly, most of the regulated genes are associated with transcription or metabolism. Known targets of PRDM16 remained unchanged. Heterozygous *Prdm16* inactivation altered the central carbon metabolism and ETC composition in cardiac mitochondria but the ultrastructure was normal. Central carbon metabolites were generally reduced. ETC complex IV was reduced in females. Abbreviations: ETC – electron transport chain.

4.2 Defective *csp1* splicing in cardiac tissue

Prdm16$^{csp1/wt}$ mice carry the *csp1* mutation of the intronic splice acceptor site of *Prdm16* (c.888-3C>A). Splicing mutations require proper experimental evaluation including characterisation of alternative transcripts and splicing efficiency. Precise measurement of lost and remaining functional transcript and protein is important, especially in heterozygous models considering potential compensation by the healthy allele.

The first attempts to evaluate *Prdm16*^{csp1} splicing in cardiac tissue of heterozygous *Prdm16*$^{csp1/wt}$ mice by direct sequencing of cDNA and molecular cloning failed. Similar lengths of splice isoforms avoided adequate separation, e.g., in gel electrophoresis. Targeted NGS revealed that the *csp1* mutation leads to cryptic splicing of *Prdm16*. Three defective splice isoforms lacked variable parts of exon 6 and 7. Putative Prdm16^{csp1} proteins are either truncated or missing small stretches. qPCR indicated a significant reduction (~50%) of functional *Prdm16* in heterozygous *Prdm16*$^{csp1/wt}$ mice. Unfortunately, the use of a heterozygous model, the complexity of *csp1* splicing, and the unavailability of functional anti-Prdm16 antibodies prevented quantification of Prdm16 deletion in *Prdm16*$^{csp1/wt}$ mutants by standard lab methods (Sanger sequencing, qPCR, Western blot analysis). Reduced *Prdm16* mRNA is only a surrogate for reduced Prdm16 protein. Furthermore, the qPCR primer design could not detect all splice isoforms. The *in-frame 2* isoform was still amplified. However, this probably caused only a minor disturbance because the proportion of this isoform in *csp1* splicing was likely to have been minimal. Also, the experimental approach with gel separation and nested PCR prior to NGS analysis avoided the quantification of the *Prdm16* transcripts by NGS.

When Bjork et al. (30) established the FVB.C-Prdm16^{csp1}/J strain, they identified only the *exon 7 skip 1* isoform in *Prdm16*$^{csp1/csp1}$ homozygotes. This discrepancy was likely to have been caused by the different experimental approach. They observed two distinct bands for *Prdm16*$^{csp1/csp1}$ homozygotes in gel electrophoresis of cDNA generated from total RNA. Their lengths were similar compared to the *wt* splice isoform and the two *exon 7 skip* isoforms, respectively (Figure 28 A). Direct sequencing detected the *exon 7 skip 1* isoform. The band also probably contained the *exon 7 skip 2* isoform, but to such a low extent that it appeared as background noise in Sanger sequencing. In contrast, highly sensitive NGS analysis detected the *exon 7 skip 2*

isoform. Bjork et al. (30) described the longer band present in *Prdm16*$^{csp1/csp1}$ homozygotes as the *wt* splice isoform. From their manuscript, it is not clear whether their claim was based on sequencing or relied on the length only. Actually, the band might have contained the two in-frame isoforms, which are only minimally shorter. Moreover, Bjork et al. (30) detected signals for Prdm16 in Western blot analysis of *Prdm16*$^{csp1/csp1}$ mice and controls, but not in gene-trap null-mutated animals (Figure 28 B). Therefore, they described a hypomorphic character of the *csp1* allele. However, it might have been that their anti-Prdm16 antibody did not recognise Prdm16 correctly. The signals were observed after long exposure and multiple bands with an unexpected length for Prdm16 appeared, which was explained by posttranslational modifications (Figure 28 B). With that being said, it is not clear if the *csp1* allele is truly hypomorphic. Because we did not test for *Prdm16* allele-specific expression in *Prdm16*$^{csp1/wt}$ heterozygotes and could not detect Prdm16 protein, we could neither clearly confirm nor falsify this. Furthermore, the possibility of tissue-specific effects remains. We analysed splicing in cardiac tissue, whilst Bjork et al. used brain buds.

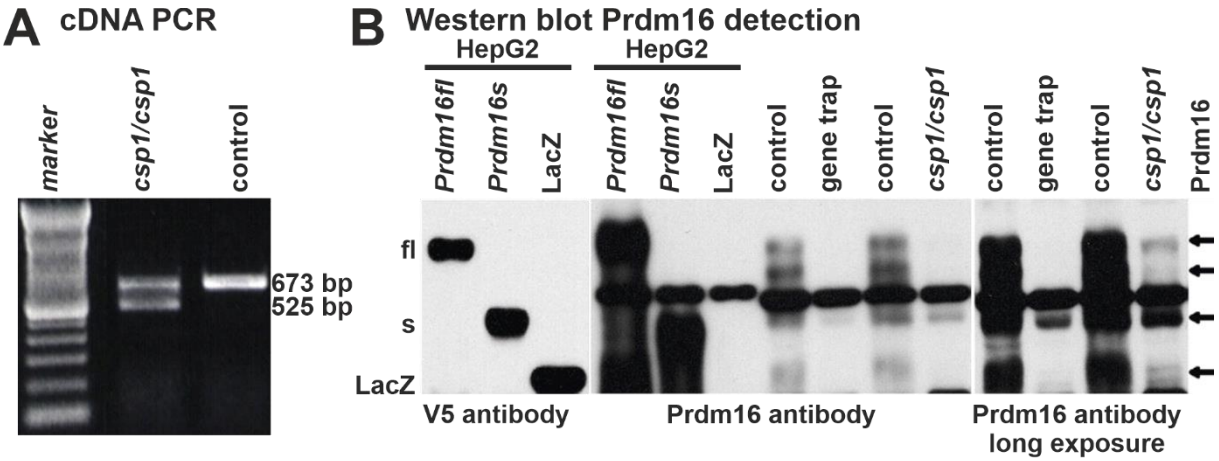

Figure 28. Analysis of the *csp1* mutation. A Amplification of cDNA revealed the presence of two bands in *Prdm16*$^{csp1/csp1}$ mice. They were assigned to the *wild-type* splice isoform (673 bp), and *exon 7 skip 1* splice isoform (525bp) **B** On the left: detection of V5-tagged PRDM16fl, Prdm16s, and LacZ control in transfected HepG2 cells with an anti-V5 antibody. On the right: detection of PRDM16 with an antibody targeting the mid region in the same cell lysates. Black arrows on the right indicate signals observed in control mice, but not in mutants, most likely corresponding to Prdm16. The Prdm16 bands with unexpected molecular weights were explained by posttranslational modifications. Signals for Prdm16 after long exposure in *Prdm16*$^{csp1/csp1}$, but not in gene trap animals, suggested a hypomorphic character of the *csp1* mutation. The antibody produced severe background staining with multiple unspecific bands (modified from Bjork et al. (30), DOI: 10.1093/hmg/ddp543, agreement of Oxford University Press).

4.3 Phenotype of systemic heterozygous *Prdm16* deletion

The phenotype of *Prdm16*$^{csp1/wt}$ mice was analysed with a focus on cardiac function (ECG, echocardiography, blood pressure) and included basic analysis of body composition and respiratory function. Furthermore, different histological procedures evaluated cardiac morphology and ultrastructure.

We found that heterozygous *Prdm16*$^{csp1/wt}$ mice were vital, whereas homozygous *Prdm16*$^{csp1/csp1}$ animals died shortly after birth due to lung- and/or heart failure (30). *Prdm16*$^{csp1/wt}$ mutants presented an early-stage CMP phenotype: mildly reduced cardiac function, hypotrophy of the heart and individual cardiomyocytes, normal cardiac morphology and ultrastructure without fibrosis. This resembled previous findings: the homozygous *Prdm16*$^{csp1/csp1}$ heart appeared hypotrophic, clefted at the ventricular apex, and well-structured in histology (30) A clefted apex also appeared in homozygous *Prdm16* cKO mice in addition to several other cardiac anomalies like LVNC (57). The phenotypes of homozygous *Prdm16* cKO differed among each other and from the *Prdm16*$^{csp1/wt}$ phenotype. In adult *Prdm16* cKO mice, cardiac dysfunction progressed further and was accompanied by hypertrophy and fibrosis (48, 56). In one *Prdm16* cKO model, there was a structural heart defect, and cardiac dysfunction was so severe that mice died 7 days after birth (57). It can be suspected that initially *Prdm16* deletion causes heart hypotrophy. Then, cardiac malfunction is aggravated, and pathological hypertrophy and cardiac fibrosis emerge eventually. Moreover, possible systemic effects due to the germline character of the *csp1* mutation must be considered. Conditional knockouts rely on the Cre-*loxP* system. Two *locus of crossover P1* (*loxP*) sites are introduced to flank a critical region of the target gene and serve as recognition sites for excision by the recombinase Cre. A cell-specific driver of Cre expression allows targeted KO in selected tissues. (67, 68). Cibi et al. (56) used a *Mesp1* Cre-driver, Nam et al. (48) used a *Myh6* Cre-driver, and Wu et al. (57) used a *Xmlc2* and *cTnt* Cre-driver. This led to *Prdm16* cKO in the cardiovascular system or in cardiomyocytes, respectively (48, 56, 57, 68). KO efficiency can depend on the Cre driver and result in different phenotypes as seen in the different *Prdm16* cKO strains (48, 56, 57). The choice of a cKO model is advantageous for understanding the cell-specific functions of a target gene, but easily it neglects that the heart is composed of different cell types that communicate together or that systemic influences can impact disease onset and progression (68, 69). This is particularly applicable for the *PRDM16* CMP. For example, PRDM16 acts as a master regulator of brown and beige adipose

tissue formation and function (20-22, 32, 33). With obesity as a main risk factor of cardiovascular disease, adipose tissue and the heart are tightly connected (70). Adipose tissue acts as the main lipid storage and an endocrine organ. This makes it critical for systemic energy homeostasis which impacts cardiac function. Also, secreted hormones directly act in cardiac tissue (71). Conversely, the heart controls adipose tissue function and systemic energy homeostasis mainly via the natriuretic peptide system (72). Epicardial adipose tissue might be of special interest. It was shown to exhibit beige features. Lower expression of thermogenic genes in epicardial adipose tissue like *PRDM16* and *UCP1* was associated with reduced ejection fraction and atrial fibrillation (73-75). Another potential cause of the phenotype discrepancy between *Prdm16*$^{csp1/wt}$ mice and *Prdm16* cKOs lies within the use of different mouse strains. Studies have shown that the genetic background of a mouse model severely affects the progression of cardiac hypertrophy and heart failure (76-78). ECG alterations in *Prdm16*$^{csp1/wt}$ and *Prdm16*-cKO mice were similar. The heart rate was normal, and Qtc- and QRS intervals were prolonged (48).

Respiratory function in heterozygous *Prdm16*$^{csp1/wt}$ mice appeared to be principally normal. In any case, the simple assessment only included the main parameters of lung function. *Prdm16* is expressed in lung tissue during embryonic development and the lungs of *Prdm16*$^{csp1/csp1}$ homozygotes showed hypoplasia and histological abnormalities (30, 31). However, Prdm16 function in lung tissue has not been studied intensively to date. A lung phenotype in *Prdm16*$^{csp1/wt}$ heterozygotes is possible and might appear at a later time point or in detailed evaluation of *Prdm16*$^{csp1/wt}$ lungs, e.g., by histological- and expression analysis. Furthermore, it is possible that the progression of cardiac dysfunction can lead to secondary affection of the respiratory system in *Prdm16*$^{csp1/wt}$ mice. Pulmonary hypertension, lung congestion, ventilation-perfusion mismatch, and impaired gas-exchange are well-known complications of HF (79-81).

Unexpectedly, systemic heterozygous deletion of *Prdm16* led to lower body weight in both sexes and a reduced body fat percentage in female *Prdm16*$^{csp1/wt}$ mice. Actually, one might have expected obese *Prdm16*$^{csp1/wt}$ mice because Prdm16 is necessary for the function and development of brown and beige adipose tissue (20-22, 32, 33), which is generally believed to protect from obesity (82). Furthermore, adipocyte-specific *Prdm16* KO mice were more susceptible for diet-induced obesity (33), whilst mice with transgenic expression of *Prdm16* in adipose tissue were protected (34). However, body

weight regulation underlies a complex interaction of multiple tissues. Amongst others, natriuretic peptides are associated with increased lipolysis, weight loss, and reduced body fat (72). *Nppb* was elevated in *Prdm16*$^{csp1/wt}$ females, but in *Prdm16* cKO mice with severe cardiac dysfunction and *Nppb* elevation the body weight was normal (48, 56). Presumably, there is another reason for the altered body composition in *Prdm16*$^{csp1/wt}$ mice, e.g., neurohormonal changes or altered food intake due to the loss of *Prdm16* in the brain.

4.4 Role of transcriptional regulation in the *PRDM16* CMP

Altered sarcomere function and mutations or differential expression of sarcomere genes appear in CMP and HF (3, 7, 8). Consequently, we tested for altered expression of selected sarcomere genes in qPCR and observed a high similarity between *Prdm16*$^{csp1/wt}$ mice and controls. Furthermore, we investigated if gene expression was generally disarrayed in *Prdm16*$^{csp1/wt}$ heart tissue by RNA sequencing. The analysis revealed that global gene expression in murine hearts was largely unaffected by systemic heterozygous *Prdm16* knockout. Less than 100 genes were expressed differentially between *Prdm16*$^{csp1/wt}$ and controls. In contrast, the transcriptome was severely altered in all homozygous *Prdm16* cKO models (48, 56, 57). Here, more than 700 or even more than 1,000 genes were expressed differentially in mutant animals. Upregulated genes were associated with hypertrophy (including sarcomere genes), heart failure, oxidative stress, fibrosis, cell death, cardiac ion homeostasis (e.g., calcium), or transmembrane potential and transport. Downregulated genes were associated with cardiac metabolism, heart development, and iron homeostasis (48, 56, 57). As for the phenotype (see 4.3), this discrepancy can be explained by different disease stages. In the far progressed CMP phenotypes of the homozygous *Prdm16* cKO mice, it is hard to define if changes are primary, caused by *Prdm16* deletion, or if they are secondary. Notably, Cibi et al. (56) and Wu et al. (57) observed disarrayed gene expression prior to onset of the phenotype. Prdm16 directly bound to the promotor of hypertrophic genes and interacted with Ehmt1 to repress these genes (56). This interaction has been described in adipose tissue before (25, 32). Interestingly, findings after the pharmacological inhibition and activation of EHMT1/2 *in vivo* and *in vitro* suggest that EHMT1 protects against cardiac hypertrophy (83). Wu et al. (57) found that *Prdm16* determined the cell fate of cardiomyocytes in synergy with other cardiac transcription factors (e.g., *Tbx5, Hand1*) by inducing compact myocardial

genes and repressing trabecular ones. Other known interaction partners of PRDM16 like PPAR-α/γ or PGC-1α/β, (20, 21, 27, 35), are also linked to cardiac health and disease by regulating cardiac energy metabolism and mitochondrial biogenesis (84-90). However, in RNA sequencing of *Prdm16*$^{csp1/wt}$ hearts, none of these were altered. The same was true for transcripts related to *Tgf-β* signalling. On the contrary, *Tgf-β* was activated in *Prdm16* cKO mice, as evidenced by elevated transcripts of the *Tgf-β* pathway (e.g., *Tgfb2*) or an increased p-Smad2/Smad2 ratio (48, 56, 57). Again, it is important to ask what primarily caused the *Tgf-β* upregulation: *Prdm16* deletion or general cardiac dysfunction? In iPSC-CM, PRDM16 negatively regulated TGF-β (51). Arndt et al. (13) proposed a functional connection between *PRDM16* and the *SKI* ortholog in the zebrafish heart. Additionally, numerous studies in non-cardiac tissues provided evidence that PRDM16 influences the TGF-β pathway (24, 26, 47, 49, 50).

4.5 Is the *PRDM16* CMP a metabolic CMP?

As PRDM16 is linked to mitochondrial and metabolic function (compare 1.3.4), we screened *Prdm16*$^{csp1/wt}$ cardiac tissue for alterations in mitochondrial content as well ascentral carbon metabolism, and performed Western blot analysis of the ETC.

Brief analysis of cardiac ultrastructure did not detect any major alterations in mitochondrial content or integrity in the *Prdm16*$^{csp1/wt}$ heart. In adult *Prdm16* cKO - but not in neonates - cardiac mitochondria were degenerated (56). In adipose tissue, deletion of *Prdm16* led to degenerated mitochondria and *PRDM16* expression stimulated mitochondrial biogenesis (21, 32).

Strikingly, *Prdm16*$^{csp1/wt}$ mice showed severe disturbance of the cardiac metabolism. A general reduction of the central carbon metabolism, as measured by GC-MS, suggested metabolic deprivation or increased turnover in *Prdm16*$^{csp1/wt}$ hearts. Previous studies showed reduced expression of metabolic and mitochondrial pathway genes (e.g. fatty acid oxidation, ETC) as well as increased expression of glucose metabolism genes in *Prdm16* cKO hearts (56, 57). Similar findings exist in adipose tissue and the small intestine (25, 45). Additionally, in *Prdm16* cKO hearts, acylcarnitine levels were reduced. It needs to be highlighted that these metabolic changes occurred prior to the cardiac phenotype and made *Prdm16* cKO mutants more vulnerable to metabolic stress (56). In the failing heart, an altered metabolism can present as a consequence (91), or as a possible cause for cardiac dysfunction (92, 93). Diminished mitochondrial oxidative capacity leads to the loss of metabolic

flexibility, and disordered substrate utilisation (58, 60, 61, 94). It is the general consensus that glycolytic rates are increased in the failing heart. (93, 95-97). Usually, anaerobic glycolysis is responsible for this higher flux. Glucose oxidation is uncoupled from this, and therefore reduced or unchanged (95-97) (Figure 29 B). However, conflicting evidence exists. For example, deletion of *long-chain acyl coenzyme synthetase isoform 1* (*Acsl1*) in mice led to higher glucose oxidation rates (92). Others observed lower glycolytic rates in patients with progressed HF (98, 99). Alterations of fatty acid metabolism in the failing heart are uncertain. Some studies suggested that fatty acid oxidation decreases (91, 92, 95), while others suggested that it increases (99). Furthermore, HF is often accompanied by elevated free fatty acid serum levels, especially in cases with obesity, diabetes, and insulin resistance. Substrate delivery impacts cardiac metabolism and makes interpretation of results more difficult (100, 101) (Figure 29 B). This study could not determine in which direction metabolic flux was altered in *Prdm16*$^{csp1/wt}$ hearts, or if energy production was impaired. Also, it remains unclear if the lipid metabolism was affected by systemic heterozygous *Prdm16* deletion. Considering the function of Prdm16 in adipose tissue, it is likely that changes in systemic metabolites and hormones, e.g., adipokines and insulin, were pivotal for the *Prdm16*$^{csp1/wt}$ phenotype. With respect to the mild phenotype, the systematic reduction of central carbon metabolites was impressive. Therefore, we conclude that changes in cardiac metabolism due to *Prdm16* deletion contributed to the onset of cardiac dysfunction.

Western blot analysis of the ETC in heterozygous *Prdm16*$^{csp1/wt}$ mice confirmed that metabolic dysfunction contributes to the *PRDM16* CMP with sex-bias. Reduced expression of complex IV appeared in female *Prdm16*$^{csp1/wt}$ hearts only. This is consistent with previous findings in the hearts of *Prdm16* cKO mice (56) and in adipocytes (20, 21, 23, 32-35, 56): In *Prdm16* cKO hearts, ETC complexes were diminished together with lower expression of genes which are essential for mitochondrial function and increased expression of antioxidative genes (56). In adipocytes, PRDM16 increased the expression of genes with mitochondrial function and directly regulated the activity of the ETC, as evidenced by increased cellular respiration and induced thermogenesis (20, 21, 23, 32-35). Cardiomyocytes predominantly use oxidative phosphorylation at the mitochondrial ETC for energy production in the form of ATP. Simplified, the mechanism looks as follows: TCA, fatty acid oxidation, and glycolysis generate high energy electrons in the form of NADH and

$FADH_2$. In a chain of redox reactions, complexes I-IV use this energy to transport protons from the mitochondrial matrix into the intermembrane space. This creates an electrochemical gradient which drives complex V to generate ATP. Electron carriers are important coenzymes for the ETC, namely: ubiquinone also known as coenzyme Q, for complexes I and III, and cytochrome C for complex IV. At complex IV, molecular O_2 is reduced to H_2O and cytochrome C is oxidised (102) (Figure 29 A). To some extent, the ETC is inefficient and produces ROS, esp. at complexes I and III (Figure 29 B). Excessive ROS can cause severe cell damage (58, 59, 102). Many studies observed ETC dysfunction in CMP and heart failure (58, 103). Complex IV activity and transcript expression are reduced in patients with DCM (104-107). Genetic variants of different ETC components are associated with CMP (94, 105). However, protein expression is only one indicator for ETC function after *Prdm16* deletion and further experiments are required.

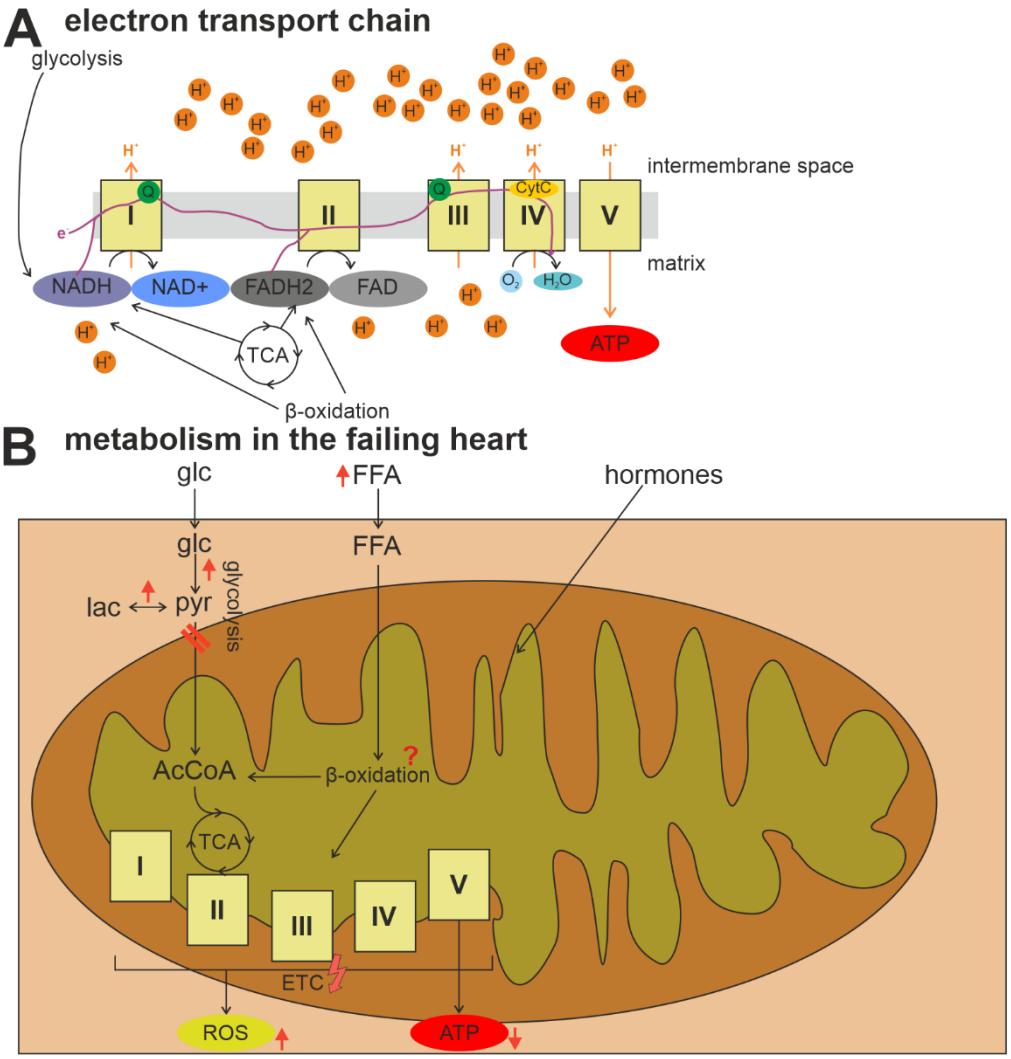

Figure 29. Mechanism of the electron transport chain and energy metabolism in heart failure. A The ETC locates the inner mitochondrial membrane. TCA, glycolysis, and β-oxidation supply NADH and $FADH_2$ as a source of energetic electrons. Redox reactions at the ETC gradually set this energy free to create a proton gradient between intermembrane space and the mitochondrial matrix, which drives ATP synthesis at complex V. Important coenzymes are ubiquinone at complexes I and III, and cytochrome C at complex IV. At complex IV, molecular oxygen becomes reduced. **B** In heart failure, oxidative metabolism in cardiac mitochondria is compromised. Anaerobic glycolysis becomes the main source for ATP production, whilst glucose oxidation is interrupted. Free fatty acids are elevated in the serum, but it is unclear if β-oxidation is changed. Circulating hormones and metabolites might impact myocardial metabolism. A dysfunctional ETC produces less ATP and excessive ROS. Abbreviations: Q –ubiquinone; CytC – cytochrome C; glc – glucose; FFA – free fatty acids; lac – lactate; pyr – pyruvate; AcCoa – acetyl coenzyme A; TCA – tricarboxylic acid cycle; ROS – reactive oxygen species; ATP – adenosin triphosphate.

4.6 Sex as a potential modifier of the *PRDM16* CMP

Interestingly, female *Prdm16*$^{csp1/wt}$ mice showed stronger expression of the CMP phenotype. Since it was first discovered as a CMP disease gene, there has been some data suggesting a connection of PRDM16 with sex. Remarkably, 16 of the 18 patients

with 1p36 deletion syndrome (heterozygous loss of *PRDM16*) and CMP were female (13). Moreover, Nam et al. (48) observed global heart hypertrophy in *Prdm16* cKO females but not in males. This is quite surprising, as in most forms of CMP and HF, the female sex is associated with a less severe phenotype and better outcome (108-110). This applies to several animal models and the human condition (108-112). Exemptions are Takotsubo- or diabetic CMP, with higher prevalence and worse outcomes in females (113, 114), or peripartum CMP, which occurs at the end of, or after pregnancy (115). Most theories explaining this sex dimorphism are based on differences in sex hormones, epigenetics, gene expression, behaviour, lifestyle, and the highly complex interaction between these factors (111). For example., studies suggested a cardioprotective role for estrogen by reducing cardiomyocyte apoptosis (116), inhibiting cardiac fibroblasts (117), or regulating mitochondrial function (118).

This study identified sex differences in the cardiac energy metabolism as a potential contributor for the sex-bias of the *PRDM16* CMP. Metabolic changes were more prominent in female *Prdm16*$^{csp1/wt}$ hearts. More metabolites of the central carbon metabolism were reduced and the changes at the ETC were restricted to *Prdm16*$^{csp1/wt}$ females. Sex differences in myocardial metabolism have previously been described. In healthy women, myocardial glucose utilisation was lower and oxygen consumption was higher compared to men (119). Obese women showed higher fatty acid oxidation rates than obese men (120). The same was true for a rat model of exercise-induced cardiac hypertrophy (121). In HF, women usually present with higher expression of genes involved in energy metabolism (122, 123). A lot of these effects might be mediated by sex hormones like estrogen (111, 118). It seems that female cardiac metabolism is more depending on fatty acid oxidation and oxidative metabolism and therefore more susceptible to alteration in these areas.

4.7 Outlook

This work confirmed a critical role for *PRDM16* in cardiac function and pathophysiology. Analysis of *Prdm16*$^{csp1/wt}$ cardiac physiology introduced a first model for systemic heterozygous *Prdm16* deletion in mammalian CMP. Probably, mitochondrial- and metabolic dysfunction are major determinants for the *PRDM16* CMP. Sex potentially modifies the onset, severity, and pathogenesis of the disease.

NGS analysis realised the characterisation of *Prdm16*^{csp1} transcripts resulting from deficient splicing. However, definite measurement of Prdm16 protein deletion in

Prdm16$^{csp1/wt}$ hearts remains an open question and requires an appropriate technique like quantitative mass spectroscopy.

The differences between *Prdm16*$^{csp1/wt}$ heterozygotes and *Prdm16* cKO homozygotes demonstrate the value of the *Prdm16*$^{csp1/wt}$ strain for understanding the underlying cause of early onset *PRDM16* CMP. The *Prdm16*$^{csp1/wt}$ phenotype is well comparable with human *PRDM16* CMP. Due to its early-stage phenotype the *Prdm16*$^{csp1/wt}$ model is particularly useful for discovering the initial causes of the *PRDM16* CMP as potential targets for prevention and therapy. However, the mild phenotype and the germline character of the *csp1* mutation are a double-edged sword. It is hard to notice the moderate effects of systemic heterozygous *Prdm16* deletion and to decide if their origin lies in the heart. *Prdm16* cKO can help us to distinguish systemic from cardiac-specific *Prdm16* functions. To this end, it is obligatory to identify relevant systemic- and cardiac actions of *PRDM16* for the development of CMP. The combination of findings in systemic and cKO models is the best way to do so.

Furthermore, it is important to monitor the onset and progression of cardiac dysfunction after *Prdm16* deletion. Physiological and molecular analysis of *Prdm16* knockout or induction of the knockout at different time points can help us to understand the role of PRDM16 in variable disease stages and ages. Furthermore, PRDM16 function in embryogenesis can be discussed. *Prdm16* deletion caused abnormal cardiac differentiation and severe LVNC (30, 57). LVNC might arise from alterations in embryonic development (11), and PRDM16 is associated with the differentiation of other tissues (20, 21, 27, 32, 33, 41, 43, 45) and is enriched in cardiac tissue of murine embryos (20, 31).

The most striking results of this work were the heavily affected cardiac metabolism and ETC in *Prdm16*$^{csp1/wt}$ mice. This raises the question if the *PRDM16* CMP is a metabolic CMP and demands further evaluation. *In vivo* GC-MS measurements should be expanded to other metabolite groups, especially lipids involved in energy production. To resolve the question about predominant substrate use in the *PRDM16* deficient heart, the actual uptake and turnover can be measured by ^{13}C metabolic flux analysis. The altered body composition of *Prdm16*^{csp1wt} mice points towards a dysregulated systemic energy homeostasis. Measuring circulating levels of the main energy substrates, e.g., glucose, free fatty acids, or ketone bodies, will show if substrate delivery is abnormal in *Prdm16*^{csp1wt} mice. *In vitro* experiments in human or murine cells after *PRDM16* KO or overexpression are also useful to assess ETC function and

energy production. Simple enzymatic assays can measure individual ETC complex activity. The most sophisticated way to assess ETC and metabolic function in general is the Seahorse XF Analyzer. It can evaluate mitochondrial respiration, ATP production, and glycolysis in a single experiment. Also, it is important to assess the consequences of mitochondrial dysfunction like excessive ROS generation and ROS mediated damage. For example, oxidative stress can be assessed by measuring ROS levels with fluorescent probes or by measuring oxidative modifications of biomolecules. Further open questions are: Is the altered metabolism due to *Prdm16* deficiency adaptive or maladaptive? Which factors improve or aggravate the condition? Is the transition from bench to bedside possible? Can we draw conclusions for the treatment and prevention of human CMP? A helpful approach to answer these questions is to test how *Prdm16*$^{csp1/wt}$ mice respond to cardiac stress like a high fat diet, which was shown to cause mitochondrial dysfunction and CMP in rat hearts (124). Moreover, the MC4R antagonism is a promising treatment to test in the mammalian heart, as this reversed the phenotype of *PRDM16* deficient zebrafish (125).

This work provided further evidence that sex is a potential modifier of the *PRDM16* CMP, being likely due to sex differences in cardiac metabolism. Future studies investigating *PRDM16* function must pay attention to this. In animal models, both sexes should be evaluated separately. In human cohorts, it can be checked if the prevalence of *PRDM16* variants differs between males and females and if they are associated with worse outcomes in females. For *Prdm16*$^{csp1/wt}$ mice, it is interesting to know if the hormonal status is changed in plasma or tissue, e.g., with different levels of sex hormones and their receptor subtypes.

In the RNA sequencing analysis, we partially excluded known PRDM16 functions like transcriptional regulation, interaction with transcription factors, or regulation of TGF-β as the prime cause of the *PRDM16* CMP. However, this must be confirmed or falsified by further experiments like ChIP-sequencing, co-immunoprecipitation, or Western blot analysis for phosphorylation of TGF-β.

5 References

1. Maron Barry J, Towbin Jeffrey A, Thiene G, Antzelevitch C, Corrado D, Arnett D, Moss Arthur J, Seidman Christine E, Young James B. Contemporary Definitions and Classification of the Cardiomyopathies. Circulation. 2006;113(14):1807-16.
2. Elliott P, Andersson B, Arbustini E, Bilinska Z, Cecchi F, Charron P, Dubourg O, Kühl U, Maisch B, McKenna WJ, Monserrat L, Pankuweit S, Rapezzi C, Seferovic P, Tavazzi L, Keren A. Classification of the cardiomyopathies: a position statement from the european society of cardiology working group on myocardial and pericardial diseases. European Heart Journal. 2008;29(2):270-6.
3. Burke MA, Cook SA, Seidman JG, Seidman CE. Clinical and Mechanistic Insights Into the Genetics of Cardiomyopathy. J Am Coll Cardiol. 2016;68(25):2871-86.
4. Hershberger RE, Givertz MM, Ho CY, Judge DP, Kantor PF, McBride KL, Morales A, Taylor MRG, Vatta M, Ware SM. Genetic Evaluation of Cardiomyopathy-A Heart Failure Society of America Practice Guideline. Journal of cardiac failure. 2018;24(5):281-302.
5. Brieler J, Breeden MA, Tucker J. Cardiomyopathy: An Overview. American family physician. 2017;96(10):640-6.
6. Ware JS, Cook SA. Role of titin in cardiomyopathy: from DNA variants to patient stratification. Nature Reviews Cardiology. 2018;15(4):241-52.
7. Towbin JA. Inherited cardiomyopathies. Circ J. 2014;78(10):2347-56.
8. Fatkin D, Graham RM. Molecular Mechanisms of Inherited Cardiomyopathies. Physiological Reviews. 2002;82(4):945-80.
9. Sacchetto C, Sequeira V, Bertero E, Dudek J, Maack C, Calore M. Metabolic Alterations in Inherited Cardiomyopathies. J Clin Med. 2019;8(12):2195.
10. Arbustini E, Favalli V, Narula N, Serio A, Grasso M. Left Ventricular Noncompaction: A Distinct Genetic Cardiomyopathy? J Am Coll Cardiol. 2016;68(9):949-66.
11. Zhang W, Chen H, Qu X, Chang C-P, Shou W. Molecular mechanism of ventricular trabeculation/compaction and the pathogenesis of the left ventricular noncompaction cardiomyopathy (LVNC). Am J Med Genet C Semin Med Genet. 2013;163C(3):144-56.

12. Kühnisch J, Herbst C, Al-Wakeel-Marquard N, Dartsch J, Holtgrewe M, Baban A, Mearini G, Hardt J, Kolokotronis K, Gerull B, Carrier L, Beule D, Schubert S, Messroghli D, Degener F, Berger F, Klaassen S. Targeted panel sequencing in pediatric primary cardiomyopathy supports a critical role of TNNI3. Clinical Genetics. 2019;96(6):549-59.
13. Arndt A-K, Schafer S, Drenckhahn J-D, Sabeh MK, Plovie ER, Caliebe A, Klopocki E, Musso G, Werdich AA, Kalwa H, Heinig M, Padera RF, Wassilew K, Bluhm J, Harnack C, Martitz J, Barton PJ, Greutmann M, Berger F, Hubner N, Siebert R, Kramer H-H, Cook SA, MacRae CA, Klaassen S. Fine mapping of the 1p36 deletion syndrome identifies mutation of PRDM16 as a cause of cardiomyopathy. Am J Hum Genet. 2013;93(1):67-77.
14. Battaglia A, Hoyme HE, Dallapiccola B, Zackai E, Hudgins L, McDonald-McGinn D, Bahi-Buisson N, Romano C, Williams CA, Brailey LL, Zuberi SM, Carey JC. Further delineation of deletion 1p36 syndrome in 60 patients: a recognizable phenotype and common cause of developmental delay and mental retardation. Pediatrics. 2008;121(2):404-10.
15. UniProt: the universal protein knowledgebase in 2021 [Internet]. 2021 [cited 16.06.2021]. Available from: https://www.uniprot.org/.
16. Ensembl 2021 [Internet]. 2021 [cited 18.06.2021]. Available from: https://www.ensembl.org/.
17. Nishikata I, Sasaki H, Iga M, Tateno Y, Imayoshi S, Asou N, Nakamura T, Morishita K. A novel EVI1 gene family, MEL1, lacking a PR domain (MEL1S) is expressed mainly in t(1;3)(p36;q21)-positive AML and blocks G-CSF-induced myeloid differentiation. Blood. 2003;102(9):3323-32.
18. Zhou B, Wang J, Lee SY, Xiong J, Bhanu N, Guo Q, Ma P, Sun Y, Rao RC, Garcia BA, Hess JL, Dou Y. PRDM16 Suppresses MLL1r Leukemia via Intrinsic Histone Methyltransferase Activity. Mol Cell. 2016;62(2):222-36.
19. Pinheiro I, Margueron R, Shukeir N, Eisold M, Fritzsch C, Richter FM, Mittler G, Genoud C, Goyama S, Kurokawa M, Son J, Reinberg D, Lachner M, Jenuwein T. Prdm3 and Prdm16 are H3K9me1 methyltransferases required for mammalian heterochromatin integrity. Cell. 2012;150(5):948-60.
20. Seale P, Bjork B, Yang W, Kajimura S, Chin S, Kuang S, Scimè A, Devarakonda S, Conroe HM, Erdjument-Bromage H, Tempst P, Rudnicki MA, Beier DR, Spiegelman

BM. PRDM16 controls a brown fat/skeletal muscle switch. Nature. 2008;454(7207):961-7.
21. Seale P, Kajimura S, Yang W, Chin S, Rohas LM, Uldry M, Tavernier G, Langin D, Spiegelman BM. Transcriptional control of brown fat determination by PRDM16. Cell Metab. 2007;6(1):38-54.
22. Kajimura S, Seale P, Kubota K, Lunsford E, Frangioni JV, Gygi SP, Spiegelman BM. Initiation of myoblast to brown fat switch by a PRDM16-C/EBP-beta transcriptional complex. Nature. 2009;460(7259):1154-8.
23. Kajimura S, Seale P, Tomaru T, Erdjument-Bromage H, Cooper MP, Ruas JL, Chin S, Tempst P, Lazar MA, Spiegelman BM. Regulation of the brown and white fat gene programs through a PRDM16/CtBP transcriptional complex. Genes Dev. 2008;22(10):1397-409.
24. Takahata M, Inoue Y, Tsuda H, Imoto I, Koinuma D, Hayashi M, Ichikura T, Yamori T, Nagasaki K, Yoshida M, Matsuoka M, Morishita K, Yuki K, Hanyu A, Miyazawa K, Inazawa J, Miyazono K, Imamura T. SKI and MEL1 cooperate to inhibit transforming growth factor-beta signal in gastric cancer cells. The Journal of biological chemistry. 2009;284(5):3334-44.
25. Ohno H, Shinoda K, Ohyama K, Sharp LZ, Kajimura S. EHMT1 controls brown adipose cell fate and thermogenesis through the PRDM16 complex. Nature. 2013;504(7478):163-7.
26. Hasegawa Y, Ikeda K, Chen Y, Alba DL, Stifler D, Shinoda K, Hosono T, Maretich P, Yang Y, Ishigaki Y, Chi J, Cohen P, Koliwad SK, Kajimura S. Repression of Adipose Tissue Fibrosis through a PRDM16-GTF2IRD1 Complex Improves Systemic Glucose Homeostasis. Cell Metab. 2018;27(1):180-94.e6.
27. Inoue M, Iwai R, Tabata H, Konno D, Komabayashi-Suzuki M, Watanabe C, Iwanari H, Mochizuki Y, Hamakubo T, Matsuzaki F, Nagata KI, Mizutani KI. Prdm16 is crucial for progression of the multipolar phase during neural differentiation of the developing neocortex. Development (Cambridge, England). 2017;144(3):385-99.
28. Iida S, Chen W, Nakadai T, Ohkuma Y, Roeder RG. PRDM16 enhances nuclear receptor-dependent transcription of the brown fat-specific Ucp1 gene through interactions with Mediator subunit MED1. Genes Dev. 2015;29(3):308-21.
29. Harms MJ, Lim H-W, Ho Y, Shapira SN, Ishibashi J, Rajakumari S, Steger DJ, Lazar MA, Won K-J, Seale P. PRDM16 binds MED1 and controls chromatin

architecture to determine a brown fat transcriptional program. Genes Dev. 2015;29(3):298-307.
30. Bjork BC, Turbe-Doan A, Prysak M, Herron BJ, Beier DR. Prdm16 is required for normal palatogenesis in mice. Human molecular genetics. 2010;19(5):774-89.
31. Horn KH, Warner DR, Pisano M, Greene RM. PRDM16 expression in the developing mouse embryo. Acta Histochem. 2011;113(2):150-5.
32. Harms MJ, Ishibashi J, Wang W, Lim HW, Goyama S, Sato T, Kurokawa M, Won KJ, Seale P. Prdm16 is required for the maintenance of brown adipocyte identity and function in adult mice. Cell Metab. 2014;19(4):593-604.
33. Cohen P, Levy JD, Zhang Y, Frontini A, Kolodin DP, Svensson KJ, Lo JC, Zeng X, Ye L, Khandekar MJ, Wu J, Gunawardana SC, Banks AS, Camporez JP, Jurczak MJ, Kajimura S, Piston DW, Mathis D, Cinti S, Shulman GI, Seale P, Spiegelman BM. Ablation of PRDM16 and beige adipose causes metabolic dysfunction and a subcutaneous to visceral fat switch. Cell. 2014;156(1-2):304-16.
34. Seale P, Conroe HM, Estall J, Kajimura S, Frontini A, Ishibashi J, Cohen P, Cinti S, Spiegelman BM. Prdm16 determines the thermogenic program of subcutaneous white adipose tissue in mice. The Journal of clinical investigation. 2011;121(1):96-105.
35. Ohno H, Shinoda K, Spiegelman BM, Kajimura S. PPARγ agonists induce a white-to-brown fat conversion through stabilization of PRDM16 protein. Cell Metab. 2012;15(3):395-404.
36. Dempersmier J, Sambeat A, Gulyaeva O, Paul SM, Hudak CSS, Raposo HF, Kwan H-Y, Kang C, Wong RHF, Sul HS. Cold-inducible Zfp516 activates UCP1 transcription to promote browning of white fat and development of brown fat. Mol Cell. 2015;57(2):235-46.
37. Huang L, Pan D, Chen Q, Zhu LJ, Ou J, Wabitsch M, Wang YX. Transcription factor Hlx controls a systematic switch from white to brown fat through Prdm16-mediated co-activation. Nature communications. 2017;8(1):68.
38. Liao J, Jiang J, Jun H, Qiao X, Emont MP, Kim DI, Wu J. HDAC3-Selective Inhibition Activates Brown and Beige Fat Through PRDM16. Endocrinology. 2018;159(7):2520-7.
39. Ivanochko D, Halabelian L, Henderson E, Savitsky P, Jain H, Marcon E, Duan S, Hutchinson A, Seitova A, Barsyte-Lovejoy D, Filippakopoulos P, Greenblatt J, Lima-Fernandes E, Arrowsmith CH. Direct interaction between the PRDM3 and PRDM16

tumor suppressors and the NuRD chromatin remodeling complex. Nucleic Acids Res. 2019;47(3):1225-38.

40. Torchy MP, Hamiche A, Klaholz BP. Structure and function insights into the NuRD chromatin remodeling complex. Cellular and molecular life sciences : CMLS. 2015;72(13):2491-507.

41. Aguilo F, Avagyan S, Labar A, Sevilla A, Lee DF, Kumar P, Lemischka IR, Zhou BY, Snoeck HW. Prdm16 is a physiologic regulator of hematopoietic stem cells. Blood. 2011;117(19):5057-66.

42. Chuikov S, Levi BP, Smith ML, Morrison SJ. Prdm16 promotes stem cell maintenance in multiple tissues, partly by regulating oxidative stress. Nat Cell Biol. 2010;12(10):999-1006.

43. Shimada IS, Acar M, Burgess RJ, Zhao Z, Morrison SJ. Prdm16 is required for the maintenance of neural stem cells in the postnatal forebrain and their differentiation into ependymal cells. Genes Dev. 2017;31(11):1134-46.

44. Chui A, Zhang Q, Dai Q, Shi SH. Oxidative stress regulates progenitor behavior and cortical neurogenesis. Development (Cambridge, England). 2020;147(5).

45. Stine RR, Sakers AP, TeSlaa T, Kissig M, Stine ZE, Kwon CW, Cheng L, Lim HW, Kaestner KH, Rabinowitz JD, Seale P. PRDM16 Maintains Homeostasis of the Intestinal Epithelium by Controlling Region-Specific Metabolism. Cell stem cell. 2019;25(6):830-45.e8.

46. Goumans M-J, Ten Dijke P. TGF-β Signaling in Control of Cardiovascular Function. Cold Spring Harb Perspect Biol. 2018;10(2):a022210.

47. Warner DR, Horn KH, Mudd L, Webb CL, Greene RM, Pisano MM. PRDM16/MEL1: a novel Smad binding protein expressed in murine embryonic orofacial tissue. Biochim Biophys Acta. 2007;1773(6):814-20.

48. Nam JM, Lim JE, Ha TW, Oh B, Kang J-O. Cardiac-specific inactivation of Prdm16 effects cardiac conduction abnormalities and cardiomyopathy-associated phenotypes. American Journal of Physiology-Heart and Circulatory Physiology. 2020;318(4):H764-H77.

49. Su L, Lei X, Ma H, Feng C, Jiang J, Jiao J. PRDM16 orchestrates angiogenesis via neural differentiation in the developing brain. Cell death and differentiation. 2020;27(8):2313-29.

50. Yoshida M, Nosaka K, Yasunaga J-i, Nishikata I, Morishita K, Matsuoka M. Aberrant expression of the MEL1S gene identified in association with hypomethylation in adult T-cell leukemia cells. Blood. 2004;103(7):2753-60.
51. Kodo K, Ong S-G, Jahanbani F, Termglinchan V, Hirono K, InanlooRahatloo K, Ebert AD, Shukla P, Abilez OJ, Churko JM, Karakikes I, Jung G, Ichida F, Wu SM, Snyder MP, Bernstein D, Wu JC. iPSC-derived cardiomyocytes reveal abnormal TGF-β signalling in left ventricular non-compaction cardiomyopathy. Nat Cell Biol. 2016;18(10):1031-42.
52. Dorn GW, 2nd, Vega RB, Kelly DP. Mitochondrial biogenesis and dynamics in the developing and diseased heart. Genes Dev. 2015;29(19):1981-91.
53. Luchsinger LL, de Almeida MJ, Corrigan DJ, Mumau M, Snoeck HW. Mitofusin 2 maintains haematopoietic stem cells with extensive lymphoid potential. Nature. 2016;529(7587):528-31.
54. Wang W, Ishibashi J, Trefely S, Shao M, Cowan AJ, Sakers A, Lim HW, O'Connor S, Doan MT, Cohen P, Baur JA, King MT, Veech RL, Won KJ, Rabinowitz JD, Snyder NW, Gupta RK, Seale P. A PRDM16-Driven Metabolic Signal from Adipocytes Regulates Precursor Cell Fate. Cell Metab. 2019;30(1):174-89.e5.
55. Lei Q, Liu X, Fu H, Sun Y, Wang L, Xu G, Wang W, Yu Z, Liu C, Li P, Feng J, Li G, Wu M. miR-101 reverses hypomethylation of the PRDM16 promoter to disrupt mitochondrial function in astrocytoma cells. Oncotarget. 2016;7(4):5007-22.
56. Cibi DM, Bi-Lin KW, Shekeran SG, Sandireddy R, Tee N, Singh A, Wu Y, Srinivasan DK, Kovalik J-P, Ghosh S, Seale P, Singh MK. Prdm16 Deficiency Leads to Age-Dependent Cardiac Hypertrophy, Adverse Remodeling, Mitochondrial Dysfunction, and Heart Failure. Cell Rep. 2020;33(3):108288.
57. Wu T, Liang Z, Zhang Z, Liu C, Zhang L, Gu Y, Peterson KL, Evans SM, Fu X-D, Chen J. PRDM16 Is a Compact Myocardium-Enriched Transcription Factor Required to Maintain Compact Myocardial Cardiomyocyte Identity in Left Ventricle. Circulation.0(0).
58. Marín-García J, Goldenthal MJ. Mitochondrial centrality in heart failure. Heart Failure Reviews. 2008;13(2):137-50.
59. Peoples JN, Saraf A, Ghazal N, Pham TT, Kwong JQ. Mitochondrial dysfunction and oxidative stress in heart disease. Experimental & Molecular Medicine. 2019;51(12):1-13.

60. Karwi QG, Uddin GM, Ho KL, Lopaschuk GD. Loss of Metabolic Flexibility in the Failing Heart. Front Cardiovasc Med. 2018;5:68-.
61. Neubauer S. The Failing Heart — An Engine Out of Fuel. New England Journal of Medicine. 2007;356(11):1140-51.
62. Ritterhoff J, Tian R. Metabolism in cardiomyopathy: every substrate matters. Cardiovasc Res. 2017;113(4):411-21.
63. Schmittgen TD, Livak KJ. Analyzing real-time PCR data by the comparative CT method. Nature Protocols. 2008;3(6):1101-8.
64. Ibrahim M, Siedlecka U, Buyandelger B, Harada M, Rao C, Moshkov A, Bhargava A, Schneider M, Yacoub MH, Gorelik J, Knöll R, Terracciano CM. A critical role for Telethonin in regulating t-tubule structure and function in the mammalian heart. Human molecular genetics. 2013;22(2):372-83.
65. Hayashi T, Arimura T, Itoh-Satoh M, Ueda K, Hohda S, Inagaki N, Takahashi M, Hori H, Yasunami M, Nishi H, Koga Y, Nakamura H, Matsuzaki M, Choi BY, Bae SW, You CW, Han KH, Park JE, Knöll R, Hoshijima M, Chien KR, Kimura A. Tcap gene mutations in hypertrophic cardiomyopathy and dilated cardiomyopathy. J Am Coll Cardiol. 2004;44(11):2192-201.
66. Knöll R, Linke WA, Zou P, Miocic S, Kostin S, Buyandelger B, Ku C-H, Neef S, Bug M, Schäfer K, Knöll G, Felkin LE, Wessels J, Toischer K, Hagn F, Kessler H, Didié M, Quentin T, Maier LS, Teucher N, Unsöld B, Schmidt A, Birks EJ, Gunkel S, Lang P, Granzier H, Zimmermann W-H, Field LJ, Faulkner G, Dobbelstein M, Barton PJR, Sattler M, Wilmanns M, Chien KR. Telethonin deficiency is associated with maladaptation to biomechanical stress in the mammalian heart. Circ Res. 2011;109(7):758-69.
67. Kim H, Kim M, Im S-K, Fang S. Mouse Cre-LoxP system: general principles to determine tissue-specific roles of target genes. Lab Anim Res. 2018;34(4):147-59.
68. Doetschman T, Azhar M. Cardiac-Specific Inducible and Conditional Gene Targeting in Mice. Circ Res. 2012;110(11):1498-512.
69. Tirziu D, Giordano FJ, Simons M. Cell Communications in the Heart. Circulation. 2010;122(9):928-37.
70. Powell-Wiley TM, Poirier P, Burke LE, Després J-P, Gordon-Larsen P, Lavie CJ, Lear SA, Ndumele CE, Neeland IJ, Sanders P, St-Onge M-P, null n. Obesity and Cardiovascular Disease: A Scientific Statement From the American Heart Association. Circulation. 2021;143(21):e984-e1010.

71. Anthony SR, Guarnieri AR, Gozdiff A, Helsley RN, Phillip Owens A, Tranter M. Mechanisms linking adipose tissue inflammation to cardiac hypertrophy and fibrosis. Clin Sci (Lond). 2019;133(22):2329-44.
72. Collins S. A heart–adipose tissue connection in the regulation of energy metabolism. Nature Reviews Endocrinology. 2014;10(3):157-63.
73. Pérez-Belmonte LM, Moreno-Santos I, Gómez-Doblas JJ, García-Pinilla JM, Morcillo-Hidalgo L, Garrido-Sánchez L, Santiago-Fernández C, Crespo-Leiro MG, Carrasco-Chinchilla F, Sánchez-Fernández PL, de Teresa-Galván E, Jiménez-Navarro M. Expression of epicardial adipose tissue thermogenic genes in patients with reduced and preserved ejection fraction heart failure. Int J Med Sci. 2017;14(9):891-5.
74. He Y, Ma N, Tang M, Jiang ZL, Liu H, Mei J. The differentiation of beige adipocyte in pericardial and epicardial adipose tissues induces atrial fibrillation development. European review for medical and pharmacological sciences. 2017;21(19):4398-405.
75. Sacks HS, Fain JN, Bahouth SW, Ojha S, Frontini A, Budge H, Cinti S, Symonds ME. Adult epicardial fat exhibits beige features. The Journal of clinical endocrinology and metabolism. 2013;98(9):E1448-55.
76. Faulx MD, Chandler MP, Zawaneh MS, Stanley WC, Hoit BD. MOUSE STRAIN-SPECIFIC DIFFERENCES IN CARDIAC METABOLIC ENZYME ACTIVITIES OBSERVED IN A MODEL OF ISOPROTERENOL-INDUCED CARDIAC HYPERTROPHY. Clinical and Experimental Pharmacology and Physiology. 2007;34(1-2):77-80.
77. Kiper C, Grimes B, Van Zant G, Satin J. Mouse Strain Determines Cardiac Growth Potential. PLOS ONE. 2013;8(8):e70512.
78. Shusterman V, Usiene I, Harrigal C, Lee JS, Kubota T, Feldman AM, London B. Strain-specific patterns of autonomic nervous system activity and heart failure susceptibility in mice. American Journal of Physiology-Heart and Circulatory Physiology. 2002;282(6):H2076-H83.
79. Cundrle I, Jr., Olson LJ, Johnson BD. Pulmonary Limitations in Heart Failure. Clin Chest Med. 2019;40(2):439-48.
80. Guazzi M, Naeije R. Pulmonary Hypertension in Heart Failure: Pathophysiology, Pathobiology, and Emerging Clinical Perspectives. J Am Coll Cardiol. 2017;69(13):1718-34.

81. Guazzi M, Borlaug BA. Pulmonary Hypertension Due to Left Heart Disease. Circulation. 2012;126(8):975-90.
82. Symonds ME, Aldiss P, Pope M, Budge H. Recent advances in our understanding of brown and beige adipose tissue: the good fat that keeps you healthy. F1000Res. 2018;7:F1000 Faculty Rev-129.
83. Thienpont B, Aronsen JM, Robinson EL, Okkenhaug H, Loche E, Ferrini A, Brien P, Alkass K, Tomasso A, Agrawal A, Bergmann O, Sjaastad I, Reik W, Roderick HL. The H3K9 dimethyltransferases EHMT1/2 protect against pathological cardiac hypertrophy. The Journal of clinical investigation. 2017;127(1):335-48.
84. Martin OJ, Lai L, Soundarapandian MM, Leone TC, Zorzano A, Keller MP, Attie AD, Muoio DM, Kelly DP. A Role for Peroxisome Proliferator-Activated Receptor γ Coactivator-1 in the Control of Mitochondrial Dynamics During Postnatal Cardiac Growth. Circ Res. 2014;114(4):626-36.
85. Lehman JJ, Barger PM, Kovacs A, Saffitz JE, Medeiros DM, Kelly DP. Peroxisome proliferator–activated receptor γ coactivator-1 promotes cardiac mitochondrial biogenesis. The Journal of clinical investigation. 2000;106(7):847-56.
86. Russell LK, Mansfield CM, Lehman JJ, Kovacs A, Courtois M, Saffitz JE, Medeiros DM, Valencik ML, McDonald JA, Kelly DP. Cardiac-Specific Induction of the Transcriptional Coactivator Peroxisome Proliferator-Activated Receptor γ Coactivator-1α Promotes Mitochondrial Biogenesis and Reversible Cardiomyopathy in a Developmental Stage-Dependent Manner. Circ Res. 2004;94(4):525-33.
87. Kaimoto S, Hoshino A, Ariyoshi M, Okawa Y, Tateishi S, Ono K, Uchihashi M, Fukai K, Iwai-Kanai E, Matoba S. Activation of PPAR-α in the early stage of heart failure maintained myocardial function and energetics in pressure-overload heart failure. American Journal of Physiology-Heart and Circulatory Physiology. 2016;312(2):H305-H13.
88. Arany Z, He H, Lin J, Hoyer K, Handschin C, Toka O, Ahmad F, Matsui T, Chin S, Wu P-H, Rybkin II, Shelton JM, Manieri M, Cinti S, Schoen FJ, Bassel-Duby R, Rosenzweig A, Ingwall JS, Spiegelman BM. Transcriptional coactivator PGC-1α controls the energy state and contractile function of cardiac muscle. Cell Metab. 2005;1(4):259-71.
89. Kärkkäinen O, Tuomainen T, Mutikainen M, Lehtonen M, Ruas JL, Hanhineva K, Tavi P. Heart specific PGC-1α deletion identifies metabolome of cardiac restricted metabolic heart failure. Cardiovasc Res. 2019;115(1):107-18.

90. Haemmerle G, Moustafa T, Woelkart G, Büttner S, Schmidt A, van de Weijer T, Hesselink M, Jaeger D, Kienesberger PC, Zierler K, Schreiber R, Eichmann T, Kolb D, Kotzbeck P, Schweiger M, Kumari M, Eder S, Schoiswohl G, Wongsiriroj N, Pollak NM, Radner FPW, Preiss-Landl K, Kolbe T, Rülicke T, Pieske B, Trauner M, Lass A, Zimmermann R, Hoefler G, Cinti S, Kershaw EE, Schrauwen P, Madeo F, Mayer B, Zechner R. ATGL-mediated fat catabolism regulates cardiac mitochondrial function via PPAR-α and PGC-1. Nat Med. 2011;17(9):1076-85.
91. Barger PM, Kelly DP. Fatty Acid Utilization in the Hypertrophied and Failing Heart: Molecular Regulatory Mechanisms. The American Journal of the Medical Sciences. 1999;318(1):36-42.
92. Ellis Jessica M, Mentock Shannon M, DePetrillo Michael A, Koves Timothy R, Sen S, Watkins Steven M, Muoio Deborah M, Cline Gary W, Taegtmeyer H, Shulman Gerald I, Willis Monte S, Coleman Rosalind A. Mouse Cardiac Acyl Coenzyme A Synthetase 1 Deficiency Impairs Fatty Acid Oxidation and Induces Cardiac Hypertrophy. Molecular and Cellular Biology. 2011;31(6):1252-62.
93. Hamirani YS, Kundu BK, Zhong M, McBride A, Li Y, Davogustto GE, Taegtmeyer H, Bourque JM. Noninvasive Detection of Early Metabolic Left Ventricular Remodeling in Systemic Hypertension. Cardiology. 2016;133(3):157-62.
94. Casademont J, Miró Ò. Electron Transport Chain Defects in Heart Failure. Heart Failure Reviews. 2002;7(2):131-9.
95. Allard MF, Schönekess BO, Henning SL, English DR, Lopaschuk GD. Contribution of oxidative metabolism and glycolysis to ATP production in hypertrophied hearts. The American journal of physiology. 1994;267(2 Pt 2):H742-50.
96. Seymour A-ML, Giles L, Ball V, Miller JJ, Clarke K, Carr CA, Tyler DJ. In vivo assessment of cardiac metabolism and function in the abdominal aortic banding model of compensated cardiac hypertrophy. Cardiovasc Res. 2015;106(2):249-60.
97. Fillmore N, Levasseur JL, Fukushima A, Wagg CS, Wang W, Dyck JRB, Lopaschuk GD. Uncoupling of glycolysis from glucose oxidation accompanies the development of heart failure with preserved ejection fraction. Molecular Medicine. 2018;24(1):3.
98. Kalsi KK, Smolenski RT, Pritchard RD, Khaghani A, Seymour AML, Yacoub MH. Energetics and function of the failing human heart with dilated or hypertrophic cardiomyopathy. European Journal of Clinical Investigation. 1999;29(6):469-77.

99. Taylor M, Wallhaus TR, DeGrado TR, Russell DC, Stanko P, Nickles RJ, Stone CK. An Evaluation of Myocardial Fatty Acid and Glucose Uptake Using PET with [^{18}F]Fluoro-6-Thia-Heptadecanoic Acid and [^{18}F]FDG in Patients with Congestive Heart Failure. Journal of Nuclear Medicine. 2001;42(1):55.
100. Mazumder PK, O'Neill BT, Roberts MW, Buchanan J, Yun UJ, Cooksey RC, Boudina S, Abel ED. Impaired cardiac efficiency and increased fatty acid oxidation in insulin-resistant ob/ob mouse hearts. Diabetes. 2004;53(9):2366-74.
101. Zhang L, Jaswal JS, Ussher JR, Sankaralingam S, Wagg C, Zaugg M, Lopaschuk GD. Cardiac insulin-resistance and decreased mitochondrial energy production precede the development of systolic heart failure after pressure-overload hypertrophy. Circulation Heart failure. 2013;6(5):1039-48.
102. Nolfi-Donegan D, Braganza A, Shiva S. Mitochondrial electron transport chain: Oxidative phosphorylation, oxidant production, and methods of measurement. Redox Biol. 2020;37:101674-.
103. Hassanpour SH, Dehghani MA, Karami SZ. Study of respiratory chain dysfunction in heart disease. J Cardiovasc Thorac Res. 2018;10(1):1-13.
104. Quigley AF, Kapsa RMI, Esmore D, Hale G, Byrne E. Mitochondrial respiratory chain activity in idiopathic dilated cardiomyopathy. Journal of cardiac failure. 2000;6(1):47-55.
105. Arbustini E, Diegoli M, Fasani R, Grasso M, Morbini P, Banchieri N, Bellini O, Dal Bello B, Pilotto A, Magrini G, Campana C, Fortina P, Gavazzi A, Narula J, Viganò M. Mitochondrial DNA mutations and mitochondrial abnormalities in dilated cardiomyopathy. Am J Pathol. 1998;153(5):1501-10.
106. Vogt S, Ruppert V, Pankuweit S, Paletta JPJ, Rhiel A, Weber P, Irqsusi M, Cybulski P, Ramzan R. Myocardial insufficiency is related to reduced subunit 4 content of cytochrome c oxidase. Journal of Cardiothoracic Surgery. 2018;13(1):95.
107. Buchwald A, Till H, Unterberg C, Oberschmidt R, Figulla HR, Wiegand V. Alterations of the mitochondrial respiratory chain in human dilated cardiomyopathy. European Heart Journal. 1990;11(6):509-16.
108. Roger VL, Weston SA, Redfield MM, Hellermann-Homan JP, Killian J, Yawn BP, Jacobsen SJ. Trends in Heart Failure Incidence and Survival in a Community-Based Population. JAMA. 2004;292(3):344-50.

109. Levy D, Kenchaiah S, Larson MG, Benjamin EJ, Kupka MJ, Ho KKL, Murabito JM, Vasan RS. Long-Term Trends in the Incidence of and Survival with Heart Failure. New England Journal of Medicine. 2002;347(18):1397-402.
110. Meyer S, van der Meer P, van Tintelen JP, van den Berg MP. Sex differences in cardiomyopathies. European Journal of Heart Failure. 2014;16(3):238-47.
111. Regitz-Zagrosek V, Kararigas G. Mechanistic Pathways of Sex Differences in Cardiovascular Disease. Physiological Reviews. 2016;97(1):1-37.
112. Du X-J. Gender modulates cardiac phenotype development in genetically modified mice. Cardiovasc Res. 2004;63(3):510-9.
113. Lyon AR, Bossone E, Schneider B, Sechtem U, Citro R, Underwood SR, Sheppard MN, Figtree GA, Parodi G, Akashi YJ, Ruschitzka F, Filippatos G, Mebazaa A, Omerovic E. Current state of knowledge on Takotsubo syndrome: a Position Statement from the Taskforce on Takotsubo Syndrome of the Heart Failure Association of the European Society of Cardiology. European Journal of Heart Failure. 2016;18(1):8-27.
114. Toedebusch R, Belenchia A, Pulakat L. Diabetic Cardiomyopathy: Impact of Biological Sex on Disease Development and Molecular Signatures. Front Physiol. 2018;9:453-.
115. Elkayam U. Clinical characteristics of peripartum cardiomyopathy in the United States: diagnosis, prognosis, and management. J Am Coll Cardiol. 2011;58(7):659-70.
116. Patten RD, Pourati I, Aronovitz MJ, Baur J, Celestin F, Chen X, Michael A, Haq S, Nuedling S, Grohe C, Force T, Mendelsohn ME, Karas RH. 17beta-estradiol reduces cardiomyocyte apoptosis in vivo and in vitro via activation of phospho-inositide-3 kinase/Akt signaling. Circ Res. 2004;95(7):692-9.
117. Dubey RK, Gillespie DG, Jackson EK, Keller PJ. 17Beta-estradiol, its metabolites, and progesterone inhibit cardiac fibroblast growth. Hypertension (Dallas, Tex : 1979). 1998;31(1 Pt 2):522-8.
118. Rattanasopa C, Phungphong S, Wattanapermpool J, Bupha-Intr T. Significant role of estrogen in maintaining cardiac mitochondrial functions. The Journal of Steroid Biochemistry and Molecular Biology. 2015;147:1-9.
119. Peterson LR, Soto PF, Herrero P, Schechtman KB, Dence C, Gropler RJ. Sex differences in myocardial oxygen and glucose metabolism. Journal of nuclear cardiology : official publication of the American Society of Nuclear Cardiology. 2007;14(4):573-81.

120. Peterson Linda R, Soto Pablo F, Herrero P, Mohammed BS, Avidan Michael S, Schechtman Kenneth B, Dence C, Gropler Robert J. Impact of Gender on the Myocardial Metabolic Response to Obesity. JACC: Cardiovascular Imaging. 2008;1(4):424-33.
121. Foryst-Ludwig A, Kreissl MC, Sprang C, Thalke B, Böhm C, Benz V, Gürgen D, Dragun D, Schubert C, Mai K, Stawowy P, Spranger J, Regitz-Zagrosek V, Unger T, Kintscher U. Sex differences in physiological cardiac hypertrophy are associated with exercise-mediated changes in energy substrate availability. American Journal of Physiology-Heart and Circulatory Physiology. 2011;301(1):H115-H22.
122. Haddad GE, Saunders LJ, Crosby SD, Carles M, del Monte F, King K, Bristow MR, Spinale FG, Macgillivray TE, Semigran MJ, Dec GW, Williams SA, Hajjar RJ, Gwathmey JK. Human cardiac-specific cDNA array for idiopathic dilated cardiomyopathy: sex-related differences. Physiological Genomics. 2008;33(2):267-77.
123. Heidecker B, Lamirault G, Kasper EK, Wittstein IS, Champion HC, Breton E, Russell SD, Hall J, Kittleson MM, Baughman KL, Hare JM. The gene expression profile of patients with new-onset heart failure reveals important gender-specific differences†. European Heart Journal. 2010;31(10):1188-96.
124. Zeng H, Vaka VR, He X, Booz GW, Chen J-X. High-fat diet induces cardiac remodelling and dysfunction: assessment of the role played by SIRT3 loss. Journal of Cellular and Molecular Medicine. 2015;19(8):1847-56.
125. Arndt AK, Beerens M, Kramer HH, Klaassen S, MacRae CA. PRDM16 - A Novel Key Player in Personalized Medicine. Thorac Cardiovasc Surg. 2015;63(S 03):V0031.

6 Eidesstattliche Versicherung

„Ich, Simon Theisen, versichere an Eides statt durch meine eigenhändige Unterschrift, dass ich die vorgelegte Dissertation mit dem Thema: „Characterisation of the *Prdm16*$^{csp1/wt}$ mouse as a model for the *PRDM16* associated Cardiomyopathy / Charakterisierung der *Prdm16*$^{csp1/wt}$ Maus als ein Modell für die *PRDM16* assoziierte Kardiomyopathie“ selbstständig und ohne nicht offengelegte Hilfe Dritter verfasst und keine anderen als die angegebenen Quellen und Hilfsmittel genutzt habe.
Alle Stellen, die wörtlich oder dem Sinne nach auf Publikationen oder Vorträgen anderer Autoren/innen beruhen, sind als solche in korrekter Zitierung kenntlich gemacht. Die Abschnitte zu Methodik (insbesondere praktische Arbeiten, Laborbestimmungen, statistische Aufarbeitung) und Resultaten (insbesondere Abbildungen, Graphiken und Tabellen) werden von mir verantwortet.

Ich versichere ferner, dass ich die in Zusammenarbeit mit anderen Personen generierten Daten, Datenauswertungen und Schlussfolgerungen korrekt gekennzeichnet und meinen eigenen Beitrag sowie die Beiträge anderer Personen korrekt kenntlich gemacht habe (siehe Anteilserklärung). Texte oder Textteile, die gemeinsam mit anderen erstellt oder verwendet wurden, habe ich korrekt kenntlich gemacht.

Meine Anteile an etwaigen Publikationen zu dieser Dissertation entsprechen denen, die in der untenstehenden gemeinsamen Erklärung mit der Erstbetreuerin, angegeben sind. Für sämtliche im Rahmen der Dissertation entstandenen Publikationen wurden die Richtlinien des ICMJE (International Committee of Medical Journal Editors; www.icmje.og) zur Autorenschaft eingehalten. Ich erkläre ferner, dass ich mich zur Einhaltung der Satzung der Charité – Universitätsmedizin Berlin zur Sicherung Guter Wissenschaftlicher Praxis verpflichte.

Weiterhin versichere ich, dass ich diese Dissertation weder in gleicher noch in ähnlicher Form bereits an einer anderen Fakultät eingereicht habe.

Die Bedeutung dieser eidesstattlichen Versicherung und die strafrechtlichen Folgen einer unwahren eidesstattlichen Versicherung (§§156, 161 des Strafgesetzbuches) sind mir bekannt und bewusst.“

Datum Unterschrift

7 Curriculum vitae

Mein Lebenslauf wird aus datenschutzrechtlichen Gründen in der elektronischen Version meiner Arbeit nicht veröffentlicht

8 Acknowledgments

I would like to thank Prof. Dr. Sabine Klaassen of the Experimental and Clinical Research Center Berlin for the subject, the possibility to accomplish my doctorate degree in her lab, and the critical review of my manuscript. I am most grateful for the trust she put in me. I thank her for encouraging and supporting me to work hard for writing this thesis, also for the great advice she gave me for my dissertation and my future career.

Furthermore, I would like to thank Dr. Jirko Kuehnisch from the Klaassen lab in the Experimental and Clinical Research Center Berlin for the tremendous support during the whole procedure of this dissertation. I really appreciate his great advice for the experimental approach, interpretation of the results, and writing this manuscript. I am thankful for his intellectual input, which helped enormously with writing my thesis.

Also, I really need to thank Josephine Dartsch from the Klaassen lab in the Experimental and Clinical Research Center Berlin who patiently introduced me to several experimental procedures.

I thank the German Centre for Cardiovascular Research (DZHK) for supporting me with the DZHK Doctoral Scholarship.

I have to thank several people of the Berlin Institute of Health (BIH), the Charité university hospital, and the Max-Delbrück-Center (MDC). For the handling of RNA-sequencing I thank Dr. Tatiana Borodina and Sascha Sauer (Core Unit Genomics). For the analysis of high-throughput sequencing data I thank Dr. Benedikt Obermayer (BIH, Core Unit Bioinformatics) For the GC-MS analysis I thank Dr. Raphaela Fritsche-Guenther and Alina Eisenberger (BIH, Core Unit Metabolomics). I thank Dr. Sara Timm and Petra Schrade (Core Facility for Electron Microscopy of the Charité university hospital, Berlin) for the help with TEM. I thank Stefanie Schelenz and Martin Taube (MDC, animal facility) Also I thank Dr. Anca Margineanu, Dr. Anje Sporbert, and Dr. Sandra Cristina Carneiro Raimundo for the technical support with the Advanced Light Microscopy Technology Platform (MDC).

Last but not least I thank my family and my friends for their support throughout my entire life. This would not have been possible without them. Special thanks go to Paula Barthel and Therese Metasch for proofreading.

9 Bescheinigung eines akkreditierten Statistikers

CharitéCentrum für Human- und Gesundheitswissenschaften

Charité | Campus Charité Mitte | 10117 Berlin

Name, Vorname: Theisen, Simon
Emailadresse: simon.theisen@charite.de
Matrikelnummer: 223219
PromotionsbetreuerIn: PD Dr. Sabine Klaassen
Promotionsinstitution / Klinik: Experimental and Clinical Research Center (MDC & Charite), Genetik von Angeborenen Herzerkrankungen

Institut für Biometrie und klinische Epidemiologie (iBikE)
Direktor: Prof. Dr. Geraldine Rauch

Postanschrift:
Charitéplatz 1 | 10117 Berlin
Besucheranschrift:
Reinhardtstr. 58 | 10117 Berlin

Tel. +49 (0)30 450 562171
geraldine.rauch@charite.de
https://biometrie.charite.de/

Bescheinigung

Hiermit bescheinige ich, dass Herr Simon Theisen innerhalb der Service Unit Biometrie des Instituts für Biometrie und klinische Epidemiologie (iBikE) bei mir eine statistische Beratung zu einem Promotionsvorhaben wahrgenommen hat. Folgende Beratungstermine wurden wahrgenommen:

- *Termin 1: 10.08.2021*

Folgende wesentliche Ratschläge hinsichtlich einer sinnvollen Auswertung und Interpretation der Daten wurden während der Beratung erteilt:

- *Prüfung der Verteilungen auf Symmetrie – dann erst sind Mittelwertvergleiche sinnvoll*
- *Beschreibung des T-Test in Bildunterschriften korrigieren*

Diese Bescheinigung garantiert nicht die richtige Umsetzung der in der Beratung gemachten Vorschläge, die korrekte Durchführung der empfohlenen statistischen Verfahren und die richtige Darstellung und Interpretation der Ergebnisse. Die Verantwortung hierfür obliegt allein dem Promovierenden. Das Institut für Biometrie und klinische Epidemiologie übernimmt hierfür keine Haftung.

Datum: 10.08.2021 [redacted]

Unterschrift Beraterin, Institutsstempel